東海大学大学院平成 28 年度博士論文

Growth of Vanadium Dioxide Films on Conductive Layers by Inductively Coupled Plasma-Assisted Sputtering Method and Their Out-of-Plane Resistance Switching Characteristics

（誘導結合プラズマ支援スパッタ法による導電層上への
二酸化バナジウム薄膜の成長と面直方向抵抗スイッチング
に関する研究）

指導教員　　沖村邦雄　教授

東海大学大学院　総合理工学研究科
総合理工学専攻

MD. SURUZ MIAN

Dedication

I would like to dedicate this thesis to my beloved parents, brother and sisters for their endless love, support and encouragements. When I entered my elementary school, we were in financially difficult state, and later when my brother and sisters started their school, the situation became more difficult. But, they always encouraged us to continue our study. With their continuous support, I was able to complete my Ph. D degree.

I love you so much my dear greatest Father and Mother.

Acknowledgements

In the name of almighty Allah, the Most Beneficent and the Most Merciful.

First and foremost, I would like to express thanks to my 'Allah', who created me.

First of all, I would like to express my greatest appreciation to my supervisor Prof. Dr. Kunio Okimura for the continuous support from my bachelor, Master's Degree, and Ph. D degree. His generous support, patience, valuable guidance, motivation, and encouragement during my Ph. D study is the outcome of the thesis today. It was not possible to write this thesis without his precious comments, suggestions, throughout the theoretical and experimental works on this thesis. It is my lifelong delightful memory to work under his guidance.

I would like to express my sincere appreciations for the member of supervisory committee; Prof. Dr. Kiyoteru Kobayashi, Prof. Dr. Yoshiyuki Show, Prof. Dr. Masao Kohzaki, and Prof. Dr. Yoshihito Matsumura. Their fruitful comments and advices greatly improved quality of this thesis as well as enriched the level of my knowledge. Particularly, I am very grateful to Prof. Dr. Kiyoteru Kobayashi for his kind advices and valuable suggestions on this thesis.

My grateful thanks go to Miss. Nurul Hanis Binti Azhan, Ph. D student of our laboratory, for her experimental co-operation, valuable discussion, and fruitful comments on this work.

Warm thanks to Master's Course student, Mr. Kui Su for his cordial help. Thanks to all undergraduate students, those who were directly and partially related in this study.

I would like to express my gratitude to Prof. Dr. Masao Kohzaki and Mr. Arai Masatoshi, Department of Mechanical Engineering, Tokai University for their kind co-operation with TiN film depositions. The TiN film depositions were one of the most important materials for this thesis.

I would like to express my gratefulness to Dr. Joe Sakai, Univ. Tours GREMAN, France for his valuable discussion, and suggestive comments on this study, and also for being a co-author in journal paper.

I am very thankful to Takayama International Education Foundation for their financial support during my study, without their support, I do not think it is possible for me to continue this study.

I would like to express my loving gratitude to Tokai University Shonan Campus for giving me the opportunity to study in such a beautiful campus for about ten years from my Japanese language course, undergraduate, master's degree and Ph. D study in course of Electrical and Electronics, Department of Science and Technology, Graduate School of Science and Technology.

I am very thankful to all staffs of Future Science and Technology Joint Research Center, Tokai University for the opportunities to use all instruments such as Materials Research Diffractometer (MRD), X-ray Photo Electron Spectroscopy (XPS), and Scanning Electron Microscopy (SEM). These devices have such great contributions on my thesis and for achieving such super results.

Last but not least, my deepest gratitude goes to my beloved parents, brother, sisters and also to my friends for their endless love, support, and encouragements.

I would like to express great thanks to my cousins and their families for their endless support and encouragements.

Lastly, thank you all who were directly and indirectly related in this thesis.

For any errors and inadequacies that remain in this thesis, the responsibility is entirely my own.

Table of Contents

Dedication

Acknowledgement

Table of contents

List of Tables

List of Figures

List of Symbols

Chapter 1 Forward ……..... …1

1.1 Introduction …….....1

1.2 Vanadium Dioxide (VO_2) …….. ….2

1.2.1 Crystalline Structure of VO_2 ……...…2

1.2.2 Band Structure of VO_2 ……...….5

1.2.3 Synthesis of VO_2 ……..…..… 7

1.3 Voltage Triggered Resistance Switching (VTRS) of VO_2: *A Review* ……..…….....8

1.4 VO_2-Based Two-Terminal Planar Type Devices … ……..……..….10

1.5 Importance of Layered Type Device ……...11

1.6 Research Objective ……...…..12

1.7 Organization of Dissertation …….....……13

References ……15

Chapter 2 Growth of VO_2 Films on Ti/Si Substrates by Inductively Coupled Plasma-Assisted Sputtering Method ….....……..20

2.1 Introduction ……20

2.2 Experimental Procedure ……...……..….22

2.2.1 Conventional Sputtering (CS) ……..……..……..…....22

2.2.2 Inductively Coupled Plasma-Assisted Sputtering (ICPS) Method …….24

2.2.3 Resistance-Temperature (*R-T*) Measurement Set-up and Evolution of *R-T* Characteristics ……..……25

2.3 Results and Discussion ……...…….27

2.3.1 Fabrications of Ti Electrodes and Its Characterizations ……. … ….27

2.3.1-1 Deposition Conditions and Electrical Properties ……..……..…..….27

2.3.1-2 XRD Pattern of Ti/Si Substrates ……..……..…..…….. ...….28

2.3.2 Deposition of VO_2 Films on Ti/Si Substrates by ICPS ……..……..……..….....29

2.3.2-1 Deposition Conditions of VO_2 Films in ICPS ……..…….……..……...29
2.3.2-2 *R-T* Characteristics and XRD Pattern of VO_2 Film Deposited on Ti/Si Substrates at 400°C .....…….…….....……..…30
2.3.2-3 XRD Patterns of VO_2 Films Deposited on Ti/Si Substrates by the ICPS at Different Substrate Temperatures ….....……...…….....31
2.3.2-4 *R-T* Characteristics of VO_2 Films Deposited on Ti/Si Substrates by the ICPS at Different Substrate Temperatures ……...…….…33
2.3.2-5 Reproducibility of *R-T* Characteristics in Point Contact Measurement Method….....35
2.3.2-6 Resistivity-Temperature (ρ-*T*) Characteristics and Mechanism of Large Out-of-Plane IMT in Layered Type Device 36
2.3.2-7 Arrhenius Plots (σ-*1/T*) Characteristics of the Sample Prepared at 250ºC …….38
2.3.3 Comparison of Deposition Performance of Conventional Sputtering (CS) with ICPS .....…….…..39
2.3.3-1 Deposition Conditions of VO_2 films in CS …….....….....…… 39
2.3.3-2 XRD Patterns of VO_2 Films Deposited on Ti/Si Substrates by the CS …….....40
2.3.3-3 *R-T* Characteristics of VO_2 Films Deposited on Ti/Si Substrates by the CS ……....41
2.3.4 Characterization of ICPS and CS ……..……..... 42
2.3.4-1 Experimental Procedure ……...……..…….....42
2.3.4-2 Ion Energy Distributions (IEDs), Plasma Parameters, and Optical Emission 45
2.3.5 Characterization of the Samples Prepared by ICPS at Different Substrate Temperatures (*T*s) ……...……..……..…….49
2.3.5-1 FE-SEM Images for the Samples Prepared at *T*s from 250 to 400ºC ……..…...49
2.3.5-2 Cross-sectional SEM Images for the Samples Prepared at *T*s from 250 to 400ºC ……...……..……...…….....50
2.3.5-3 XPS Depth Profiles for the Samples Prepared at *T*s from 250 to 400ºC …….....51
2.3.5-4 Current-Voltage (*I-V*) Characteristics of the Samples Prepared at *T*s from 230 to 300ºC ….....……..53
2.3.6 Growth of VO_2 Films on Ti/Si Substrates with Different Film Thicknesses by the ICPS ……...…….....55
2.4 Conclusions ….……...……...……....….....60

References ……..……...…….…...62

Chapter 3 Growth of VO_2 Films on TiN/Ti/Si Substrates by Inductively Coupled Plasma-Assisted Sputtering Method ...…….……65

3.1 Introduction ……65
3.2 Experimental Procedure ……..……..66
3.2.1 Deposition Conditions of TiN Films ……..……66
3.2.2 Deposition Conditions of VO_2 Films …….…….…….....….....…..67
3.3 Results and Discussion
3.3.1 XRD Patterns of TiN Films Deposited on Ti/Si Substrates……..……...…….…68
3.3.2 XRD 2θ scan Patterns of VO_2 Films Deposited at Different Substrate Temperatures …...……..……...……..……...……69
3.3.3 *R-T* Characteristics of VO_2 Films Deposited at Different Substrate Temperatures ……..71
3.3.4 Surface SEM Images of VO_2 Films Deposited at Substrate Temperatures of 250 and 400ºC ……..……....75
3.3.5 Cross-sectional SEM Images of VO_2 Films Deposited at Substrate Temperatures of 250 and 400ºC …….……..……...….....76
3.3.6 XPS Depth Profiles of VO_2 Films Deposited at Substrate Temperatures of 250 and 400ºC ……...……...…….....77
3.3.7 *I-V* Characteristics of VO_2 Films Deposited at Substrate Temperatures of 250 and 400ºC …….……..……...…..…79
3.4 Conclusions ……...……..…….....81

References …….……..……..…83

Chapter 4 Self-sustaining Oscillation of VO_2-Based Layered Type Device ……..……..……..…….84

4.1 Introduction …….……..……..…....84
4.2 Experimental Procedure ..…….....…..86
4.3 Results and Discussion ……...……..87
4.3.1 XRD Pattern of VO_2 Film Deposited on TiN/Si Substrates ……..…..…..……87
4.3.2 *R-T* Characteristics of VO_2 Film Deposited on TiN/Si Substrates ……..….....88
4.3.3 XPS Depth Profiles of VO_2 Film Deposited on TiN/Si Substrates ……..……89
4.3.4 *I-V* Characteristics of VO_2 Film Deposited on TiN/Si Substrates ……..….....90
4.3.5 Oscillation Measurement of VO_2 Film Deposited on TiN/Si Substrates …….…....91
4.3.5-1 Fundamental of Oscillation Measurement Method …..…..…….....…91

4.3.5-2 Dependence of Oscillation Frequency on *V*s and R_E ……92
4.3.5-3 Analytical Study of Oscillation Phenomena ……93
4.3.5-4 Parametric Dependence of the Self-Oscillation Phenomenon in VO_2/Ti/Si Structures ……96
4.3.5-5 Multi-step Resistance Switching and the Self-Oscillation Phenomenon ……99
4.3.5-6 High-frequency Self-Oscillation in VO_2/TiN/Si Structures ……100
4.3.5-7 Mechanism of High-frequency Self-Oscillation ……101
4.4 Conclusions ……102

References ……104

Chapter 5 Summary and Future Works ……106

5.1 Summary ……106
5.2 Future Works ……111

Achievements

List of Tables

Table 1-1 Summary of the crystalline structure of VO_2. ……..……..…4

Table 2-1 Deposition conditions and electrical resistivity of deposited Ti films. …….…... 27

Table 2-2 Deposition conditions of VO_2 films in ICPS. ….……...……...……..29

Table 2-3 IMT properties of VO_2 films on Ti/Si substrates deposited at different *T*s. …….....34

Table 2-4 Deposition conditions of VO_2 films in CS. ……..……..……..……39

Table 2-5 Mean energy of IED, E_{mean}, energy at peak, E_{peak}, plasma space potential, V_s, electron temperature, T_e, and electron density, N_e. E_{mean} and E_{peak} were obtained from the measured IED's. V_s, T_e, and N_e were measured by Langmuir probe measurements. 48

Table 2-6 *I-V* properties of the samples prepared at *T*s from 230 to 300ºC. ……...……54

Table 3-1 Deposition conditions and electrical resistivity of deposited Ti and TiN films. 66

Table 3-2 Deposition conditions of VO_2 films. ……..……...…….…..…..67

Table 3-3 IMT properties of VO_2 films fabricated on TiN/Ti/Si substrates at different *T*s. ……74

List of Figures

Fig. 1-1 High temperature tetragonal rutile unit cell of VO_2 (R). 2
Fig. 1-2 Low temperature monoclinic unit cell of VO_2 (M1). 3
Fig. 1-3 Energy levels of V 3*d* orbitals in VO_2. 5
Fig. 1-4 Schematic band structure of VO_2. 6
Fig. 1-5 Schematic of VO_2-based two-terminal planar type devices. 10
Fig. 1-6 Schematic of VO_2-based layered type device. 12
Fig. 2-1 Schematic of VO_2/Ti/Si layered structure. 21
Fig. 2-2 Schematic of rf magnetron sputtering apparatus. 22
Fig. 2-3 Schematic of ICP-assisted sputtering apparatus. 24
Fig. 2-4 Schematic of *R-T* characteristics measurement method. 25
Fig. 2-5 *R-T* characteristics evolution. 26
Fig. 2-6 XRD pattern for the Ti film deposited on Si substrates. 28
Fig. 2-7 (a) Out-of-plane *R-T* characteristics and (b) XRD pattern for the sample fabricated at 400ºC. 30
Fig. 2-8 XRD 2θ scan patterns of the samples prepared at different substrate temperatures. 31
Fig. 2-9 Out-of-plane *R-T* characteristics of the samples prepared at different substrate temperatures, (a) for 300 - 400ºC and (b) for 200 - 250ºC, respectively. 33
Fig. 2-10 (a) Reproducibility of *R-T* characteristics in point contact measurements for the sample prepared at 250ºC in different places and (b) *R-T* with error bars. 35
Fig. 2-11 (a) Schematic of resistivity calculation, (b) ρ-*T* characteristics for the sample prepared at 250ºC, and (c) Relationship between R_{RT} of the VO_2/Ti/Si structure and the electrode area, *S*, of Ti electrode. 36
Fig. 2-12 Arrhenius plots of conductivity, σ, against 1/T for the sample deposited at 250ºC. 38
Fig. 2-13 XRD patterns of VO_2 films deposited at 250 and 400ºC. The results of ICP-assisted sputtering method is reused from Fig. 2-8. 40
Fig. 2-14 Resistance-temperature (*R-T*) characteristics of VO_2 films prepared by (a) CS method and (b) ICP-assisted sputtering method at substrate temperatures of 250 and 400°C. 41
Fig. 2-15 (a) Schematic experimental setup for measurements of IEDs in the ICP-assisted sputtering apparatus, (b) ion energy analyzer consisting of three mesh grids, (c) an example of collected current, I_c, against retarding potential, V_r. The first derivative of I_c with respect to V_r, - (dI_c/dV_r) represents ion energy distribution. 42

Fig. 2-16 IEDs of substrate-incident Ar^+ for both CS and ICPS. Intensities of IEDs against ion

energy were normalized such that the integral value of the area of each IED converges to unity as a probability function. ……..…45

Fig. 2-17 Characteristics of electron current, I_e, against probe voltage, V_p, for ICP-rf and target-rf power of 200 W in the case of 0.5 Pa. Space potential, V_s = 156 V was given by the intersection of two straight lines. ……..……...……...…46

Fig. 2-18 Optical emission intensities for O* (777 nm) atoms for (a) ICPS and (b) CS. ……47

Fig. 2-19 Surface SEM images for the samples prepared at (a) 250ºC, (b) 300ºC, (c) 350ºC, and (d) 400ºC, respectively. ……..……...….....…..49

Fig. 2-20 Cross-sectional SEM images for the samples prepared at (a) 250ºC, (b) 300ºC, (c) 350ºC, and (d) 400ºC, respectively. ……...……...….50

Fig. 2-21 XPS depth profiles for the samples prepared at (a) 250ºC, (b) 300ºC, (c) 350ºC, and (d) 400ºC, respectively. ……..……..……..51

Fig. 2-22 (a) *I-V* characteristics of the samples prepared from 230 to 300ºC, (b) ln (*I/V*) vs. $\sqrt{V}$ measured from (a), and (c) – (e) present the each graph for the all samples taken from (b). ……...…….….....…..53

Fig. 2-23 Cross-sectional SEM images of VO_2 films deposited for (a) 20 min, (b) 40 min, (c) 60 min, and (d) 80 min, respectively. ……..…….….....…...55

Fig. 2-24 XRD patterns of the samples prepared with different film thicknesses. …..……..56

Fig. 2-25 *R-T* characteristics of the samples prepared with different film thicknesses. ……..…57

Fig. 2-26 (a) *I-V* characteristics of the samples prepared with different film thicknesses, (b) P-F plots [ln (*I/V*) vs. √V] constructed from *I-V* curves shown in (a), and (c) values of V_{th} and I_{th} against film thicknesses ……..…58

Fig. 2-27 Switching electric field and power consumption of the samples prepared with different film thicknesses. ……..……..…..59

Fig. 3-1 Schematic of VO_2/TiN/Ti/Si layered structure devices. ……...…….65

Fig. 3-2 XRD Patterns of TiN films deposited on Ti/Si substrates. ……..…….….....….68

Fig. 3-3 XRD 2θ scan patterns of the samples prepared at different substrate temperatures. ……..…69

Fig. 3-4 Changes of peak intensity for VO_2 (011) plane observed in XRD patterns for both VO_2/Ti/Si and VO_2/TiN/Ti/Si structures. ……...…….....70

Fig. 3-5 *R-T* characteristics of VO_2 films deposited on TiN/Ti/Si substrates at different substrate temperatures. ……..…..……..…….71

Fig. 3-6 A comparison of the *R-T* characteristics for the samples prepared at *T*s = 400°C for both structures. ……..……..…..72

Fig. 3-7 Changes of R_{RT} with substrate temperatures for both structures. ……..…..….72

Fig. 3-8 Transition temperatures of VO_2 films fabricated on Ti/Si and TiN/Ti/Si substrates at different substrate temperatures. ……...…….....……73

Fig. 3-9 Surface SEM images of VO_2 films fabricated on TiN/Ti/Si substrates at low (250°C) substrate temperature (a) and high (400ºC) substrate temperature (b). ……..……75

Fig. 3-10 Cross-sectional SEM images of VO_2 films fabricated on TiN/Ti/Si substrates at low (250°C) substrate temperature (a) and high (400ºC) substrate temperature (c). (b) and (d) present for the VO_2/Ti/Si structure deposited at the same temperatures. ……76

Fig. 3-11 XPS depth profiles of VO_2 films fabricated on TiN/Ti/Si substrates at (a) 250ºC and (c) 400ºC. Images of (b) and (d) present the XPS depth profiles of VO_2/Ti/Si structures, where (b) for 250ºC and (d) for 400ºC, respectively. ……77

Fig. 3-12 *I-V* characteristics of VO_2 films fabricated on TiN/Ti/Si substrates at (a) 250ºC and (b) 400ºC. ……79

Fig. 4-1 Schematic of VO_2/TiN/Si layered structure devices. ……85

Fig. 4-2 (a) XRD 2θ scan pattern of VO_2 film deposited on TiN/Si substrates, and (b) cross-sectional SEM image and (c) surface SEM image of the produced VO_2/TiN/Si structures. ……87

Fig. 4-3 *R-T* characteristics of VO_2 film deposited on TiN/Si substrates. ……..88

Fig. 4-4 XPS depth profiles of VO_2 film deposited on TiN/Si substrates. ……89

Fig. 4-5 (a) Out-of-plane *I-V* measurement method and (b) *I-V* characteristics of VO_2 film deposited on TiN/Si substrates. ……90

Fig. 4-6 A schematic of oscillation measurement circuit. ……91

Fig. 4-7 (a) Oscillation waveforms for different *V*s, (b) dependence of f_{osc} on *V*s, and (c) dependence of f_{osc} on R_E. Minimum value of f_{osc}, observed firstly with increasing V_S, is plotted for each R_E. ……92

Fig. 4-8 (a) Equivalent circuit for the self-oscillation. (b) Comparison between an analytic and experimental waveforms. (c) Dependence of oscillation frequency, f_{osc}, on series resistance, R_E. Dotted line shows analysis based on equation (10). Minimum value of f_{osc}, observed firstly with increasing V_S, is plotted for each R_E. ……93

Fig. 4-9 (a) Oscillation waveforms and (b) f_{osc} for different film thicknesses. (c) Oscillation waveforms and (d) f_{osc} for different probe diameters. ……..96

Fig. 4-10 (a) *I-V* characteristics with different hysteresis width and (b) f_{osc} for different hysteresis width. ……..97

Fig. 4-11 (a) *I-V* characteristics with multi-step switching and (b) dependence of f_{osc} on *V*s for this *I-V* characteristics. ……99

Fig. 4-12 (a) *I-V* characteristics with multi-step switching for high frequency oscillation mode,

(b) oscillation waveforms for different Vs, and (c) dependence of f_{osc} on Vs. Series resistance, R_E, was kept constant at 30 kΩ. ……..100

Fig. 4-13 Illustrations for voltage triggered switching with NDR ($dV_D/dI_D < 0$) region after the onset of IMT for cases without hysteretic behavior between paths of IMT and MIT (i), with hysteretic behavior (ii), and multiple NDR regions with smaller hysteresis (iii). ……..……..……101

List of Symbols

IGZO	: Indium gallium zinc oxide	
ZnO	: Zinc oxide	
NiO	: Nickel oxide	
TMOs	: Transition metal oxides	
TiO_2	: Titanium dioxide	
CrO_2	: Chromium dioxide	
MnO_2	: Manganese dioxide	
ZrO_2	: Zirconium dioxide	
VO_2	: Vanadium dioxide	
IMT	: Insulator-metal transition	
Ti	: Titanium	
V	: Vanadium	
V_2O_3	: Vanadium sesquioxide *or* trioxide	
Ti_2O_3	: Titanium trioxide	
$SmNiO_3$	: Samarium nickelate	
Ti_3O_5	: Titanium pentoxide	
$LaCoO_3$	: Lanthanum cobalt oxide	
SPT	: Structural phase transition	
M1	: Monoclinic	
R	: Rutile	
T_{IMT}	: Transition temperature	
E_F	: Fermi level	
UPS	: Ultraviolet photoelectron spectroscopy	
XAS	: X-ray absorption spectroscopy	
ICPS	: Inductively coupled plasma-assisted sputtering	
PLD	: Pulsed laser deposition	
CVD	: Chemical vapor deposition	
HiPIMS	: High power impulse magnetron sputtering	
MIM	: Metal-insulator metal	
VTRS	: Voltage triggered resistance switching	
I-V	: Current - voltage	
NDR	: Negative differential resistance	
L	: Electrode distance	[μm]
V_{th}	: Switching voltage	[V]

I_{th}	: Switching current	[μA]
O*	: Oxygen radicals	
BE	: Bottom electrode	
CS	: Conventional sputtering	
ICPS	: Inductively coupled plasma sputtering	
XRD	: X-ray diffractometer	
R-T	: Resistance- temperature	
SEM	: Scanning electron microscopy	
XPS	: X-ray photoelectron spectroscopy	
TiN	: Titanium nitride	
rf	: Radio frequency	
TMP	: Turbo-molecular pump	
sccm	: Standard cubic centimeter	
ρ	: Resistivity	[Ω cm]
R_{RT}	: Resistance at room temperature	[Ω]
R_{100}	: Resistance at 100ºC	[Ω]
T_{IMT}	: Transition temperature	[ºC]
T_{IMT-H}	: Transition temperature for heating	[ºC]
T_{IMT-C}	: Transition temperature for cooling	[ºC]
ΔR	: Transition width	
ΔH	: Hysteresis width	[ºC]
*T*s	: Substrate temperature	[ºC]
d	: Area of probe contact	[μm]
s	: Cross-sectional of contact probe	[m]
l	: VO_2 film thickness	[nm]
S	: Electrode area	[mm^2]
σ	: Conductivity	[$\Omega^{-1}cm^{-1}$]
k	: Boltzmann's constant	[JK^{-1}]
T	: Temperature	[K^{-1}]
ΔEa	: Activation energy	[eV]
IP	: Insulator phase	
MP	: Metal phase	
IEDs	: Ion energy distributions	
V_s	: Plasma space potential	[V]
V_r	: Retarding potential	[V]
I_c	: Collected current	[μA]

W	: Tungsten	
V_p	: Probe voltage	[V]
E_{mean}	: Mean energy of IED	[eV]
E_{peak}	: Energy at peak	[eV]
T_c	: Electron temperature	[eV]
N_e	: Electron density	[cm^{-3}]
E_{th}	: Switching electric field	[V/m]
P	: Power consumption	[W]
P-F	: Poole-Frenkel	
S	: Electrode area	[mm^2]
τ	: Time constant	[s]
f_{osc}	: Oscillation frequency	[Hz]
WC	: Tungsten carbide	
Vs	: Source voltage	[V]
R_E	: Series resistance	[kΩ]
V_D	: Voltage of VO_2	[V]
MIT	: Metal-insulator transition	
τ_1	: Recovery time for MIT	[s]
τ_2	: Time needed for IMT	[s]
R_D	: Resistance of VO_2 device	[kΩ]
C_D	: Capacitance of VO_2 device	[F]
i_D	: The current flowing through the device	[A]
q_D	: Electric charge of device	[C]
i_E	: The current flowing through the R_E	[A]
i_C	: The current flowing through the C_D	[A]
i_R	: The current flowing through the R_D	[A]
V_E	: Voltage of R_E	[V]
V_D (t)	: Time-dependent voltage across the VO_2 device	[V]

CHAPTER 1

Forward

Chapter 1 Forward

1.1 Introduction

For years, oxide materials such as indium gallium zinc oxide (IGZO)[1], zinc oxide (ZnO)[2], and nickel oxide (NiO)[3] have been actively studied for applications in several fields such as smart glass, liquid crystal display drivers, and nickel-ion batteries.[1–3] Recently, transition metal oxides (TMOs) have become central subject in both scientific and technological works for the next generation device materials. In last decade, TMOs such as titanium dioxide (TiO_2)[4], chromium dioxide (CrO_2)[5], manganese dioxide (MnO_2)[6], zirconium dioxide (ZrO_2)[7] and vanadium dioxide (VO_2)[8–23] has been widely being investigated for various industrial applications, including paints, varnish, magneto-electronics, dry-cell battery, ceramics industry, as well as electronic devices.[1–7,9,13,16,20–24]

Among TMOs, VO_2 is the most promising material and has been continuously gathering attentions considering its interesting characteristics of insulator-metal transition (IMT). The IMT in VO_2 was firstly reported by Morin in 1958.[25] He reported that the metallic behavior of the lower oxide of titanium (Ti) and vanadium (V). He pointed out that polycrystalline titanium and vanadium trioxides (Ti_2O_3 and V_2O_3) exhibit IMT at Neel temperature. Then, a year later in 1959, Morin reported that VO_2 exhibits a sharp IMT at low temperature of 68ºC, named as a Morin transition.[8]

VO_2 undergoes a sharp IMT and accompanied by a structural phase transition (SPT) from a low temperature monoclinic ($P2_1/c$) phase to a high temperature tetragonal ($P4_2/mnm$) phase at a relatively low temperature of 68ºC (341K). An abrupt change in resistivity for more than four orders of magnitude was occurred in this transition temperature.[8,12,13,15–17,20,21,24,26–33] Other oxides such as samarium nickelate ($SmNiO_3$), titanium pentoxide (Ti_3O_5) and lanthanum cobalt oxide ($LaCoO_3$) also exhibit IMT at higher temperatures, such as 130ºC for $SmNiO_3$, 127-327ºC for Ti_3O_5, and 227ºC for $LaCoO_3$.[34] Thus, it is desirable to use VO_2 with low IMT temperature for the device applications. As for the IMT of VO_2 at temperature of 68ºC, it could be easily triggered by external parameters such as electrical field,[13,16,17,19,20,31,35] optical excitation,[14,36] pressure,[19] stress,[37] Joule heating,[38] and as well as temperature.[8] VO_2 is continuously gathering great interest in several fields application such as high speed electrical switching devices,[13,19,20,22,31,39] optical switching devices,[40] infrared detectors,[41] smart windows,[42] memory,[43] sensors, non-volatile memories,[44] thermochromic devices,[45] memristors,[46] hybrid metamaterials,[47] and data storages.[48]

1.2 Vanadium Dioxide (VO_2)

1.2.1 Crystalline Structure of VO_2

Structural phase transitions refer the changes of the crystallography in materials. According to the SPTs, the macroscopic properties of a material are changed. So, the study of these change is important for various applications. As shortly briefed in last section, VO_2 shows a structural phase transition (SPT) from a low-temperature monoclinic phase to a high-temperature tetragonal rutile phase at relatively low temperature of 68ºC.

Rutile structure

Rutile structure of VO_2 is the most stable phase at higher temperature side, based on a simple tetragonal lattice with space group $P4_2/mnm$ $(D_{4h}^{14}, No.136)$.[49] The Wyckoff positions of vanadium atoms are (2a): (0, 0, 0), $(\frac{1}{2},\frac{1}{2},\frac{1}{2})$ and oxygen atoms are (4f): ± (u, u, 0) and ± $(\frac{1}{2}+u,\frac{1}{2}-u,\frac{1}{2})$; where the values are (0.301, 0.301, 0). Figure 1-1 shows the high temperature tetragonal rutile unit cell of VO_2.

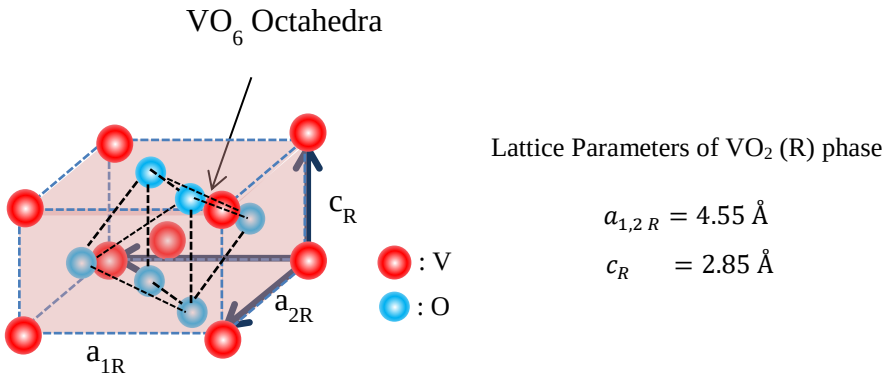

Fig. 1-1 High temperature tetragonal rutile unit cell of VO_2 (R).

Rutile structure is visualized as a body-centered tetragonal lattice, which composed of two equivalent vanadium (V) atoms at P (center) and Q (corner) per cell and each V atoms are surrounded by an oxygen octahedron, where two of the V-O bonds distance at 1.933 Å and four others are at 1.922 Å. Neighboring octahedra share edges, resulting interlinked octahedral chains via the corner of metal V atoms and build chain along the *c*-axis. The lattice constant of VO_2 rutile was firstly reported by Westman in 1961.[50] Then, in 1972, McWhan *et al.* reported the lattice constant for VO_2 rutile phase, including the internal oxygen parameter, which is close to the values are given by Marezio for $V_{0.976}\,Cr_{0.024}O_2$ $(u = 0.3004)$, reported in 1972.[51,52] McWhan *et al.* reported the values for the lattice constant and the internal oxygen parameter for VO_2 rutile phase as $a_R = 4.556$ Å, $c_R = 2.851$ Å $and\ u = 0.300$. These values have been widely used in calculation.[51]

The Monoclinic (M1) structure

The low temperature monoclinic (Hereafter referred as M1) structure of VO_2 belongs to a simple monoclinic lattice with space group of $P2_1/c$ (C_{2h}^5, No. 14).[49] Figure 1-2 represents the low temperature monoclinic unit cell of VO_2. In the M1 structure, octahedra is aligned in two perpendicular directions, although the octahedra are not so long. One short distance in V–O (0.176 nm) is corresponding to a double link. The V atoms have shifted from the center of the octahedra to form chains, which is not parallel to the c_R-axis. There is now two different distances between V atoms with 2.615Å and 3.162 Å instead of 2.851 Å for the rutile structure, leading to a doubling of the cell along the c_R axis of the rutile structure. The Wyckoff position of V and two different O is 4e: x, y, z; $\bar{x}, \bar{y}, \bar{z}$; $\bar{x}, \frac{1}{2}+y, \frac{1}{2}-z$; $x, \frac{1}{2}-y, \frac{1}{2}+z$ with four sets of two-fold point positions corresponding to the symmetry centers of the cell. The lattice constants and angle between *b*- and *c*- axis were firstly reported by Andersson in 1956.[53,54] The reported values are $a_{M1} = 5.743$ Å, $b_{M1} = 4.517$ Å, $c_{M1} = 5.375$ Å, and $\beta = 122.61°$. Then, in 1970, Longo and Kierkegaard reported different lattice constant and angel and the values are $a_{M1} = 5.751$ Å, $b_{M1} = 4.537$ Å, $c_{M1} = 5.382$ Å, and $\beta = 122.646°$, respectively. These lattice constant described are the commonly used values considering the VO_2 crystalline structure. [29,55] The crystalline structure of VO_2 are listed in Table 1-1.

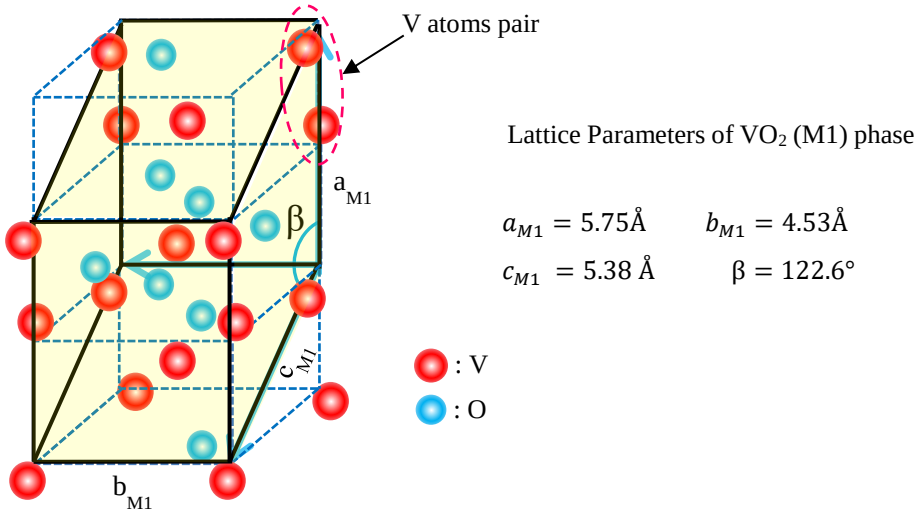

Fig. 1-2 Low temperature monoclinic unit cell of VO_2 (M1).

Table 1-1 Summary of the crystalline structure of VO_2.

Structure	**Monoclinic (M1)** **(Low-temperature phase)**	**Rutile (R) (Tetragonal)** **(High- temperature phase)**
Wyckoff Position	V and O (4e): $\pm(\mathrm{x},\mathrm{y},\mathrm{z}), \pm(\mathrm{x},\frac{1}{2}-y,\frac{1}{2}+z)$	V (2a): (0,0,0), $(\frac{1}{2},\frac{1}{2},\frac{1}{2})$ O (4f): $\pm(\mathrm{u},\mathrm{u},0), \pm(\frac{1}{2}+u,\frac{1}{2}-u,\frac{1}{2})$
Space Group	$C_{2h}^{5}(No.14)-P2_1/c$	$D_{4h}^{14}(No.136)-P4_2/mnm$
Lattice Parameter	$a_{M1}=5.753$ Å	$a_{1,2\,R}=4.555$ Å
	$b_{M1}=4.526$ Å	$c_R=2.853$ Å
	$c_{M1}=5.383$ Å	-
	$\beta=122.6°$	-
Unit Cell Volume	118.08 Å^3	59.20 Å^3
Thermal Expansion Coefficient	$\alpha_{\parallel}=4.9\times10^{-6}$ ($°C^{-1}$) $\alpha_{\perp}=26\times10^{-6}$ ($°C^{-1}$)	$\alpha_{\parallel}=26\times10^{-6}$ ($°C^{-1}$) $\alpha_{\perp}=4.9\times10^{-6}$ ($°C^{-1}$)

1.2.2 Band Structure of VO_2

As known, VO_2 demonstrates a sharp IMT at a relatively low-temperature of 68ºC accompanying by a structural change from low-temperature semiconducting M1 phase to high-temperature metallic R phase. However, mechanism of the IMT in VO_2 is not clear yet. Earlier, Goodenough explained the IMT of VO_2 based on simple band structure.[10] Goodenough focused on $3d^1$ orbitals because *d*-orbitals play an important role in IMT transition. The 3*d* electronic levels of the V ion are split into the lower energy states of triply generated t_{2g} (x^2-y^2, *yz and zx*) and doubly high energy states generated e_g (or σ^*or e_g^σ; where σ represents the symmetry of the V–O bonds and labeled as $3z^2$-r^2 and *xy* . The t_{2g} state further splits into $d_\parallel$ (x^2-y^2) and π^* (*yz, zx*), which can be understood from the point group theory. The $d_\parallel$band is weakly hybridized by O 2*p* band, while π^* band is hybridized with O *2p* π band, resulting in a higher energy than $d_\parallel$band and being push upward. Cosequently, $d_\parallel$ band has a lowest energy in the V 3*d* band. On the other hand, the doubly generated e_g levels are hybridized by O *2p* σ orbitals with a rather large bandwith. The energy levels of V 3*d* orbitals in VO_2 are given in Fig. 1-3.

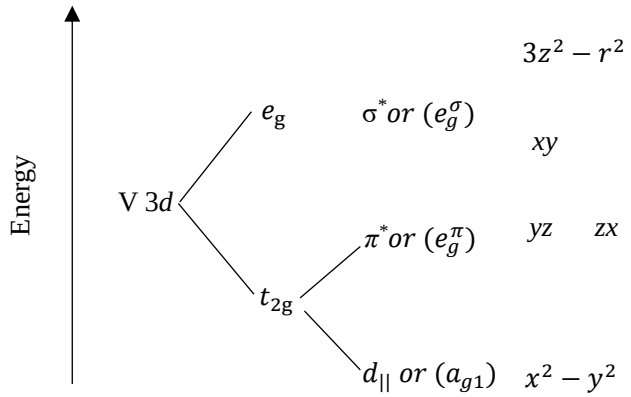

Fig. 1-3 Energy levels of V 3*d* orbitals in VO_2.

The schematic band structure of VO_2 is illustrated in Fig. 1-4. Across the IMT, two significant changes in the band structure were observed in the insulating state (Fig. 1-4); a raising of the π^* band above the Fermi level (E_F), and separation of the $d_\parallel$ orbitals to $d_\parallel$-bonding and $d_\parallel^*$-anti-bonding. As described by Goodenough, the raising of π^* above the E_F level might be resposible for destabilizing π^* orbitals or stabilizing the bottom part of $d_\parallel$ or both.[10] Crystallographic deformation results in the destabilization of the π^* orbitals. Stabilization of $d_\parallel$ would be induced by the distortion of c_R/a_R ratio and bottom half of the $d_\parallel$ bands would be stabilized by the c_R-axis doubling, since the doubiling of c_R-axis induce a split in $d_\parallel$orbital as also reported by Goodenough in 1960.[56] As results, in the insulating state, V atoms along the c_R axis displaced and form a V–V pair into a bonding and anti bonding combination of $d_\parallel$ orbitals. This displacement of V atoms from the center of the octahedral

symmetry, causes the formation of shorter V–O pairs. According to the change in the V–O hybridization, the energy of the more hibridized π^*splits and moves upward. Finally, π^* band and anti-bonding $d_{\parallel}$ ($d_{\parallel}^*$) become empty and bonding $d_{\parallel}$ band become filled. The band gap with the value of 0.65 eV has been reported by Shin *et al.* was measured by ultraviolet photoelectron spectroscopy (UPS).[57] However, the mechanism of IMT is still on debate considering two view points; 1) Peierls mechanism that suggests the dimerization of the V atoms along the c_R-axis, resulting in the opening of the gap in the insulating state[10,29,58,59], and 2) Mott mechanism, in which the gap opened due to the Coulomb repulsion between the localized 3*d* orbitals of V.[60–66]

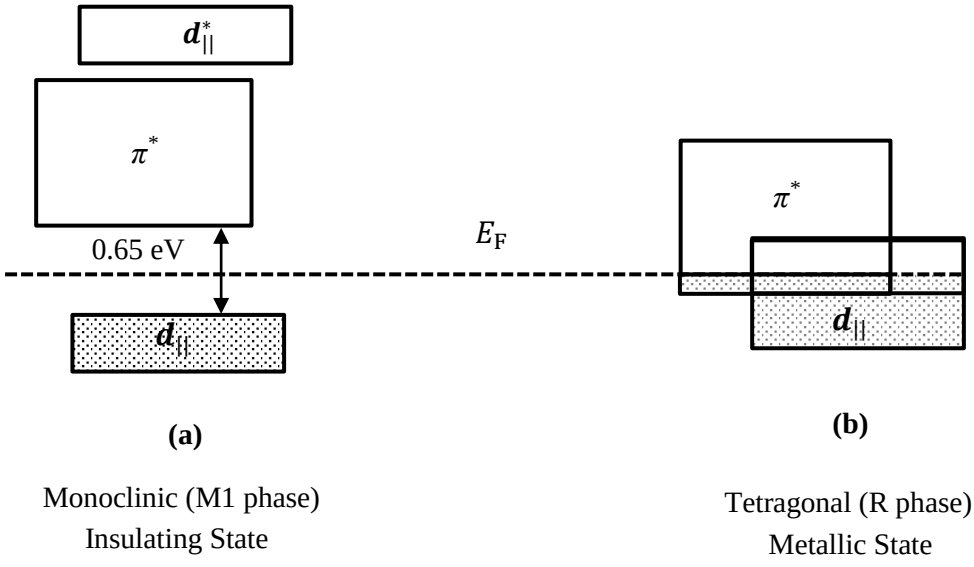

Fig. 1-4 Schematic band structure of VO_2.

1.2.3 Synthesis of VO_2

The stabilization of pure VO_2 films is remarkably sensitive to the deposition conditions. Basically, when vanadium is synthesized in the small amount of O_2, vanadium forms a lower oxidation phases, including VO, V_2O_3, V_3O_5, V_4O_7, V_5O_9, and V_6O_{11} known as Magneli phase (V_nO_{2n-1}).[67–69] On the other hand, Wadsely phase (V_nO_{2n+1}), including V_2O_5, V_3O_7, V_4O_9, V_5O_{11} and V_6O_{13} will be preferably grow when the vanadium is synthesized in rather large amount of O_2 environment.[67–70] At room temperature, with slight changes in the stoichiometry, VO_2 also understood to grown in some different phases such as – VO_2 (M1), [8,9,12,13,15,16,21,27,28,31] VO_2 (M2), [52,71–74] VO_2 (A)[75,76], and VO_2 (B)[77,78]. Considering those background, it is very difficult to produce a pure stoichiometric VO_2 films. VO_2 has been synthesized in different forms, such as bulk single crystal,[79] polycrystalline thin films,[80,81] and epitaxial thin films.[82,83] VO_2 was also reported to grow in form of nanostructure, including nanowires,[66,84,85] nanobeams, [86,87] nanoparticles,[86,88] and nanobelts.[89]

The main content of the stoichiometric VO_2 films synthesis mostly depends on the deposition temperature, background pressure, deposition pressure, and deposition technique. Numbers of deposition techniques have been investigated for growing the VO_2 film, including sputtering,[24,90] inductively coupled plasma-assisted sputtering (ICPS),[91,92] pulsed laser deposition (PLD),[15,93] chemical vapor deposition (CVD),[94] sol-gel technique,[95] atomic layer deposition,[96,97] oxide molecular beam epitaxy,[98] laser ablation,[99] hydro-thermal process[100], high power impulse magnetron sputtering (HiPIMS),[101] and substrate biasing method.[102]

Another important factor in VO_2 synthesis is substrate materials. Substrate materials play a vital role in controlling IMT and transition temperature, T_{IMT}. An enormous number of substrates was being investigated with the aim of achieving a good crystalline VO_2 films such as the different cut of Al_2O_3,[20,103,104] Si,[83,91,105] SiO_2,[106] TiO_2,[15,107] TiN,[22] Ge,[26] glass,[96,108] MgO,[109] NiO,[110] ZnO,[111] and ITO[92]. Other than that, the substrate temperature is another important content to achieve good crystalline property. It was reported that VO_2 exhibits an excellent crystallinity as the deposition is performed above 400°C.[93,94] However, such high-temperature deposition technique is not applicable for the layered type devices as metal layer diffusion could occur at the interfaces of the devices.

1.3 Voltage Triggered Resistance Switching (VTRS) of VO_2: *A Review*

Oxide materials that exhibit a resistive switching phenomenon have been studied intensively. Hysteretic current–voltage (*I–V*) characteristics in metal-insulator-metal (MIM) structures of $Al/Al_2O_3/Al$ was firstly reported by Hickmott in 1962.[112] These results suggested that resistive switching occurs as a result of voltage applied. Later, in the 1960s to 1980s, resistive switching has been reported in variety binary metal oxides such as SiO and NiO.[113–115] As for the driving mechanism of resistive switching, two models were proposed; a charge trap model and a conductive filament model. Then, several groups observed a voltage triggered induced resistance switching (VTRS) in $Pr_{1-x}Ca_xMnO_3$ (PCMO) with a certain Ca content x ($0.3 \leq x \leq 0.75$).[116–118]

VO_2 exhibits a voltage triggered resistance switching (VTRS) in room temperature as was firstly discovered in the 1960s.[119,120] It was reported that during the transition in the current-voltage (*I-V*) characteristics of a VO_2 bulk sample, it showed gradual changes of the resistance.[121,122]While extremely steep and discontinuous jump in resistance at the transition was reported in the case of VO_2 thin film.[120,123–125] It should be noted that these I-V characteristics are symmetric, and this phenomenon is different from view point for the resistance random access memory. Then, Berglund and Duchence *et al*. reported on the current switching properties in VO_2-based two-terminal planar type devices, in which due to the filamentary conduction path in the VO_2 layer.[123,125] Since then, VTRS in VO_2 has been frequently reported.[13,16,17,19,20,126] In VTRS, it has been reported that current-induced Joule heating could be responsible for the switching, owing to the occurrence of structural phase transition (SPT) in VO_2.[127] Lee *et al*. suggested that the current flows into a narrow filament in VO_2 film, generating the Joule heat, and inducing the IMT.[128] Then, in 2000, Stefanovich *et al.* reported VTRS in VO_2-based two-terminal planar type devices.[13] After a report by Stefanovich *et al.*, VO_2-based two-terminal planar type devices has been actively studied. Using some microfabrication techniques such as photolithography, reactive ion etching, and lift-off method, facing electrodes with 3–50 μm gap length on VO_2 film also reported to exhibit the VTRS phenomena.[16,17,19,20,129] Sakai and Kurisu reported the effect of hydrostatic pressure on VTRS of VO_2- based two-terminal planar type devices.[19] Okimura *et al*. reported that the VTRS was triggered at voltage, current of 2 V, 600 μA for a planar device with both electrode gap length and width of 5 and 1500 μm.[20,129] They also discovered a multistep negative differential resistance (NDR) region in the switching properties. They reported a switching speed of about 200 ns. However, such a planar device has a restriction in switching threshold voltage and current, which results in a high power consumption. According to the planar type configuration, a shorter electrodes distance (L) should bring a smaller switching voltage (V_{th}). To investigate the intrinsic properties of VTRS, it is highly desirable to achieve a layered structure of VO_2 film on a conductive layer, so-called out-of-plane device or layered type device or sandwich type device. In the out-of-plane configuration, in which VO_2 film is fabricated on a bottom electrode (BE), the switching voltage is expected to be significantly reduced because the responsible L is equal to the

film thickness of the VO_2 layer. Also, this layered type configuration will be essential for the integrated device application. Ramanathan *et al.* fabricated VO_2 film on a heavily doped Si wafer with a resistivity of (2–5) $\times 10^{-4}$ Ω cm, and showed VTRS in the out-of-plane metal-oxide-semiconductor geometry.[26,130,131] They proposed that the VTRS is resulted from a field effect or carrier injection, rather than current-induced Joule heating effect.[130] Son *et al.* reported the performance of a selector using VO_2 film on a Pt/TiN/SiO_2/Si substrates.[90] They obtained VO_2 film by thermal annealing for metal vanadium film at 500°C. However, details of the IMT was not reported. Sakai *et al*. reported the growth of VO_2 films on Pt (111)/TiO_2/SiO_2/Si (001) substrates by pulsed laser deposition method at a substrate temperature of 500°C.[132] To date, layered growth of VO_2 film on a metal layer, which exhibits IMT with several orders of change in resistance has not been reported.

1.4 VO_2-Based Two-Terminal Planar Type Devices

The voltage triggered resistance switching (VTRS) phenomenon was firstly reported by Berglund in 1969.[123] Studies on the nonlinear resistive switching in VO_2 have been reported in the 1970s.[125] Later, various types of switching devices were being investigated on the basis of nonlinear *I-V* characteristics. However, this nonlinear *I-V* characteristics might not be involved in the electric field induced IMT. The firstly reported IMT switching was introduced by the Joule heating effect.[8] Then, in 2000, Stefanovich *et al.* reported on the electric field induced resistance switching in VO_2.[13] After this report, wide scale studies have been performed on the VTRS of VO_2 with the aim of VO_2 applications sufficiently in electrical switch, resistive memories etc.[16,19,20,126,129,133–135] This switching phenomenon is accompanied by a structural change from the insulator monoclinic phase to metallic rutile phase; same as being reported in the thermally induced resistance switching. As shortly described in forward, VO_2 is actively being investigated for the purpose of application in several fields. Among them, research on VO_2-based two-terminal planar type switching devices is the most highly progressed.[13,16,19,20,129,133,135,136] Planar type device referred to VO_2 films grown on Si or *c*-Al_2O_3 substrates with facing electrodes with gap of 3–50 μm length. The electrodes are deposited onto the VO_2 films by using microfabrication techniques such as photolithography, reactive ion etching, and lift-off method. In this type of devices, all measurements were performed in an in-plane direction. The reported switching voltage (V_{th}) for this type devices as larger than several Volts. The lowest V_{th} and switching current, I_{th} of about 2 V, 6 mA were reported by Okimura *et al.* with electrode gap of 5 μm. Figure 1-5 shows a schematic of VO_2-based two-terminal planar type devices.

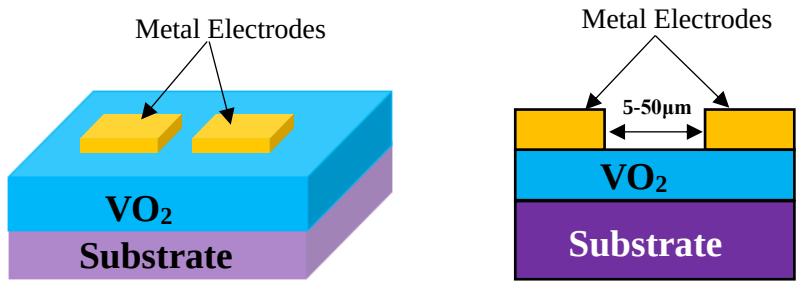

(a) Three dimensional view **(b) Cross-sectional view**

Fig. 1-5 Schematic of VO_2-based two-terminal planar type devices.

1.5 Importance of Layered Type Device

In the previous section, VO_2-based two-terminal planar type devices were explained. However, there are some disadvantages of the planar type devices. Firstly, the mechanism of the current flow is not clear. It is either the current flow through the VO_2 films or between the two electrodes. Secondly, higher switching voltage (V_{th}) and current (I_{th}) in the threshold switching, which is responsible for high power consumption. In the planar type devices, the V_{th} depends on the distance between the two electrodes gap. Consequently, such VO_2-based two-terminal planar type devices has a limit for restriction of the threshold voltage and current for switching.[13,16,19,20,128,129,137] So, it is highly required to achieve a layered type device (out-of-plane or sandwich type device), in which VO_2 films is deposited onto a conductive layer with the aim of application as a low consumption power selector switch. The switching voltage and current are expected to be significantly reduced in an out-of-plane configuration, since the film thickness of the VO_2 layer corresponds to the electrode distance in the planar-type devices. Additionally, this type of structure is highly necessary for the integrated device applications. Lee *et al.* proposed Pt/VO_2/Pt layered structure as a selector switch for the low-voltage and high-speed non–volatile memory. [44]Then, Ramanathan group fabricated VO_2 films on a heavily doped Si wafer with a resistivity of (2–5) $\times 10^{-4}$ Ωcm, also with the aim of achieving the out-of-plane device structure for the reduce the switching voltage.[26,130,131,138,139] Son *et al.* reported the growth of VO_2 film by thermal annealing for metal vanadium film on a Pt/TiN/SiO_2/Si substrates at 500°C.[90] However, IMT in out-of-plane direction for VO_2 itself was not reported. Also, with the purpose of realizing a high-speed VTRS in the out-of-plane configuration, the deposition of VO_2 films on Ti metallic plate[140] and Nb-doped $SrTiO_3$ were introduced as conductive substrates.[141] Recently, Sakai *et al.* reported the growth of VO_2 films on Pt (111)/TiO_2/SiO_2/Si (001) substrates by the pulsed laser deposition method at a substrate temperature of 500°C with the aim of realized a low voltage and power consumption switching devices.[132] Among all report for the VO_2-based layered type device, only a few studies was succeeded to reduce switching voltage around 1 V, however, they could not succeed to reduce switching current in several tens μA orders, which is most essential for realizing a low power consumption switching devices. Additionally, the crystal morphology, the interface states between the VO_2 film and the bottom electrode, and the out-of-plane IMT with more than 2 orders of magnitude change in resistance has not yet been reported.

1.6 Research Objective

This dissertation focuses on the crystal growth of VO_2 films on conductive layers with the aim of achieving a layered structure to realize a low voltage and low power consumption switching devices. Figure 1-6 presents the schematic of VO_2-based layered type device as proposed in this study. The out-of-plane IMT characteristics will be investigated together with crystalline structure, crystalline morphology and the interface between the VO_2 film and the metal layer. In VTRS, reductions of switching voltage and current, hence power consumption at the switching, are mandatory issues to be addressed. Switching voltage less than 1 V is a targeted value in the present proposed layered type device. The achieved low voltage and current in the proposed layered type device are advantageous for the application to low power consumption switching elements. In order to apply VO_2 as a selector switch for next-generation random resistive memory, such requirement is a central subject to be achieved based on the reduced operation voltage and current in the latest electronics devices. To achieve above objective, the deposition of VO_2 films on conductive layers were performed by using inductively coupled plasma-assisted sputtering (ICPS) method.

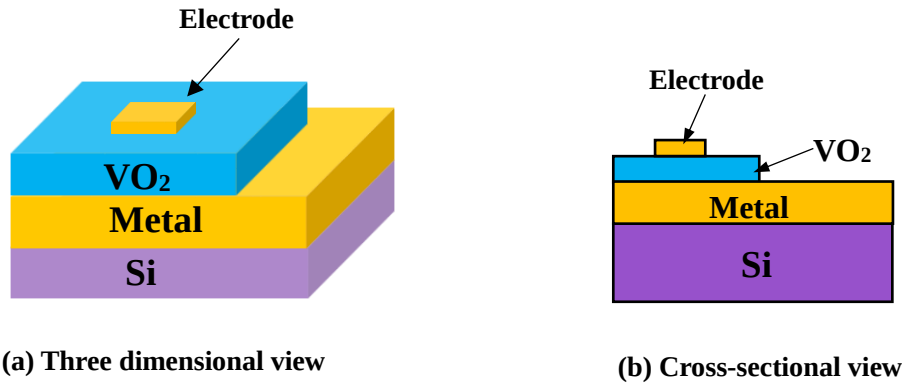

(a) Three dimensional view **(b) Cross-sectional view**

.

Fig. 1-6 Schematic of VO_2-based layered type device.

1.7 Organization of Dissertation

This dissertation is organized by 5 chapter. A short brief of this thesis is given in below.

Chapter 1

In this chapter, the background of this study was firstly introduced. A brief description on VO_2 was given, which is consisting of crystalline structure, energy band structure, and the synthesis of VO_2. A review of voltage triggered resistance switching (VTRS) was given. VO_2-based two-terminal planar type devices, together with the problem statement was described. The importance of layered type devices with the motivation of this work was also provided in this chapter.

Chapter 2

In this chapter, firstly given an explanation on experimental procedure. Then, details of the deposition processes of VO_2/Ti/Si layered structure were discussed. Crystal growth of VO_2 films was observed at a low substrate temperature of 250ºC in ICPS which revealed more than 2 orders of magnitude change in resistance in the out-of-plane direction, while the growth of VO_2 films was not observed at the same temperature in CS. Plasma diagnosis of ICPS and CS, including ion energy distributions, plasma space potential, and optical emission intensity of oxygen radicals (O*) were presented in this chapter with the aim of clarification of the low-temperature crystallization of VO_2. High substrate incident ion energy, space potential and the optical emission intensity of O* was achieved in ICPS, which assisted low-temperature crystal growth in ICPS. Morphology of VO_2 films was examined by surface SEM. The interface between the VO_2 film and the Ti layer was investigated by X-ray photoelectron spectroscopy (XPS). Voltage triggered resistance switching (VTRS) was performed by the Current –voltage (*I-V*) characteristics measurement. Low switching voltage, current and power consumption was achieved in proposed layered device structure.

Chapter 3

In this chapter, DC-magnetron sputtered titanium nitride (TiN) was introduced as a bottom electrode which also can act as a diffusion barrier layer between the VO_2 film and Ti layers. Deposition processes of TiN and VO_2 films were given. Crystallinity, layered structure, interfaces between the VO_2 film and the TiN layer were investigated by XRD, *R-T* characteristics, cross-sectional SEM, and XPS, respectively, for all samples were prepared. A superior crystal growth was observed at a low temperature of 250ºC and even at a higher temperature of 400ºC in the VO_2/TiN/Ti/Si structure, in contrast with the film on Ti/Si. Sharp out-of-plane IMT with more than 2.3 orders of magnitude change in resistance and an abrupt interface between the VO_2 film and the TiN layer was obtained at 400ºC, demonstrating the advantage of the use of TiN layer. *I-V* characteristics with low power consumption of several tens μW was achieved in the present device, promoting the application of this device as a

low power consumption switching elements.

Chapter 4

In this chapter, the oscillation phenomenon of VO_2-based layered type device was explored with the aim of investigation the switching speed and stability. A simple series circuit was used in the experimental processes. Self-oscillation with frequencies of MHz order was realized in the present device. An equivalent circuit was introduced for analytical study and comparison with experimental results. Then, the dependence of oscillation frequency on geometric parameters, including the film thickness and contact probe diameter was examined together with the dependence on circuit parameters of source voltage and series resistance. A model for high-frequency oscillation mechanism was constructed. The achieved results with MHz band oscillation in the proposed layered structure device has a great potential for industrial application such as radio frequency generator and micro-inverter. The threshold switching speed of about several tens ns was obtained in present devices, which is significantly lower than the planar type devices.

Chapter 5

In this chapter, the conclusions of this work were presented. The recommendation of future works was also delivered in this chapter.

References

[1] K. Toshio and H. Hosono, NPG Asia Mater. **2**, 15 (2010).

[2] Ü. Özgür, Ya I. Alivov, C. Liu, A. Teke, M. A. Reshchikov, S. Doğan, V. Avrutin, S.-J. Cho, and H. Morkọ, J. Appl. Phys. **98**, 1 (2005).

[3] I. Hotový, J. Huran, L. Spiess, R. Čapkovič, and Š. Haščík, Vacuum **58**, 300 (2000).

[4] X. Chen and S. S. Mao, Chem. Rev. **107**, 2891 (2007).

[5] X. Zhang, Y. Chen, L. Lü, and Z. Li, J. Phys. Condens. Matter **18**, L559 (2006).

[6] J. Fei, Y. Cui, X. Yan, W. Qi, Y. Yang, K. Wang, Q. He, and J. Li, Adv. Mater. **20**, 452 (2008).

[7] W.-J. Qi, R. Nieh, B.-H. Lee, L. Kang, Y. Jeon, and J. C. Lee, Appl. Phys. Lett. **77**, 3269 (2000).

[8] F. J. Morin, Phys. Rev. Lett. **3**, 34 (1959).

[9] C. N. Berglund and H. J. Guggenheim, Phys. Rev. **185**, 1022 (1969).

[10] J. B. Goodenough, J. Solid State Chem. **3**, 490 (1971).

[11] A. Zylbersztejn, Phys. Rev. B **11**, 4383 (1975).

[12] J. P. Pouget and H. Launois, J. Phys. **37**, 49 (1976).

[13] G. Stefanovich, A. Pergament, and D. Stefanovich, J. Phys. Condens. Matter **12**, 8837 (2000).

[14] A. Cavalleri, C. Tóth, C. W. Siders, J. A. Squier, F. Ráksi, P. Forget, and J. C. Kieffer, Phys. Rev. Lett. **87**, 237401 (2001).

[15] Y. Muraoka and Z. Hiroi, Appl. Phys. Lett. **80**, 583 (2002).

[16] H.-T. Kim, B.-G. Chae, D.-H. Youn, S.-L. Maeng, G. Kim, K.-Y. Kang, and Y.-S. Lim, New J. Phys. **6**, 52 (2004).

[17] H.-T. Kim, B.-G. Chae, D.-H. Youn, G. Kim, K.-Y. Kang, S.-J. Lee, K. Kim, and Y.-S. Lim, Appl. Phys. Lett. **86**, 242101 (2005).

[18] D. Ruzmetov, S. D. Senanayake, V. Narayanamurti, and S. Ramanathan, Phys. Rev. B **77**, 195442 (2008).

[19] J. Sakai and M. Kurisu, Phys. Rev. B - Condens. Matter Mater. Phys. **78**, 2 (2008).

[20] K. Okimura, N. Ezreena, Y. Sasakawa, and J. Sakai, Jpn. J. Appl. Phys. **48**, 065003 (2009).

[21] D. Ruzmetov, G. Gopalakrishnan, C. Ko, V. Narayanamurti, and S. Ramanathan, J. Appl. Phys. **107**, 114516 (2010).

[22] Md. Suruz Mian and K. Okimura, J. Vac. Sci. Technol. A **32**, 041502 (2014).

[23] Md. Suruz Mian, K. Okimura, and J. Sakai, J. Appl. Phys. **117**, 215305 (2015).

[24] Z. Yang, Y. Zhou, and S. Ramanathan, J. Appl. Phys. **111**, 1 (2012).

[25] F. J. Morin, Bell Syst. Tech. J. **37**, 1047 (1958).

[26] Z. Yang, C. Ko, and S. Ramanathan, J. Appl. Phys. **108**, 073708 (2010).

[27] J. Leroy, A. Crunteanu, A. Bessaudou, F. Cosset, C. Champeaux, and J. C. Orlianges, Appl. Phys. Lett. **100**, 213507 (2012).

[28] M. Nakano, K. Shibuya, D. Okuyama, T. Hatano, S. Ono, M. Kawasaki, Y. Iwasa, and Y. Tokura, Nature **487**, 459 (2012).

[29] V. Eyert, Ann. Der Phys. **11**, 650 (2002).

[30] A. Cavalleri, T. Dekorsy, H. H. W. Chong, J. C. Kieffer, and R. W. Schoenlein, Phys. Rev. B - Condens. Matter Mater. Phys. **70**, 1 (2004).

[31] B.-G. Chae, H.-T. Kim, D.-H. Youn, and K.-Y. Kang, Phys. B Condens. Matter **369**, 76 (2005).

[32] J. Wu, Q. Gu, B. S. Guiton, N. P. De Leon, L. Ouyang, and H. Park, Nano Lett. **6**, 2313 (2006).

[33] B.-J. Kim, Y.-W. Lee, B.-G. Chae, S.-J. Yun, S.-Y. Oh, H.-T. Kim, and Y.-S. Lim, Appl. Phys. Lett. **90**, 2 (2007).

[34] M. Imada, A. Fujimori, and Y. Tokura, Rev. Mod. Phys. **70**, 1039 (1998).

[35] C. Ko and S. Ramanathan, Appl. Phys. Lett. **93**, 1 (2008).

[36] M. Rini, A. Cavalleri, R. W. Schoenlein, R. López, L. C. Feldman, R. F. Haglund, L. A. Boatner, and T. E. Haynes, Opt. Lett. **30**, 558 (2005).

[37] J. F. De Natale, P. J. Hood, and A. B. Harker, J. Appl. Phys. **66**, 5844 (1989).

[38] J. S. Lee, M. Ortolani, U. Schade, Y. J.Chang, and T. W. Noh, Appl. Phys. Lett. **90**, 051907 (2007).

[39] K. Okimura and Md. Suruz Mian, J. Vac. Sci. Technol. A **30**, 051502 (2012).

[40] M. Rini, Z. Hao, R. W. Schoenlein, C. Giannetti, F. Parmigiani, S. Fourmaux, J. C. Kieffer, A. Fujimori, M. Onoda, S. Wall, and A. Cavalleri, Appl. Phys. Lett. **92**, 181904 (2008).

[41] M. Soltani, M. Chaker, E. Haddad, R. V. Kruzelecky, and J. Margot, Appl. Phys. Lett. **85**, 1958 (2004).

[42] J. Zhou, Y. Gao, Z. Zhang, H. Luo, C. Cao, Z. Chen, L. Dai, and X. Liu, Sci. Rep. **3**, 1 (2013).

[43] S.-H. Chang, S.-B. Lee, D.-Y. Jeon, S.-J. Park, G.-T. Kim, S.-M. Yang, S.-C. Chae, H.-K. Yoo, B.-S. Kang, M.-J. Lee, and T.-W. Noh, Adv. Mater. **23**, 4063 (2011).

[44] M.-J. Lee, Y. Park, D.-S. Suh, E.-H. Lee, S. Seo, D.-C. Kim, R. Jung, B.-S. Kang, S.-E. Ahn, C. B. Lee, D. H. Seo, Y.-K. Cha, I.-K. Yoo, J.-S. Kim, and B. H. Park, Adv. Mater. **19**, 3919 (2007).

[45] L. Kang, Y. Gao, Z. Chen, J. Du, Z. Zhang, and H. Luo, Sol. Energy Mater. Sol. Cells **94**, 2078 (2010).

[46] S.-H. Bae, S. Lee, H. Koo, L. Lin, B.-H. Jo, C. Park, and Z. L. Wang, Adv. Mater. **25**, 5098 (2013).

[47] T. Driscoll, H.-T. Kim, B.-G. Chae, B.-J. Kim, Y.-W. Lee, N. M. Jokerst, S. Palit, D. R. Smith, M. Di Ventra, and D. N. Basov, Science **325**, 1518 (2009).

[48] Y. V. Pershin and M. Di Ventra, Adv. Phys. **60**, 145 (2011).

[49] T. Hahn, editor , *International Tables for Crystallography Volume A: Space-Group Symmetry*, Fifth (Springer, 2005).

[50] S. Westman, I. Lindqvist, B. Sparrman, G. B. Nielsen, H. Nord, and A. Jart, Acta Chem. Scand. **15**, 217 (1961).

[51] D. B. McWhan, M. Marezio, J. P. Remeika, and P. D. Dernier, Phys. Rev. B **10**, 490 (1974).

[52] M. Marezio, D. B. McWhan, J. P. Remeika, and P. D. Dernier, Phys. Rev. B **5**, 2541 (1972).

[53] G. Andersson, C. Parck, U. Ulfvarson, E. Stenhagen, and B. Thorell, Acta Chem. Scand. **10**, 623 (1956).

[54] G. Andersson, Acta Chem. Scand. **8**, 1599 (1954).

[55] J. M. Longo and P. Kierkegaard, Acta Chem. Scand. **24**, 420 (1970).

[56] J. B. Goodenough, Phys. Rev. **117**, 1442 (1960).

[57] S. Shin, S. Suga, M. Taniguchi, M. Fujisawa, H. Kanzaki, A. Fujimori, H. Daimon, Y. Ueda, K. Kosuge, and S. Kachi, Phys. Rev. B **41**, 4993 (1990).

[58] A. Cavalleri, M. Rini, H. H. W. Chong, S. Fourmaux, T. E. Glover, P. A. Heimann, J. C. Kieffer, and R. W. Schoenlein, Phys. Rev. Lett. **95**, (2005).

[59] J. M. Booth and P. S. Casey, Phys. Rev. Lett. **103**, 086402 (2009).

[60] N. F. Mott, Rev. Mod. Phys. **40**, 677 (1968).

[61] A. Zylbersztejn and N. F. Mott, Phys. Rev. B **11**, 4383 (1975).

[62] T. M. Rice, H. Launois, and J. Pouget, Phys. Rev. Lett. **73**, 3042 (1994).

[63] H.-T. Kim, B.-G. Chae, D.-H. Youn, S.-L. Maeng, G. Kim, K.-Y. Kang, and Y.-S. Lim, New J. Phys. **6**, 52 (2004).

[64] H.-T. Kim, Y.-W. Lee, B.-J. Kim, B.-G. Chae, S.J. Yun, K.-Y. Kang, K.-J. Han, K.-J. Yee, and Y.-S. Lim, Phys. Rev. Lett. **97**, 10 (2006).

[65] R. Eguchi, M. Taguchi, M. Matsunami, K. Horiba, K. Yamamoto, Y. Ishida, a. Chainani, Y. Takata, M. Yabashi, D. Miwa, Y. Nishino, K. Tamasaku, T. Ishikawa, Y. Senba, H. Ohashi, Y. Muraoka, Z. Hiroi, and S. Shin, Phys. Rev. B - Condens. Matter Mater. Phys. **78**, 1 (2008).

[66] J. I. Sohn, H. J. Joo, D. Ahn, H.-H. Lee, A. E. Porter, K. Kim, D.-J. Kang, and M. E. Welland, Nano Lett. **9**, 3392 (2009).

[67] K. Kosuge, H. Okinaka, and S. Kachi, IEEE Trans. Magn. **8**, 581 (1972).

[68] M. Demeter, M. Neumann, and W. Reichelt, Surf. Sci. **454**, 41 (2000).

[69] H. Katzke, P. Tolédano, and W. Depmeier, Phys. Rev. B **68**, 1 (2003).

[70] H. M. Zeng, Y. Zhao, Y. J. Hao, Q. Y. Lai, J. H. Huang, and X. Y. Ji, J. Alloys Compd. **477**, 800 (2009).

[71] J. P. Pouget, H. Launois, J. P. D'Haenens, P. Merenda, and T. M. Rice, Phys. Rev. Lett. **35**, 873 (1975).

[72] K. Okimura, T. Watanabe, and J. Sakai, J. Appl. Phys. **111**, (2012).

[73] T. Watanabe, K. Okimura, T. Hajiri, S. Kimura, and J. Sakai, J. Appl. Phys. **113**, 163503 (2013).

[74] K. Okimura, Nurul Hanis Azhan, T. Hajiri, S. I. Kimura, M. Zaghrioui, and J. Sakai, J. Appl. Phys. **115**, (2014).

[75] Y. Oka, S. Sato, T. Yao, and N. Yamamoto, J. Solid State Chem. **598**, 594 (1998).

[76] W. Wang, B. Jiang, W. Xiong, H. Sun, Z. Lin, L. Hu, J. Tu, J. Hou, H. Zhu, and S. Jiao, Sci. Rep. **3**, 3383 (2013).

[77] Y. Oka, T. Yao, N. Yamamoto, Y. Ueda, and A. Hayashi, J. Solid State Chem. **105**, 271 (1993).

[78] Q. Wang, J. Pan, M. Li, Y. Luo, H. Wu, L. Zhong, and G. Li, J. Mater. Sci. Technol. **2**, 2 (2014).

[79] L. A. Ladd and W. Paul, Solid State Commun. **7**, 425 (1969).

[80] C. Ko and S. Ramanathan, J. Appl. Phys. **104**, 086105 (2008).

[81] D. Ruzmetov, D. Heiman, B. B. Claflin, V. Narayanamurti, and S. Ramanathan, Phys. Rev. B - Condens. Matter Mater. Phys. **79**, 153107 (2009).

[82] J. Lu, K. G. West, and S. A. Wolf, Appl. Phys. Lett. **93**, 2 (2008).

[83] A. Gupta, R. Aggarwal, P. Gupta, T. Dutta, R. J. Narayan, and J. Narayan, Appl. Phys. Lett. **95**, 111915 (2009).

[84] E. Strelcov, Y. Lilach, and A. Kolmakov, Nano Lett. **9**, 2322 (2009).

[85] J. Baik, M. Kim, and C. Larson, J. Phys. Chem. Lett. **112**, 13328 (2008).

[86] J. Cao, E. Ertekin, V. Srinivasan, W. Fan, S. Huang, H. Zheng, J. W. L. Yim, D. R. Khanal, D. F. Ogletree, J. C. Grossman, and J. Wu, Nat. Nanotechnol. **4**, 732 (2009).

[87] J. Wei, Z. Wang, W. Chen, and D. H. Cobden, Nat. Nanotechnol. **4**, 420 (2009).

[88] R. Lopez, T. E. Haynes, L. A. Boatner, L. C. Feldman, and R. F. Haglund, Phys. Rev. B **65**, 224113 (2002).

[89] J. Liu, Q. Li, T. Wang, D. Yu, and Y. Li, Angew. Chem. Int. Ed. Engl. **43**, 5048 (2004).

[90] M. Son, J. Lee, J. Park, J. Shin, G. Choi, S. Jung, W. Lee, S. Kim, S. Park, and H. Hwang, IEEE Electron Device Lett. **32**, 1579 (2011).

[91] K. Okimura and N. Kubo, Thin Solid Films **515**, 4992 (2007).

[92] Md. Suruz Mian and K. Okimura, Jpn. J. Appl. Phys. **53**, 035802 (2014).

[93] H. Zhou, M. F. Chisholm, T.-H. Yang, S. J. Pennycook, and J. Narayan, J. Appl. Phys. **110**, 073515 (2011).

[94] M. B. Sahana, M. S. Dharmaprakash, and S. A. Shivashankar, J. Mater. Chem. **12**, 333 (2001).

[95] J. Nag, R. F. Haglund, E. A. Payzant, and K. L. More, J. Appl. Phys. **112**, 1 (2012).

[96] P. Dagur, Anil U. Mane, and S. A. Shivashankar, J. Cryst. Growth **275**, e1223 (2005).

[97] M. Tangirala, K. Zhang, D. Nminibapiel, V. Pallem, C. Dussarrat, W. Cao, T. N. Adam, C. S. Johnson, H. E. Elsayed-Ali, and H. Baumgart, ECS J. Solid State Sci. Technol. **3**, N89 (2014).

[98] L. L. Fan, S. Chen, Z. L. Luo, Q. H. Liu, Y. F. Wu, L. Song, D. X. Ji, P. Wang, W. S. Chu, C. Gao, C. W. Zou, and Z. Y. Wu, Nano Lett. **14**, 4036 (2014).

[99] M. Nagashima and H. Wada, J. Mater. Res. **12**, 416 (1997).

[100] D. Alie, L. Gedvilas, Z. Wang, R. Tenent, C. Engtrakul, Y. Yan, S. E. Shaheen, A. C. Dillon, and C. Ban, J. Solid State Chem. **212**, 237 (2014).

[101] J.-P. Fortier, B. Baloukas, O. Zabeida, J. E. Klemberg-Sapieha, and L. Martinu, Sol. Energy Mater. Sol. Cells **125**, 291 (2014).

[102] Nurul Hanis Azhan, K. Su, K. Okimura, and J. Sakai, J. Appl. Phys. **117**, 185307 (2015).

[103] K. Okimura, J. Sakai, and S. Ramanathan, J. Appl. Phys. **107**, 063503 (2010).

[104] Y. Nihei, Y. Sasakawa, and K. Okimura, Thin Solid Films **516**, 3572 (2008).

[105] S. Saitzek, F. Guinneton, G. Guirleo, L. Sauques, K. Aguir, and J. R. Gavarri, Thin Solid Films **516**, 891 (2008).

[106] N. Yuan, J. Li, G. Li, and X. Chen, Thin Solid Films **515**, 1275 (2006).

[107] J. Li and J. Dho, J. Cryst. Growth **312**, 3287 (2010).

[108] J. Jian, A. Chen, W. Zhang, and H. Wang, J. Appl. Phys. **114**, 1 (2013).

[109] A. D. Rata, S. Vongtragool, D. O. Boerma, and T. Hibma, Thin Solid Films **400**, 120 (2001).

[110] A. Gupta, J. Narayan, and T. Dutta, Appl. Phys. Lett. **97**, 95 (2010).

[111] K. Kato, P. K. Song, H. Odaka, and Y. Shigesato, Jpn. J. Appl. Phys. **42**, 6523 (2003).

[112] T. W. Hickmott, J. Appl. Phys. **33**, 2669 (1962).

[113] J. F. Gibbons and W. E. Beadle, Solid. State. Electron. **7**, 785 (1964).

[114] G. Dearnale, A. M. Stoneham, and D. V. Morgan, Rep. Prog. Phys. **33**, 1129 (1970).

[115] B. J. Choi, D. S. Jeong, S. K. Kim, C. Rohde, S. Choi, J. H. Oh, H. J. Kim, C. S. Hwang, K. Szot, R. Waser, B. Reichenberg, and S. Tiedke, J. Appl. Phys. **98**, 1 (2005).

[116] Z. Jirák, S. Krupička, Z. Šimša, M. Dlouhá, and S. Vratislav, J. Magn. Magn. Mater. **53**, 153 (1985).

[117] K. Knížek, Z. Jirák, E. Pollert, F. Zounová, and S. Vratislav, J. Solid State Chem. **100**, 292 (1992).

[118] A. Asamitsu, Y. Tomioka, H. Kuwahara, and Y. Tokura, Nature **388**, 1995 (1997).

[119] P. F. Bongers and U. Enz, Philips Res. Repts **21**, 387 (1966).

[120] K. van Steensel, F. van de Burg, and C. Kooy, Philips Res. Repts **22**, 170 (1967).

[121] Y. Taketa, F. Kato, M. Nitta, and M. Haradome, Appl. Phys. Lett. **27**, 212 (1975).

[122] B. Fisher, J. Appl. Phys. **49**, 5339 (1978).

[123] C. N. Berglund, IEEE Trans. Electron Devices **16**, 432 (1969).

[124] C. N. Berglund and A. Jayaraman, Phys. Rev. **1022**, (1969).

[125] J. Duchene, M. Terraillon, P. Pailly, and G. Adam, Appl. Phys. Lett. **19**, 115 (1971).

[126] Z. Yang, Y. Zhou, and S. Ramanathan, J. Appl. Phys. **111**, 014506 (2012).

[127] M. P. Shaw, IEEE Trans. Electron Devices **26**, 1766 (1979).

[128] J. S. Lee, M. Ortolani, A. Ginolas, Y. J. Chang, T. W. Noh, and U. Schade, Phys. C **460-462**, 549 (2007).

[129] K. Okimura and J. Sakai, Jpn. J. Appl. Phys. **46**, pp. L813 (2007).

[130] C. Ko and S. Ramanathan, Appl. Phys. Lett. **93**, 8 (2008).

[131] D. Ruzmetov, G. Gopalakrishnan, J. Deng, V. Narayanamurti, and S. Ramanathan, J. Appl. Phys. **106**, 083702 (2009).

[132] J. Sakai, M. Zaghrioui, V. Ta Phuoc, S. Roger, C. Autret-Lambert, and K. Okimura, J. Appl. Phys. **113**, 123503 (2013).

[133] P. P. Boriskov, A. A. Velichko, A. L. Pergament, G. B. Stefanovich, and D. G. Stefanovich, Tech. Phys. Lett. **28**, 406 (2002).

[134] A. L. Pergament, P. P. Boriskov, A. A. Velichko, and N. A. Kuldin, J. Phys. Chem. Solids **71**, 874 (2010).

[135] G. Seo, B.-J. Kim, Y.-W. Lee, and H.-T. Kim, Appl. Phys. Lett. **100**, 011908 (2012).

[136] V. S. Aliev, S. G. Bortnikov, and I. A. Badmaeva, J. Appl. Phys. **115**, 204511 (2014).

[137] C.-R. Cho, S. Cho, S. Vadim, R. Jung, and I. Yoo, Thin Solid Films **495**, 375 (2006).

[138] Z. Yang, S. Hart, C. Ko, A. Yacoby, and S. Ramanathan, J. Appl. Phys. **110**, 033725 (2011).

[139] G. Seo, B.-J. Kim, C. Ko, Y. Cui, Y.-W. Lee, J.-H. Shin, S. Ramanathan, and H.-T. Kim, IEEE Electron Device Lett. **32**, 1582 (2011).

[140] J. Sakai, J. Appl. Phys. **104**, 73703 (2008).

[141] Y. Cui, X. Wang, Y. Zhou, R. Gordon, and S. Ramanathan, J. Cryst. Growth **338**, 96 (2012).

CHAPTER 2

Growth of VO_2 Films on Ti/Si Substrates by Inductively Coupled Plasma-Assisted Sputtering Method

Chapter 2 Growth of VO_2 Films on Ti/Si Substrates by Inductively Coupled Plasma-Assisted Sputtering Method

2.1 Introduction

As described in chapter 1, VO_2 exhibits an abrupt insulator-metal transition (IMT) at a relatively low temperature of 68ºC.[1] It has been reported that the IMT of VO_2 can be triggered by the electric field, which cause VO_2 to be the most promising material for the electrical switching devices. Voltage triggered resistance switching (VTRS) in VO_2-based two-terminal planar type devices was being widely investigated.[2–4] However, there has been a restriction in both switching voltage and current, while in this type the threshold switching voltage and current depend on the gap between electrodes.[2,3,5–9] Therefore, in order to investigate the intrinsic properties of VTRS, it is highly required to achieve a layered type device, in which VO_2 film is deposited on the conductive layer (bottom electrode, BE) as was shown in Fig. 1-4 in chapter 1.[10] Some research groups tried to achieve the out-of-plane configuration with the VO_2 films deposited on heavily doped Si wafers,[10–13] Nb-doped $SrTiO_3$ substrates,[14] and Pt layers.[15–17] However, the out-of-plane IMT, the crystal morphology, and the interface between the VO_2 film and the BE were not investigated. Many research groups have performed higher temperature depositions by the PLD[18] method for the sample fabrication, in order to achieve a stoichiometric VO_2 films with a good crystallinity. Among those deposition techniques, reactive magnetron sputtering is advantageous for growing thin films on various substrates such as Al_2O_3, Si, and glass, at relatively low temperatures of around 400~500ºC.[19–21] However, in layered type device, substrate temperature of more than 400ºC might cause the interface diffusion between the VO_2 film and the BE. So, it is highly desirable to introduce a low-temperature deposition technique to realize this layered type configuration. It has been reported that an assistance of the plasma in sputtering method is effective to improve crystallization at a relatively low temperature. In this study, inductively coupled plasma-assisted sputtering (ICPS) was introduced, which is rather advantageous for crystallization at a low temperature.[22,23] In VO_2-based two-terminal planar type devices, different types of electrode such as Au,[24] Au/Ti,[2,3] Au/Cr,[7] Au/Ni,[25] and Pd[10] were investigated. However, the work functions of Au and Pd materials are rather higher than that of the VO_2 films. So, it remains to be questioned if either an Ohmic contact is achieved between the VO_2 film and the electrode during the *I-V* measurements, since VO_2 is reported to behave as a n-type semiconductor[26,27] with a work function of about 4.9 eV.[28]

In this section, Ti was selected as a bottom electrode because of its high melting temperature and low cost for fabrication. Furthermore, the low work function of Ti (4.14 eV) can be able to make an Ohmic contact with VO_2 film.The growth of VO_2 film on Ti/Si substrates with the aim of achieving a layered type configuration was investigated by using the ICP-assisted sputtering method. Figure2-1

presents the schematic of VO_2/Ti/Si layered structure.

This chapter is organized as follows. Firstly, a minute description on conventional sputtering (CS), ICP –assisted sputtering (ICPS) and *R-T* measurement method were given. Then, characterization of the deposited Ti films on p-Si (100) substrates by the ICP-assisted sputtering method was performed in order to confirm its ability to work as a bottom electrode. After that, the deposition conditions and the crystalline properties of VO_2 films on the Ti films by the ICP-assisted sputtering method was described. Characterization of films with XRD patterns and out-of-plane *R-T* characteristics were given. Then a comparison of ICPS with CS was delivered. Plasma diagnosis with including ion energy distributions, plasma space potential, and optical emissions of O radical (O*) was presented with the aim of clarifying the low-temperature crystallization of VO_2 in ICPS. It is well-known that the energetic ion irradiation promotes the densification of films in various materials, including metals and compounds like TiN and TiO_2.[29–31] On the other hand, as for the materials in which the good crystallinity is required to emerge their intrinsic properties, the effect of ion irradiation should be discussed in details as a factor that dominates the crystalline formation.[32,33] Subsequently, surface and cross-sectional field effect scanning electron microscopic (FE-SEM) images, XPS depth profiles were presented. Finally, current-voltage (*I-V*) characteristics were presented for the fabricated samples.

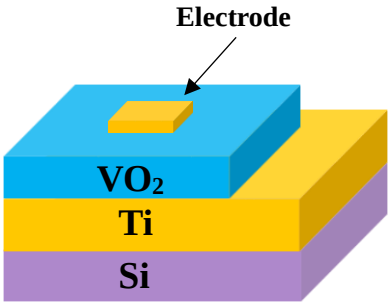

Fig. 2-1 Schematic of VO_2/Ti/Si layered structure.

2.2. Experimental Procedure

2.2.1 Conventional Sputtering (CS)

Reactive sputtering is one kind of sputtering, in which the films are formed by chemical reaction between the target materials and gases. In most cases for oxide formation O_2 gas is introduced as a reactive gas. In conventional sputtering (CS) method, electrons trapped in the magnetic field due to the establishment of the magnet on the back side of the target contribute to a dense plasma, which leads to high-speed film depositions. CS method is applicable deposition for oxide and nitride films. At present, CS sputtering is widely used for industrial coating technology, also in advanced research fields.

In this work, CS method was applied for sample fabrication. Figure 2-2 shows the schematic of CS method used in this study.

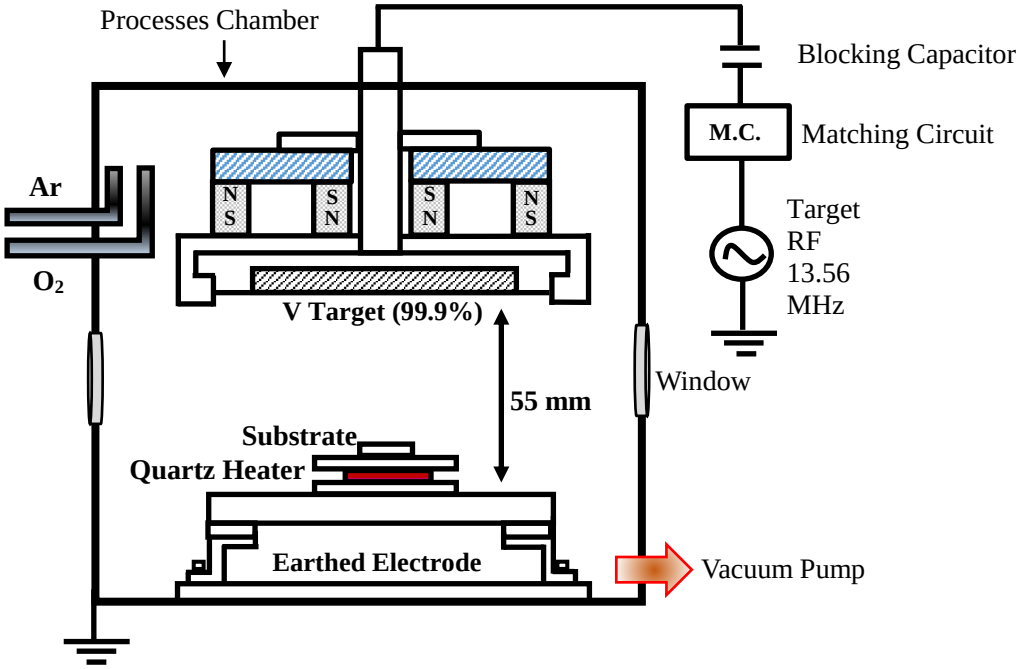

Fig. 2-2 Schematic of rf magnetron sputtering apparatus.

The cathode (target), earthed electrode (105 mm φ), quartz heater, and thermocouple were placed inside the chamber. In this study, vanadium metal (100 mm φ, 3N) with purity of 99.9% was used as a target material. Radio frequency (rf) power of 13.56 MHz was supplied to the target through a π type matching circuit. The distance between the target and the heater were maintained at 55 mm. Two rotary pumps and three turbo-molecular pumps (TMP) were used for pumping the chamber. The

degree of vacuum was monitored by an ionized vacuum gauge apparatus. The substrate was placed on the heater, in which the heating current was supplied by a Slidax. Substrate temperature was monitored by a K-type thermocouple. The processes chamber and the target were cooled by water. Flow rates of Ar and O_2 gases were controlled by mass flow controllers.

2.2.2 Inductively Coupled Plasma-Assisted Sputtering (ICPS) Method

As described in chapter 1, several deposition techniques such as sputtering, PLD, and CVD has been examined for depositing VO_2 films.[18,34,35] In PLD technique, VO_2 films revealed a good crystallinity at deposition temperature of more than 500ºC.[18,21,36–41] In sputtering method, VO_2 films show a better crystallinity above 400ºC.[19,42,43] However, it is difficult to produce a stoichiometric VO_2 films with a sharp IMT below 400ºC in sputtering and PLD techniques. The crystallinity and IMT of VO_2 films strongly depend on the substrate temperature, where lower substrate temperature generally deteriorates the crystallinity of VO_2. However, higher substrate temperature tends to cause diffusion in the interface.[44] Due to this matter, it is highly required to introduce another deposition technique to produce VO_2 films with a good crystallinity at a low temperature of around 200ºC. In this work, the ICP-assisted sputtering (ICPS) method was introduced as a deposition method which enables low-temperature deposition. Figure 2-3 shows a schematic of ICP-assisted sputtering apparatus used in this study.

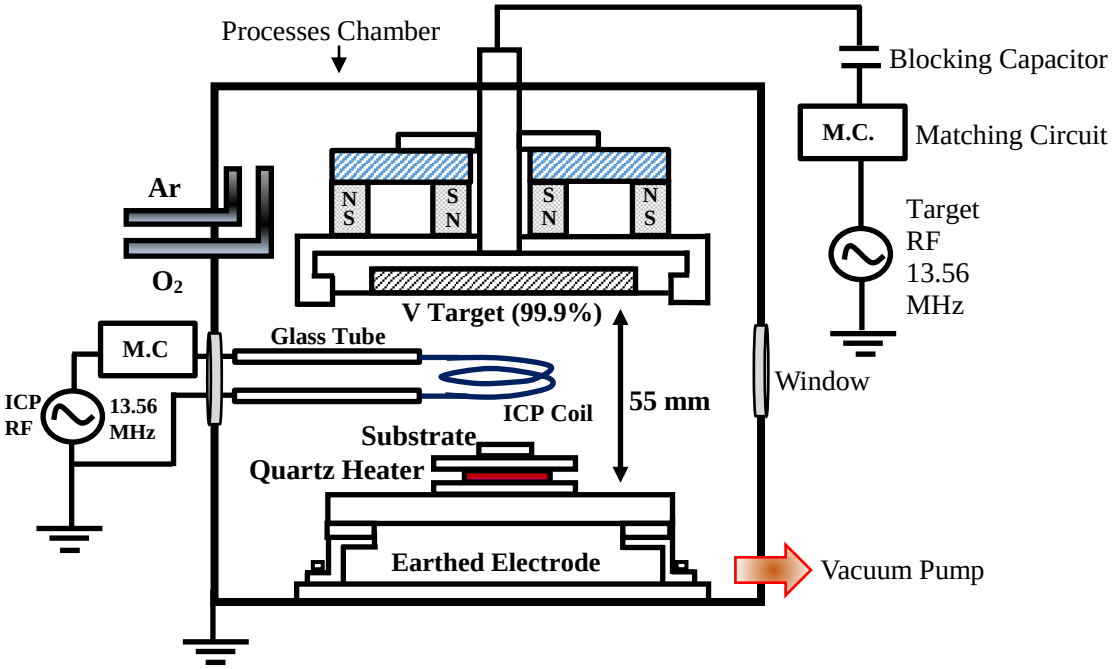

Fig. 2-3 Schematic of ICP-assisted sputtering apparatus.

ICPS is a method, in which a two-turn coil was inserted between the target and the substrate in the conventional rf magnetron sputtering apparatus as shown in Fig. 2-3. The ICP-coil was made from a SUS 304 tubing (1/8 in.) and the diameter of the coil was 85 mm. The coil was cooled by water. The radio frequency of 13.56 MHz was supplied to the coil *via* a matching circuit in order to produce the inductively coupled plasma. The other configuration of the system is the same as the RF magnetron sputtering apparatus. In ICP-assisted sputtering the plasma density increases and the target self-bias is rather low compared to the conventional RF magnetron sputtering.

2.2.3 Resistance-Temperature (*R-T*) Measurement Set-up and Evolution of *R-T* Characteristics

(a) *R-T* Measurement Set-up

R-T characteristics is referred to as resistance change against temperature. As previously described, VO_2 is an oxide that shows an insulator-metal transition (IMT) near 68°C, where several orders of magnitude change in resistance is occurred. After the fabrication of the sample, the growth of crystalline VO_2 film can be confirmed by performing *R-T* characteristic measurement.

In this study, the *R-T* characteristics were measured by using two-probe method. Figure 2-4 shows the schematic measurement method of the *R-T* characteristics.

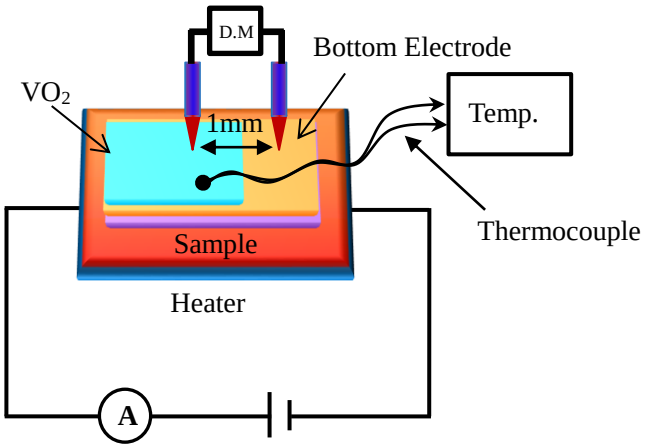

Fig. 2-4 Schematic of *R-T* characteristics measurement method.

Generally, *R-T* characteristic measurement was performed by contacting both probes onto the VO_2 film deposited on Si substrates, which is known as a planar direction measurement. In this work, one probe contacted onto the VO_2 film, while another one contacted on the bottom electrode. This method is called as an out-of-plane direction measurement. During the measurements, the sample was placed on the heater, where, the heating current was controlled carefully, since the transition temperature (T_{IMT}) of VO_2 strongly depends on the heating speed.

(b) Evolution of *R*-*T* Characteristics

Figure 2-5 shows the *R*-*T* characteristics for the sample prepared on *c*-Al_2O_3 substrate by ICP-assisted sputtering method at a substrate temperature of 300°C. More than three orders of magnitude change in resistance was observed. IMT properties were characterized by the initial resistance (or resistance at room temperature), R_{RT}, resistance at 100ºC, R_{100}, transition temperature T_{IMT} ($T_{IMT\text{-}H}$ for heating and $T_{IMT\text{-}C}$ for cooling), magnitude of resistance change, ΔR, and hysteresis width ΔH. T_{IMT} is derived from the peak of the derivative (d ($\log_{10}R$)/dT) curve (inset figure). The ΔR was calculated using resistance values before and after the transition at both edges of the derivative curve and ΔH was defined by the difference between $T_{IMT\text{-}H}$ and $T_{IMT\text{-}C}$.

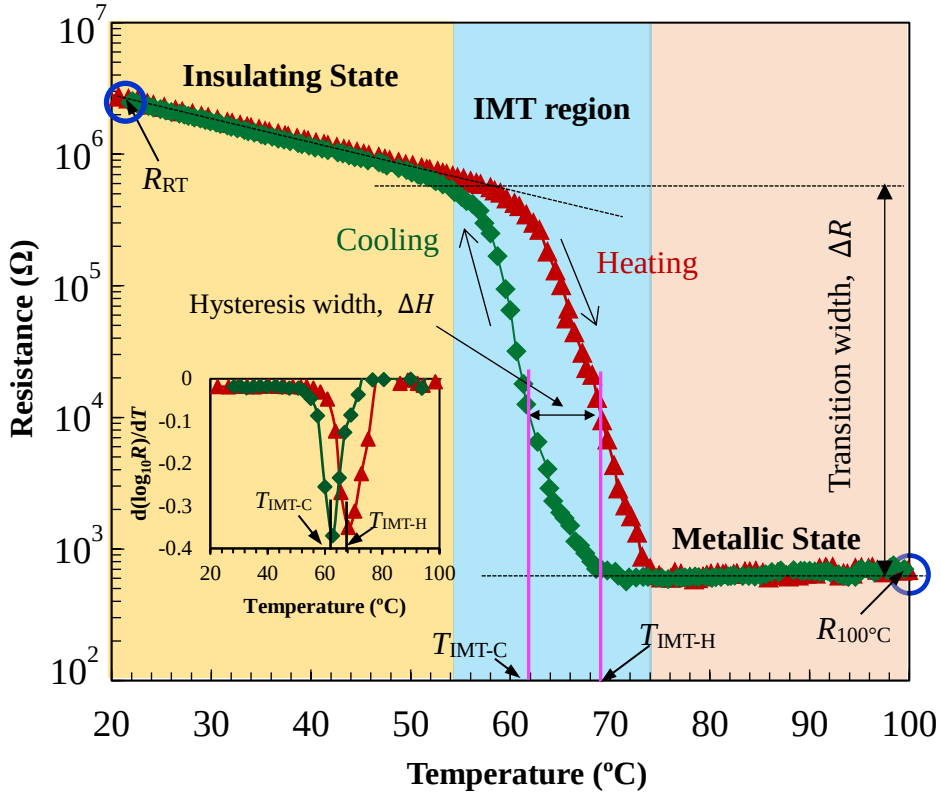

Fig. 2-5 *R*-*T* characteristics evolution.

2.3 Results and Discussion

2.3.1 Fabrications of Ti Electrodes and Its Characterizations

2.3.1-1 Deposition Conditions and Electrical Properties

In this work, before the deposition of VO_2 films, Ti films were deposited on p-Si (100) substrates (Ti/Si) by ICP-assisted sputtering method using a Ti target with a purity of 99.99%. Before the substrates were placed in the chamber, they were cleaned ultrasonically using acetone to remove the organic matters and other impurity ions adhered to the surface, and then rinsed using pure water. During the deposition, the substrate temperature and Ar pressure were kept constant at 200°C and 1.2 Pa, respectively. The deposition was performed for 10 min, producing films with a thickness of about 300 nm. The target-rf power and ICP-rf power were 200 W and 150 W, respectively. The resistivity of the fabricated Ti film was $1 - 2 \times 10^{-4}$ Ωcm. The resistivity was measured by four-probe method. Although the measured resistivity is one order higher than that of the bulk Ti (4.27×10^{-5} Ωcm), yet it is possible to be used as an electrode. The deposition conditions were summarized in Table 2-1.

Table 2-1 Deposition conditions and electrical resistivity of deposited Ti films.

Target	Ti (99.99%)
Substrate	p-Si (100)
Substrate Temperature (°C)	200
Ar Pressure (Pa)	1.2
Ar gas flow (sccm)	70
Target-rf Power (W)	200
ICP-rf Power (W)	150
Deposition Time (min)	10
Film Thickness (nm)	300
Resistivity (Ωcm)	$1\text{-}2\times10^{-4}$

2.3.1-2 XRD Pattern of Ti/Si Substrates

Crystallization of Ti films was analyzed by X-ray diffraction, XRD (PANalytical X'pert MRD) by using Cukα radiation (λ=1.5418Å). Figure 2-6 shows the XRD patterns of the deposited film. The horizontal axis denotes diffraction angle and vertical axis indicates the peak intensity. Peaks at 2θ = 32.75° and 69.10° are corresponding to Si (200) and (400) planes. Peaks at 2θ = 35.05°, 38.05°, 39.95°, 52.29º, 62.86º, 74.85º, and 77.25º, are corresponding to Ti (100), (002), and (101), (102), (110), (200), and (112) planes, respectively. These results suggest that Ti films grow on Si substrates (Ti/Si) in a polycrystalline manner.

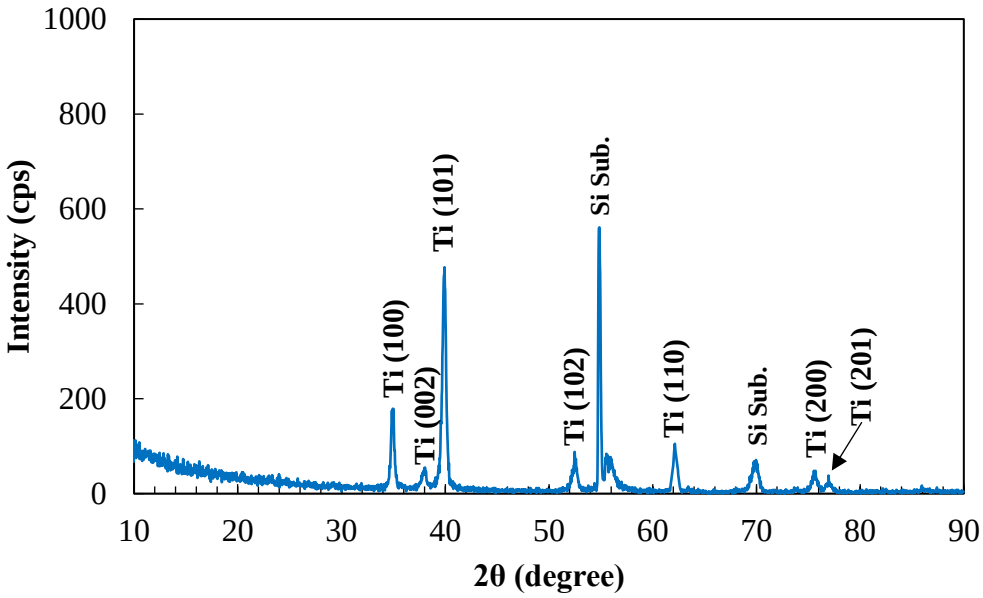

Fig. 2-6 XRD pattern for the Ti film deposited on Si substrates.

2.3.2 Deposition of VO_2 Films on Ti/Si Substrates by ICPS

2.3.2-1 Deposition Conditions of VO_2 Films in ICPS

After confirming the crystallization of Ti films on p-Si (100) substrates, VO_2 films were deposited on Ti/Si substrates by using the ICPS. In order to obtain a stoichiometric VO_2 film, it is important to choose the deposition conditions. As previously described, the crystallization of VO_2 film strongly depends on the substrate materials, substrate temperature (*T*s), and deposition technique. In this work, the deposition was first performed at *T*s of 400°C. The target-rf power, ICP-rf power, O_2 flow rate, $Ar+O_2$ total pressure, and deposition time were kept constant at 200 W, 200 W, 1.0 sccm, 0.5 Pa, and 20 min, respectively. The film thickness of VO_2 films was measured to be about 200 nm. The layered structure of the device was investigated by the cross-section SEM measurement. Crystalline evaluation of VO_2 films was carried out by XRD measurement. The out-of-plane *R*-*T* characteristics were measured by the two-probe method. Field emission scanning electron microscopy (FE-SEM) observations (HITACHI S-4800) were conducted for structural analysis, and x-ray photoelectron spectroscopy (XPS) was performed (Quantum 2000; ULVAC-PHI, Inc.) for analyzing the chemical states and the atomic composition along the out-of-plane direction. Finally, the current-voltage (*I*–*V*) characteristics were investigated using a curve tracer (SCT-2FR; Kokusai Denki Co. Ltd.). The deposition conditions for the VO_2 films were summarized in Table 2-2.

Table 2-2 Deposition conditions of VO_2 films in ICPS.

Target	V (99.9%)
Substrate	Ti/Si
Substrate Temperature (°C)	100 to 400
($Ar+O_2$) Pressure (Pa)	0.5
Ar gas flow (sccm)	50
O_2 flow (sccm)	1.0
Target-rf Power (W)	250
ICP-rf Power (W)	200
Deposition Time (min)	20

2.3.2-2 *R-T* Characteristics and XRD Pattern of VO_2 Film Deposited on Ti/Si Substrates at 400°C

As described in the previous section, VO_2 films were firstly deposited at 400°C by the ICP-assisted sputtering method. Figure 2-7 (a) shows the out-of-plane *R-T* characteristics of the sample prepared at 400ºC on Ti/Si substrates. The low initial resistance of about 3.3 kΩ was observed and no transition behavior was observed; only a semiconducting-like decrease in resistance was observed with increasing temperature.

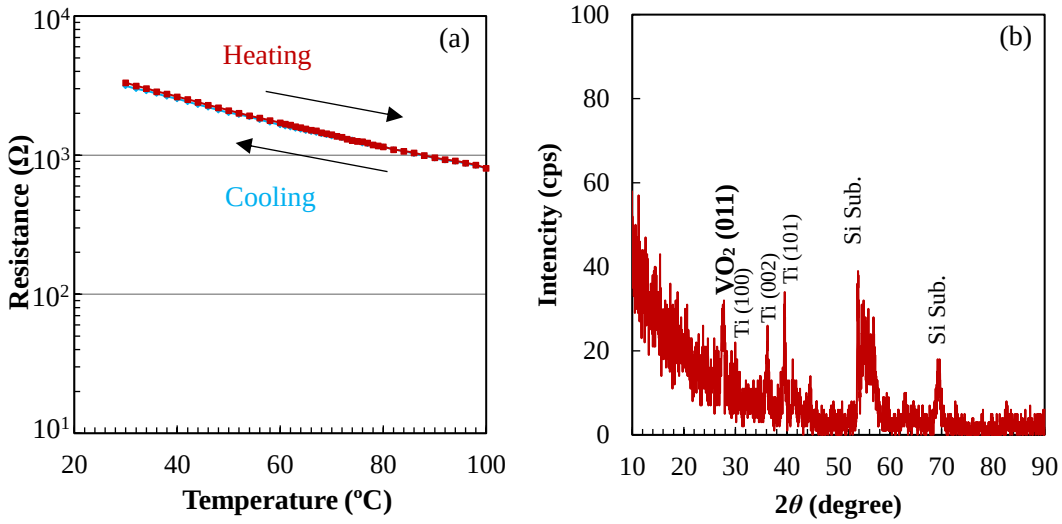

Fig. 2-7 (a) Out-of-plane *R-T* characteristics and (b) XRD pattern for the sample fabricated at 400ºC.

Figure 2-7 (b) displays the XRD 2θ scan pattern of the prepared sample. Peaks at 2θ = 35.02º, 38.15º, and 40.01º corresponded to hcp-Ti (100), (002), and (101) planes, respectively. A weak diffraction from the monoclinic VO_2 (011) plane was observed at 27.85º. Interestingly, partial peeling of Ti films was also observed in the fabricated sample. In addition, as the substrate temperature increased to 450ºC, Ti films was totally peeled off. Due to that, *R-T* characteristics and XRD pattern could not be measured. Based on these results, it can be concluded that the growth of VO_2 films on the Ti/Si substrates might be difficult to be performed at substrate temperatures higher than 400ºC.

2.3.2-3 XRD Patterns of VO_2 Films Deposited on Ti/Si Substrates by the ICPS at Different Substrate Temperatures

As described in the section 2.3.2-2, it is difficult to grow crystalline VO_2 films in the substrate temperatures of 400ºC and 450ºC. In this section, the crystal growth of VO_2 films on Ti/Si substrates at comparatively lower substrate temperatures was delivered. The substrate temperatures, *T*s was varied from 100ºC to 350ºC. Other deposition conditions were kept constant during deposition. The crystal growth of VO_2 films was evaluated by the XRD 2θ scan method with a low X-ray incident angle of 2°.

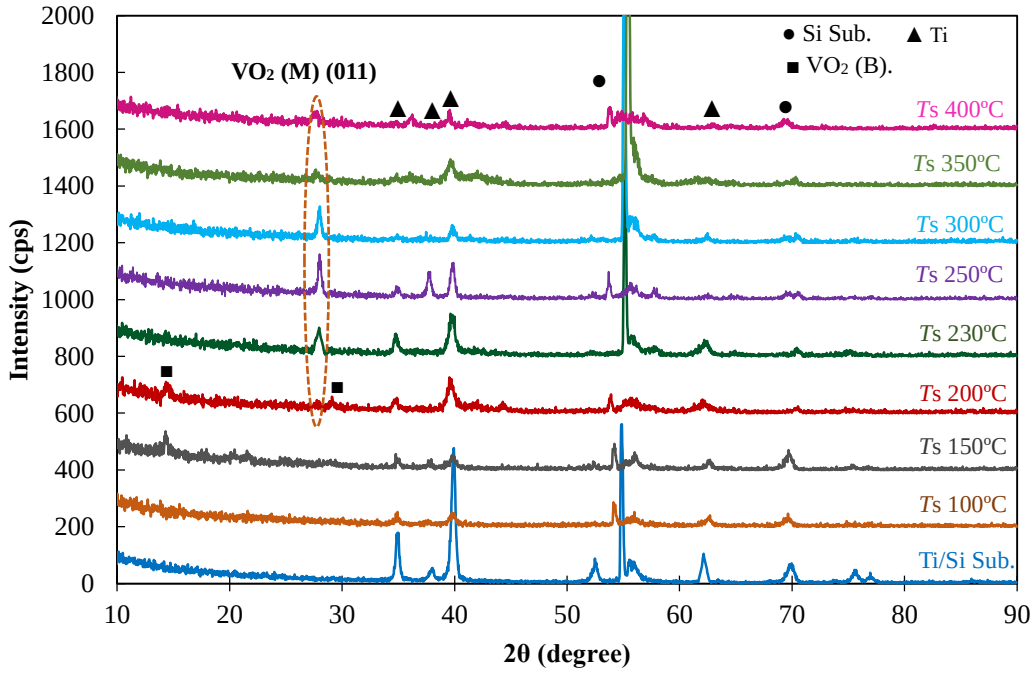

Fig. 2-8 XRD 2θ scan patterns of the samples prepared at different substrate temperatures.

Figure 2-8 shows the XRD 2θ scan patterns of the samples prepared at different substrate temperatures. In Fig. 2-8, diffractions from hcp-Ti (100), (002), (101), (102), (110), (200), and (112) planes were detected at 2θ = 25.05°, 38.05°, 39.95°, 52.29°, 62.86°, 74.85°, and 77.25°, respectively. As described in section 2.3.1-2, the growth of Ti films on Si substrates in a polycrystalline manner was confirmed.

Diffraction from the monoclinic VO_2 (011) plane was observed at 2θ = 27.85° for the samples prepared from 200 to 400°C, suggesting the crystalline growth of VO_2 film on Ti/Si substrates. The peak intensity increased with decreasing *T*s until 250°C. On the other hand, the peak intensity decreased with decreasing *T*s from 230ºC to 200ºC. New peaks were observed at 2θ = 14.39° and

29.07° corresponding to the (001) and (002) planes of VO_2 (B). VO_2 (B) is a polymorph of VO_2, which is reported to be usually formed by the chemical solution method at relatively low temperatures.[45–49] VO_2 (B) reveal a layered-type structure and has been collecting much attentions for a cathode electrode in secondary Li-ion battery. A single VO_2 (B) phase was obtained at 150°C in Fig. 2-8. At 100°C, no peak was observed, indicating the crystalline growth was no longer achievable. The degradation of VO_2 crystalline at high temperatures was due to the diffusion of O atoms and the oxidation of Ti atoms as shown later. In contrast, the temperatures lower than 250°C are insufficient to achieve the crystalline growth of VO_2 films. Based on these results, it was understood that 250°C is the most suitable substrate temperature for depositing VO_2 films on the Ti/Si substrates by using the ICP assisted sputtering method from the standpoint of crystallinity.

2.3.2-4 *R-T* Characteristics of VO_2 Films Deposited on Ti/Si Substrates by the ICPS at Different Substrate Temperatures

In this section, the IMT properties of the samples deposited at different substrate temperatures were delivered. Herein, *R-T* characteristics were shown only for the samples prepared from 200 to 400ºC, since crystal growth of VO_2 was not observed at 100ºC and 150ºC. Figures 2-9 (a) and (b) represent the out-of-plane *R-T* characteristics of the films fabricated at a higher temperature range (300 - 400ºC) and a lower temperature range (200 - 250ºC), respectively.

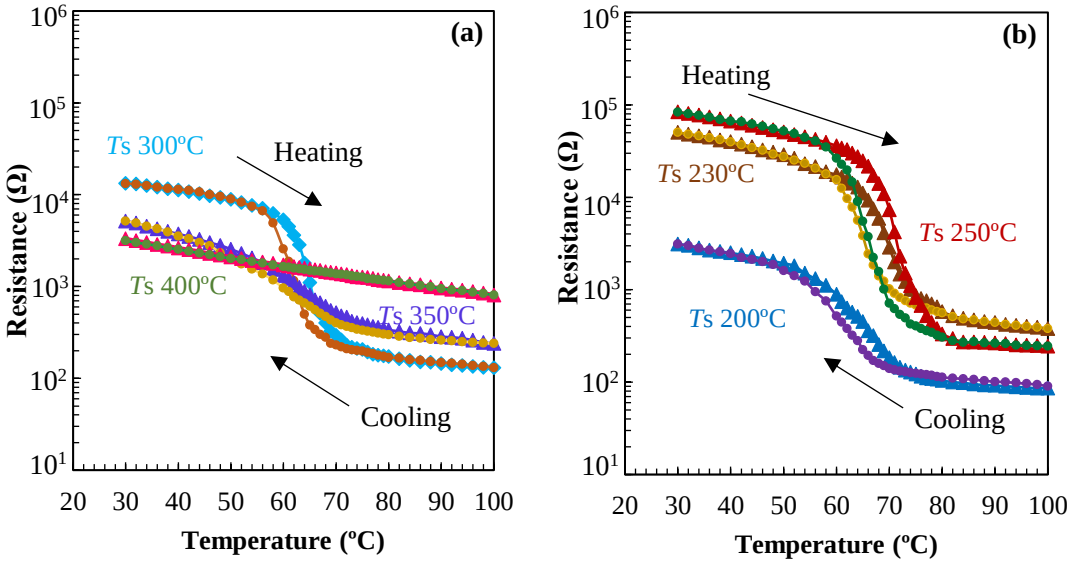

Fig. 2-9 Out-of-plane *R-T* characteristics of the samples prepared at different substrate temperatures, (a) for 300 - 400ºC and (b) for 200 - 250ºC, respectively.

The sample deposited at 350ºC showed a weak insulator-metal transition (IMT) with near one order of resistance change, while no transition was observed for the sample of 400ºC. In this sample, R_{RT} increased to 5.1 kΩ compared to the 3.3 kΩ of 400ºC. The increase of initial resistance is important to achieve a large resistance change. A sharp IMT with more than 1.5 orders of magnitude change in resistance was achieved in the sample of 300ºC. These results are corresponding to the XRD patterns, wherein higher peak intensity was observed for the sample deposited at 300ºC in comparison to samples of 350ºC and 400ºC. The $T_{IMT\text{-}H}$ and $T_{IMT\text{-}C}$ of 66ºC and 62ºC with ΔH of 4ºC and ΔR of 1.85 were observed. The R_{RT} was increased to 13.2 kΩ compared to 5.1 kΩ at 350ºC. These results suggest that the IMT is improved in lower substrate temperature than that in higher substrate temperature. Figure 2-9 (b) shows the *R-T* characteristics when the substrate temperature further decreased from 300ºC to 200ºC. In Fig. 2-9 (b), a sharp IMT with more than 2.5 orders of magnitude change in resistance was observed for the sample deposited at 250ºC, with $T_{IMT\text{-}H}$ and $T_{IMT\text{-}C}$ at 71ºC and 67ºC with a ΔH of 4ºC and ΔR of 2.6 with the highest R_{RT} of 83.26 kΩ. The ΔR of 2.6 orders was the highest

value achieved for the layered type device, while another research groups failed to realize the IMT due to the low initial resistance of films. For the film deposited at 230ºC, IMT with T_{IMT-H} and T_{IMT-C} at 72ºC and 65ºC, with a wider ΔH of 7ºC (compared to the samples of 250 and 300ºC) was observed. ΔR of 1.9 orders magnitude was observed in the sample of 230ºC though rather lower R_{RT} was found compared to the 250 and 300ºC. A weak transition was realized in the sample prepared at T_S of 200ºC, in which small diffraction peaks in XRD from both monoclinic VO_2 and metastable VO_2 (B) phases were observed. In summary, 250ºC is the most suitable temperature for the VO_2 deposition on the Ti layer, in which 2.6 orders of magnitude change in resistance was obtained. The cause of deterioration of IMT at higher substrate temperature will be explained in XPS section. The summarizing results of out-of-plane *R-T* characteristics were listed in Table 2-3.

Table 2-3 IMT properties of VO_2 films on Ti/Si substrates deposited at different *T*s.

Sub. Temp. (ºC)	Heating		Cooling		T_{IMT-H} (ºC)	T_{IMT-C} (ºC)	ΔH (ºC)	ΔR
	R_{RT-H} (kΩ)	R_{100-H} (Ω)	R_{RT-C} (kΩ)	R_{100-C} (Ω)				
200	3.1	86	3.1	90	65	63	2	1.1
230	50.2	380	50.2	380	72	65	7	1.9
250	83.2	244	83.2	247	71	67	4	2.6
300	13.2	131	13.2	131	66	62	4	1.9
350	5.1	240	5.1	240	66	61	5	0.9
400	3.3	805	3.1	805	0	0	0	0

2.3.2-5 Reproducibility of *R-T* Characteristics in Point Contact Measurement Method

In this section reproducibility of *R-T* characteristics in present point contact measurements is discussed. The sample prepared at 250ºC was presented for this purpose. The *R-T* characteristics were measured in different places on different dates with the aim of investigating the reproducibility of *R-T* characteristics.

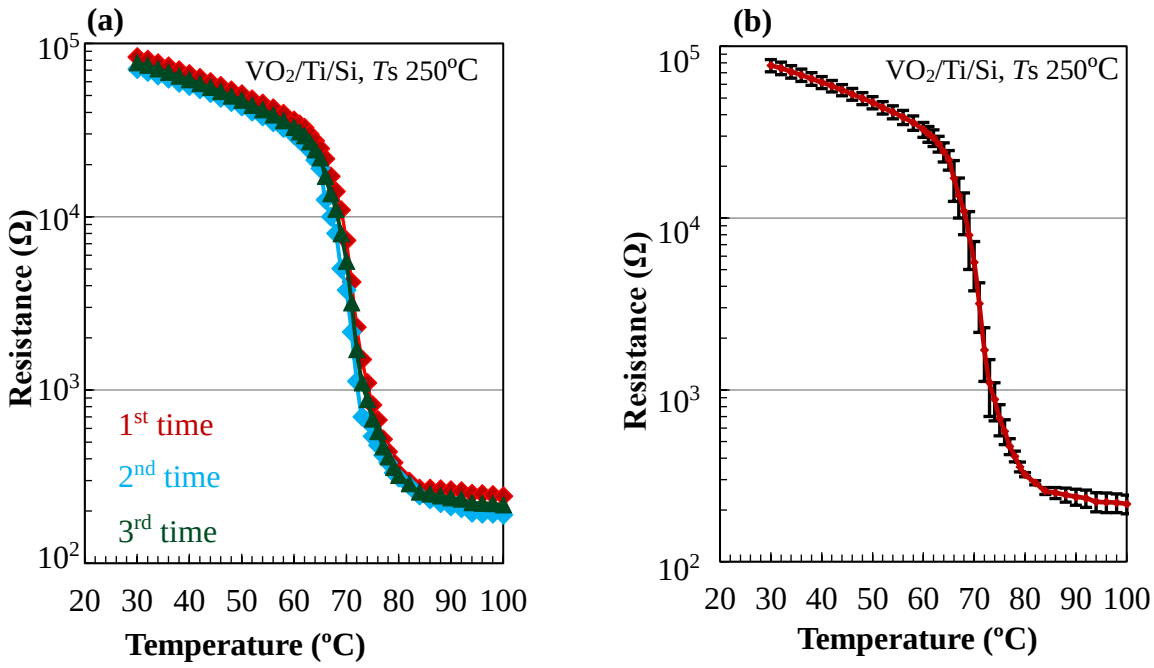

Fig. 2-10 (a) Reproducibility of *R-T* characteristics in point contact measurements for the sample prepared at 250ºC in different places and (b) *R-T* with error bars.

Figure 2-10 (a) shows the *R-T* characteristics measured in different places on different dates. The results are only for heating runs. The initial resistance was almost the same in every measurements. Reproducibility of the resistance change with temperature was shown in this figure, though slight variation depending on the place was present as shown by error bars in Fig. 2-10 (b).

2.3.2-6 Resistivity-Temperature (ρ-T) Characteristics and Mechanism of Large Out-of-Plane IMT in Layered Type Device

In section 2.3.2-4, the results were presented as resistance versus temperature, R-T characteristics. In this section the resistivity, ρ was calculated by the equation of $\rho = R\frac{S}{l}$, where R is resistance of the sample, s is cross-sectional area of the contact probe, and l is film thickness of the VO_2. The schematic of resistivity calculation is given in Fig. 2-11 (a).

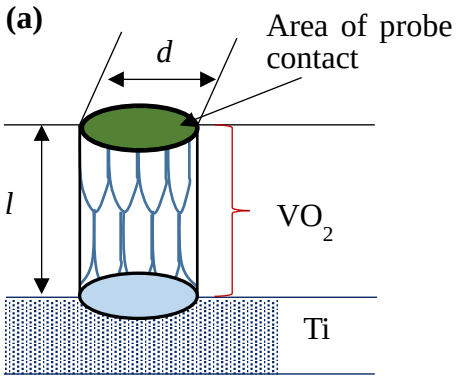

R=83 kΩ (VO_2/Ti/Si , Ts 250ºC)

l=200 nm $s=\frac{\pi d^2}{4}$ (d=50 μm)

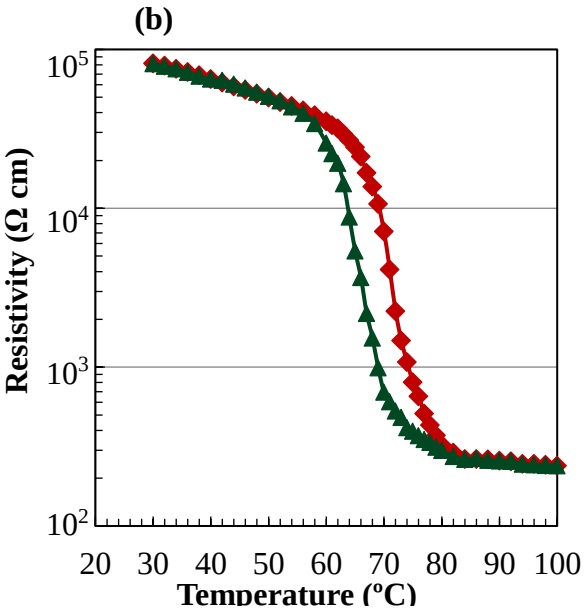

,

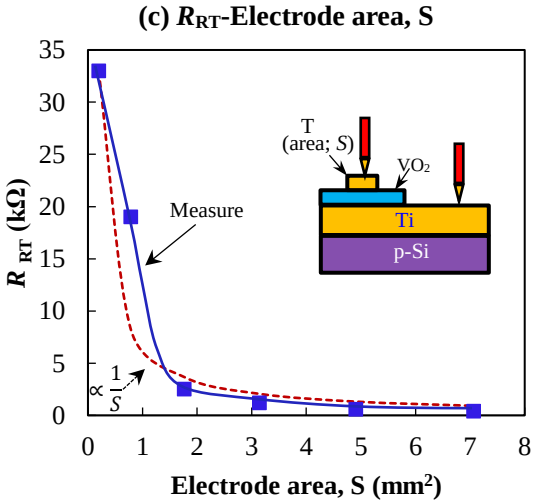

Fig. 2-11 (a) Schematic of resistivity calculation, (b) ρ-T characteristics for the sample prepared at 250ºC, and (c) Relationship between R_{RT} of the VO_2/Ti/Si structure and the electrode area, S, of Ti electrode. Fig. (c) is "Reproduced with permission from [Md. Suruz Mian and K. Okimura, J. Vac. Sci. Technol. A **32**, 041502 (2014)]. Copyright [2014], American Vacuum Society."

Fig. 2-11 (b) shows the ρ-T characteristics of the sample prepared at 250ºC. In monoclinic phase, ρ was calculated to be 8.13×10^4 Ω cm. This value is about three orders higher than the reported value of 10 Ω cm for the pure VO_2 thin film. [50] In the present proposed device, higher initial resistance was observed realizing a large resistance drops in the out-of-plane direction. However, other research groups could not succeed in realizing the out-of-plane IMT of VO_2 films grown on Pt layers, because of their low initial resistance[16,17]. So, it needs to clarify the causes of high initial resistance and the mechanism of out-of-plane IMT in this layered structure. To clarify the mechanisms of high out-of-plane initial resistance and realization of abrupt IMT in this layered structure device, Ti electrodes with different sizes of 0.5 ~ 7.0 mm^2 were fabricated on VO_2/Ti/Si structure (250°C) by a vacuum evaporation method. Figure 2-11 (c) shows the relationship between the R_{RT} and the electrode area, S. It can be seen that the R_{RT} was inversely proportional to S as illustrated by theoretical curve of $R_{RT} \propto \frac{1}{S}$. This results indicate that the current path increased as electrode area increased. Based on the polycrystalline feature, it was elucidated that the current path is formed within such crystalline grains covered by the upper electrode (probe) (Fig. 2-11(a)). Furthermore, the presence of grain boundaries in the presents polycrystalline VO_2 film is considered to be also responsible for such high initial resistance between the top and bottom electrodes. In contrast, the VO_2 film on the Pt layer is considered to be a laterally grown oriented crystals in which grain boundary contribution is suppressed and the current flows through entire the film; resulting in low initial resistance. Thus, the high R_{RT} in the present layered type device has potential advantages in realizing intrinsic IMT of VO_2 films on metal layers without additional VO_2 etching to enhance its resistance.

2.3.2-7 Arrhenius Plots (*σ-1/T*) Characteristics of the Sample Prepared at 250ºC

VO_2 shows insulator-like property at room temperature, and it turns to show metallic after SPT. Values of conductivity σ against 1/*T* in unit of K^{-1} were calculated for the sample prepared at 250ºC. Figure 2-12 shows the σ-1/T characteristics, Arrhenius plots for the heating case of the sample of 250ºC. When conductivity σ obeys activation process with temperature, σ is proportional to $e^{-\frac{\Delta Ea}{kT}}$, where Δ*E*a presents the activation energy, and *k* signifies the Boltzmann's constant. Then, Δ*E*a can be derived from straight-line fitting for the Arrhenius plots. The values of Δ*E*a were calculated for both the low-temperature insulator phase (IP) and the high-temperature metallic phase (MP) from the slopes of fitting lines, as presented in Fig. 2-12. The achieved values of Δ*E*a were 0.22 eV for IP and 0.09 eV for MP, respectively. The Δ*E*a of 0.22 eV in IP is as almost the same compared to reported value of VO_2 film.[34,51,52]

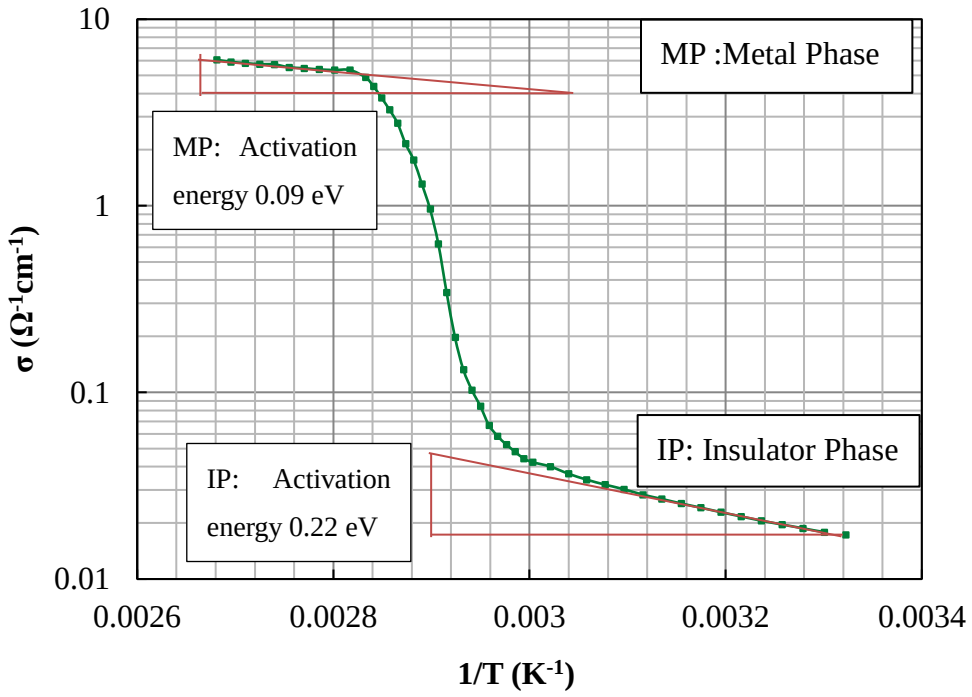

Fig. 2-12 Arrhenius plots of conductivity, σ, against 1/T for the sample deposited at 250ºC.

2.3.3 Comparison of Deposition Performance of Conventional Sputtering (CS) with ICPS

2.3.3-1 Deposition Conditions of VO_2 films in CS

In the previous section, a stoichiometric crystal growth of VO_2 films on Ti/Si substrates was realized at a substrate temperature of 250ºC by ICP-assisted sputtering method. In this section, crystalline growth of VO_2 films on Ti/Si substrates by the conventional rf-magnetron sputtering (CS) method was performed. The rf magnetron sputtering method is a general sputtering technique and reported to be able to deposit crystalline VO_2 films. Two samples were fabricated; one was at 250ºC and another one was at 400ºC. The other deposition conditions were same as the deposition conditions during the ICP-assisted sputtering. The deposition conditions in CS were given in Table 2-4.

Table 2-4 Deposition conditions of VO_2 films in CS.

Target	V (99.9%)
Substrate	Ti/Si
Substrate Temperature (°C)	250 and 400
Target –rf power (W)	200
ICP-rf power (W)	Non
Ar gas flow (sccm)	50
O_2 flow (sccm)	1.0
(Ar+O_2) Pressure (Pa)	0.5
Deposition Time (min)	20

2.3.3-2 XRD Patterns of VO_2 Films Deposited on Ti/Si Substrates by the CS

In this section, the crystal growth of VO_2 films on Ti/Si substrates by conventional sputtering (CS) method was investigated. Figure 2-13 shows the XRD 2θ scans for the deposited VO_2 films. XRD patterns for *T*s of 250 and 400ºC deposited by the ICP-assisted sputtering method were reused in this figure. In this section, 2θ scan with a low X-ray incident angle of 2° was carried out.

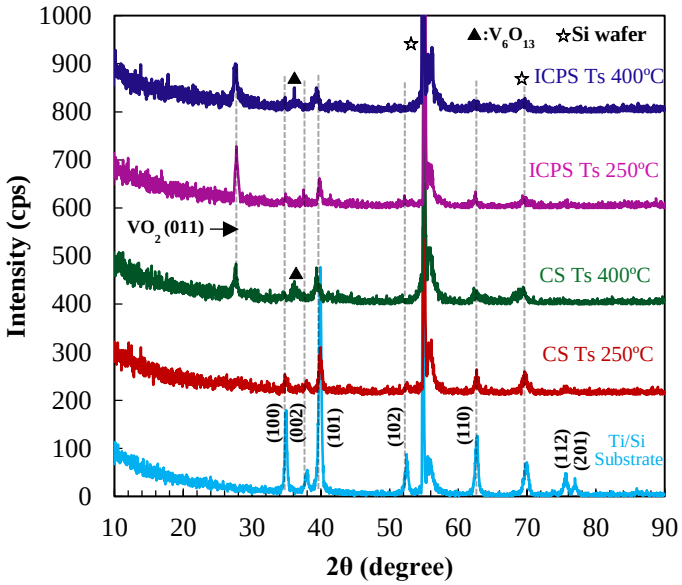

Fig. 2-13 XRD patterns of VO_2 films deposited at 250 and 400ºC. The results of ICP-assisted sputtering method is reused from Fig. 2-8.[62] "Copyright (2014) The Japan Society of Applied Physics"

Figure 2-13 shows the XRD patterns of VO_2 films deposited on Ti/Si substrates by the CS at 250 and 400ºC. In Fig. 2-13, no diffraction from VO_2 was observed for the sample prepared at 250ºC by the CS method. This result suggested the growth of amorphous VO_2 film on Ti/Si substrates at a low substrate temperature in CS methods. On the other hand, crystal growth with a weak peak from VO_2 (011) plane was observed at 2θ = 27.85° for the sample prepared at 400ºC in CS method. However, in the case of ICP-assisted sputtering method, strong diffraction from VO_2 (011) plane at 2θ = 27.85° was observed in both samples prepared at 250 and 400ºC as shown in Fig. 2-8.

2.3.3-3 *R-T* Characteristics of VO_2 Films Deposited on Ti/Si Substrates by the CS

In this section, out-of-plane *R-T* characteristics of VO_2 films deposited by the CS method were discussed. Figure 2-14 (a) presents the out-of-plane *R-T* characteristics for the fabricated samples. *R-T* characteristics of the films deposited at 250 and 400ºC for ICP-assisted sputtering method shown in Fig. 2-14 (b) were reused from Fig. 2-9 (a) and (b).

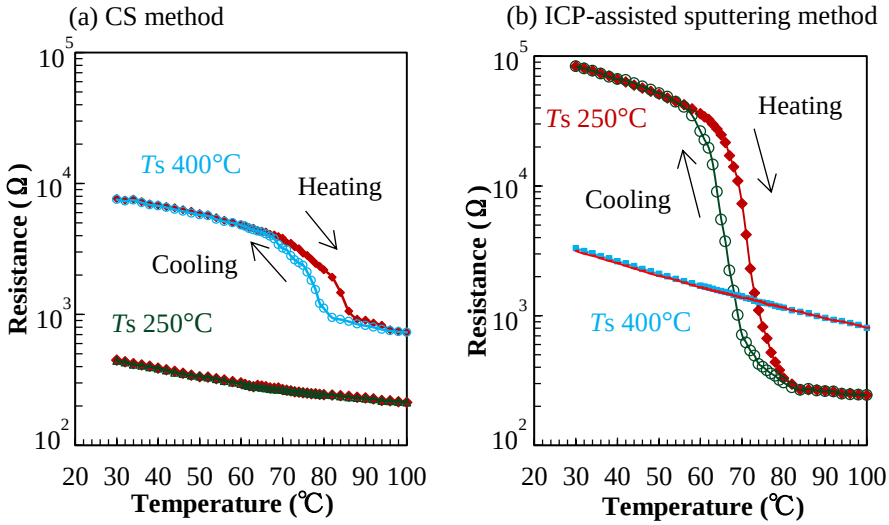

Fig. 2-14 Resistance-temperature (*R-T*) characteristics of VO_2 films prepared by (a) CS method and (b) ICP-assisted sputtering method at substrate temperatures of 250 and 400°C.[62]

In Fig 2-14 (a), no IMT was observed in the film prepared by the CS method at 250°C, while a sharp IMT with more than two orders of magnitude change was realized in the films deposited by ICP-assisted sputtering. In contrast, a weak transition with nearly one order of magnitude in resistance was observed in the sample of 400°C in the case of CS. These results were consistent with the XRD results. So, it is essential to clarify the reason behind the preferable crystalline growth of VO_2 film at a low substrate temperature of 250°C deposited by the ICP-assisted sputtering method. To elucidate this matter, the characterization of both deposition apparatus were investigated and given in next section.

2.3.4 Characterization of ICPS and CS

2.3.4-1 Experimental Procedure

In the previous section, the low-temperature crystalline growth of VO_2 films on Ti/Si substrates was achieved in the ICP-assisted sputtering method, while the crystallization of VO_2 film was not observed in CS sputtering method at the same low substrate temperature of 250°C. In this section, characterization of both deposition techniques was performed to clarify the low-temperature crystalline growth of VO_2.

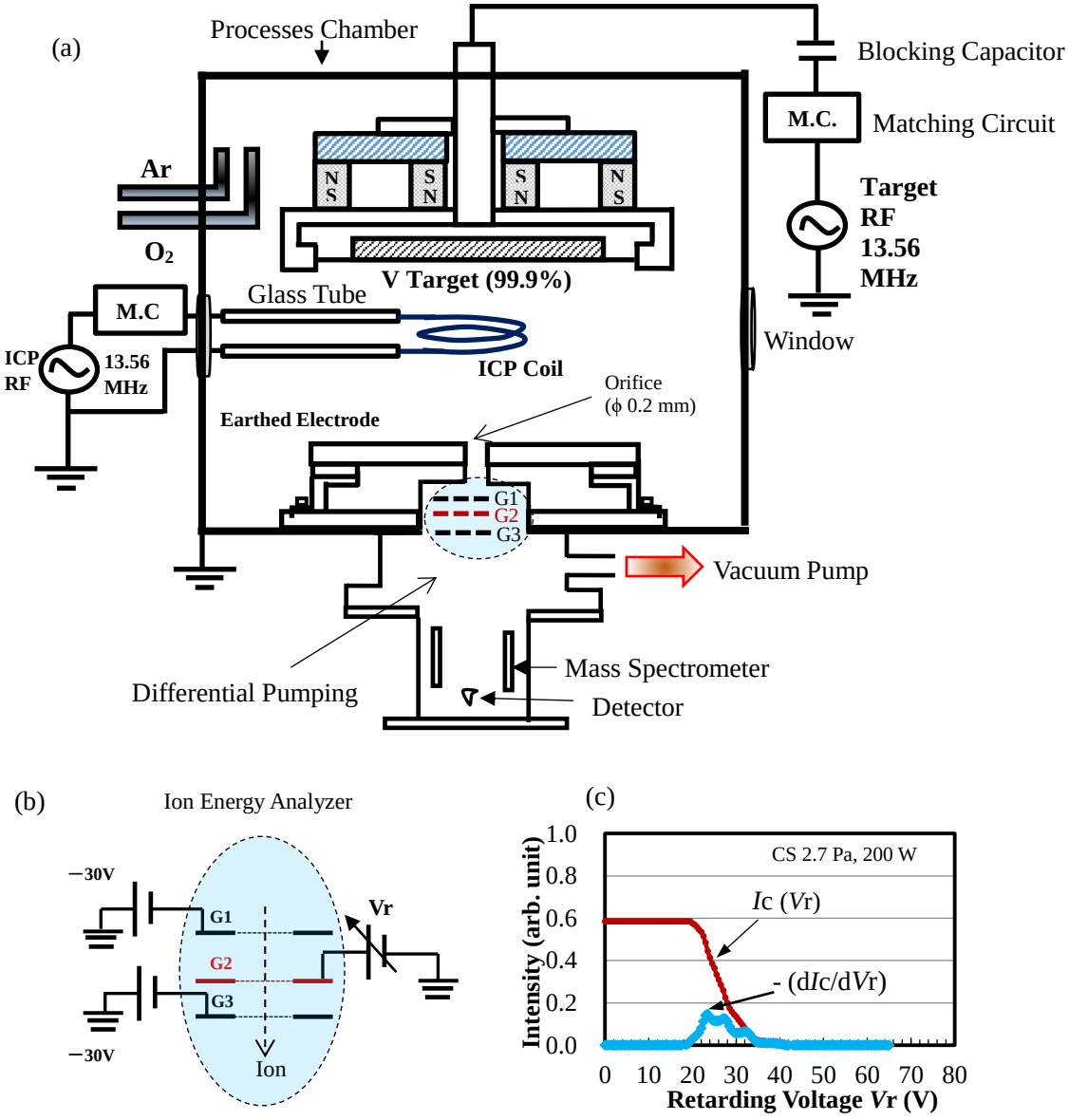

Fig. 2-15 (a) Schematic experimental setup for measurements of IEDs in the ICP-assisted sputtering apparatus, (b) ion energy analyzer consisting of three mesh grids, (c) an example of collected current, I_c, against retarding potential, V_r. The first derivative of I_c with respect to V_r, - (dI_c/dV_r) represents ion energy distribution.[62]

The ion energy distributions (IEDs) of Ar ions to the substrate in both sputtering methods were measured by means of an electrostatic energy analyzer coupled with quadrupole mass analyzer.

The dependence of IEDs on ICP-power was characterized. Values of plasma space potential (V_s), as one of the plasma parameter were measured by Langmuir probe method. Emission intensities from the plasma were measured by the optical emission spectroscopy. Figure 2-15 (a) shows the schematic of ICP-assisted sputtering apparatus with a mass spectrometer. A small orifice with the diameter of 0.2 mm was placed under the grounded electrode. This orifice enables ions and neutrals to pass through to the lower chamber, where a mass spectrometer was set. The particles reach the mass spectrometer without colliding with ambient gas molecules. The ionization filament was switched off in order to measure the Ar^+ ions. The IEDs were measured by using electrostatic energy analyzer, which is constructed in three grids as shown in Fig 2-15 (b). Each grid consisted of a 0.25 mm tungsten mesh (100 mesh/inch) with the area of the mesh was 100 mm^2. The retarding potential was applied to analyze the energy of incident ions. The retarding potential (V_r) was served at the second grid as shown in Fig 2-15 (b). The first and third grids were biased with a negative voltage of -30 V, for repelling electrons and focusing the ions towards the first grid and extracting the ions towards the detector at the third grid.

The current I_c against ion velocity, v, is given by following equation (1)

$$I_C = enA \int_{v_{min}}^{\infty} v f(v) dv \qquad \text{..... (1)}$$

where e is elementary charge, n is ion density, A is effective collector area, and $f(v)$ is velocity distribution function. The minimum velocity of incident ion, v_{min}, is given by V_r as follows.

$$\frac{1}{2} m {v_{min}}^2 = eV_r \qquad \text{..... (2)}$$

By translating velocity distribution function to energy distribution function $F(\varepsilon)$, the relation between I_c and $F(\varepsilon)$ is given as follows.

$$I_C = enA \int_{eV}^{\infty} \sqrt{\frac{2\varepsilon}{m}} F(\varepsilon) d\varepsilon \qquad \text{..... (3)}$$

By differentiating the collector current, I_c, with retarding voltage, V_r, we obtain following relation (4).

$$\frac{dI_c}{dV_r} = -e^2 nA \sqrt{\frac{2eV_r}{m}} F(eV_r) \qquad \text{..... (4)}$$

Thus, ion energy distribution (IED), $F(eV_r)$, is given as follows.

$$F(\mathrm{e}V_r) = -\frac{1}{e^2 nA} \sqrt{\frac{m}{2eV_r}} \frac{dI_c}{dV_r} \qquad \text{..... (5)}$$

Based on this relation, we obtained IED by measuring the collector current with respect to the retarding bias voltage, and numerically differentiating the I_c against V_r. Numerical differentiation was performed by four-points differentiation for smoothing data set. Figure 2-15 (c) shows change in Ic against Vr in the case of total pressure of 2.7 Pa and rf power of 200 W in the conventional sputtering. The ion energy is given by first derivative of I_c with respect to V_r, dI_c/dV_r, as also plotted in Fig. 2-15 (c).

2.3.4-2 Ion Energy Distributions (IEDs), Plasma Parameters, and Optical Emission

As described in the previous section, IEDs of Ar^+ ions subjected to the substrate in ICP-assisted sputtering and conventional sputtering were measured by an electrostatic energy analyzer coupled with quadrupole mass analyzer. Figure 2-16 shows the IEDs of Ar^+ ions for both CS and ICPS. During the measurement, pressure was constant at 0.5 Pa, which is the same as during the VO_2 film deposition. The horizontal axis represents the ion energy and the vertical axis means normalized intensity. The intensities of IEDs were normalized such that the integral value of the area of each IED converges to unity as a probability function.

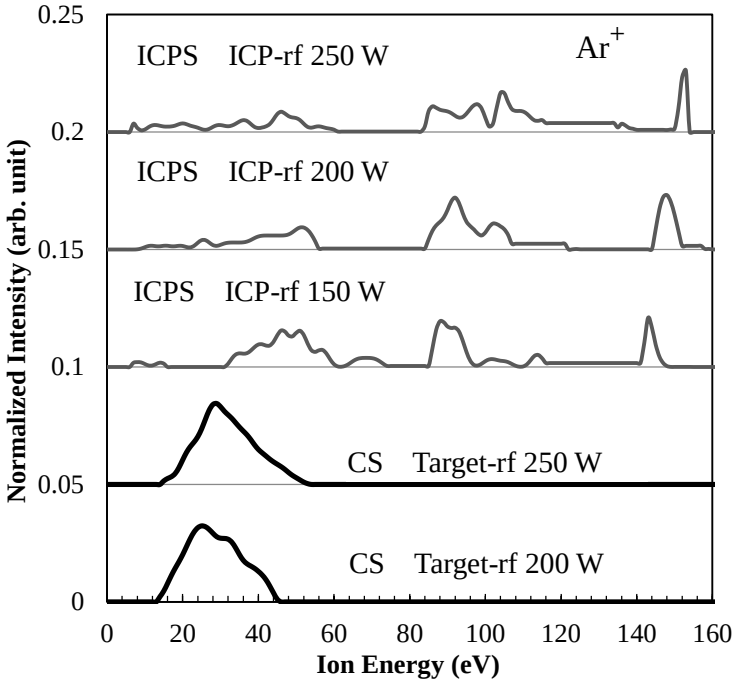

Fig. 2-16 IEDs of substrate-incident Ar^+ for both CS and ICPS. Intensities of IEDs against ion energy were normalized such that the integral value of the area of each IED converges to unity as a probability function.[62] "Copyright (2014) The Japan Society of Applied Physics"

In Fig. 2-16, it can be observed that the ion energies are ranging from 13 eV to 44 eV in the case of rf power at 200 W in CS. The highest peak intensity was observed at 26 eV. This peak was almost coincident with the plasma space potential that was measured using a single Langmuir probe consisting of a 2-mm long cylindrical tungsten (W) tip with the diameter of 0.3 mm. Langmuir probe was inserted at the center of the chamber with a distance from the surface of the ground electrode to be 15 mm. So, it can be considered that the IED is strongly dominated by the plasma potential at this

lower total pressure of 0.5 Pa in which mean free path of Ar^+ is estimated half of the distance between the target and the substrate. The lower energy component with energies less than 13 eV was considered to be present dispersion through various inelastic collisions. Such kind of lower energy could not be detected in the present set-up because of the lower sensitivity for the IED measurements. When the applied RF power was increased to 250 W in CS, the peak of IED shifted towards higher ion energy of 29 eV. In contrast, in the case of ICP-assisted sputtering apparatus with RF power of 150 W, three components of energy regions were observed at-40-50, 90-100, and 140-150 eV, respectively. In this case, the energy with the highest intensity was observed at about 142 eV. The IED tends to show higher shift with increasing ICP power. At ICP-rf power of 200 W, space potential was measured to be about 156 V, which is almost corresponding to that highest component in IED.

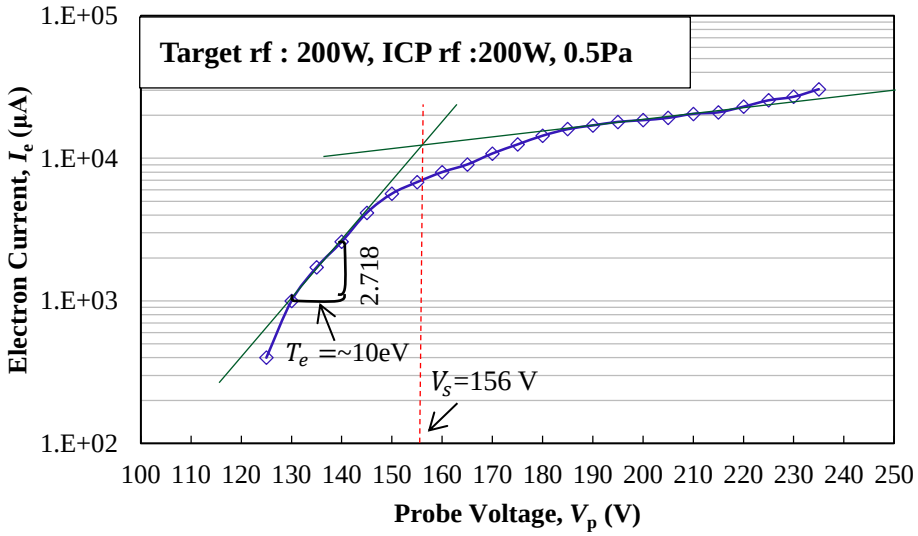

Fig. 2-17 Characteristics of electron current, I_e, against probe voltage, V_p, for ICP-rf and target-rf power of 200 W in the case of 0.5 Pa. Space potential, V_s = 156 V was given by the intersection of two straight lines.

Figure 2-17 shows the Langmuir probe characteristics which shows electron current flowing into the probe against the probe voltage for the ICP-rf and CS. The calculated space potential was designated on the figure and was observed to be about 156 V. It was reported that the IED is dominated by space potential oscillations with several tens V interval.[53,54] Thus it was clarified that the observed high energy components in IEDs in ICPS are responsible for quite high plasma space potential. It was also reported that the electrons run away from the metal coil, at a positively biased period resulting in a high electron temperature and high space potential in ICPS.[55,56] Explicitly, large losses of electrons result in high energy ions incident to the substrate by the acceleration potential between the substrate and the plasma. The obtained plasma density of ICPS at ICP-rf power of 200 W is estimated to be on

the order of 10^{10} cm^{-3}, which is not so high compared to CS. However, high space potential (V_s) together with high electron temperature (T_c) are characteristic in ICPS. Here, mean energy (E_{mean}) was provided by statistical calculation using IED. E_{mean} of ICPS at ICP-rf power of 150 W was 47 eV, and increased to 54 eV when ICP-rf power increased to 200 W. These values are quite higher than those in CS. Further, optical emission intensities for O* (777 nm) atom during the deposition was measured using S2000 fiber optic spectroscopy. Figure 2-18 presents the optical emission intensity for the O* (777 nm) atoms for the (a) ICPS and (b) CS. In Fig. 2-18 (a), the emission intensity was significantly increased with increasing ICP-rf power. In contrast, no change in emission intensity was observed for CS shown in Fig. 2-18 (b).

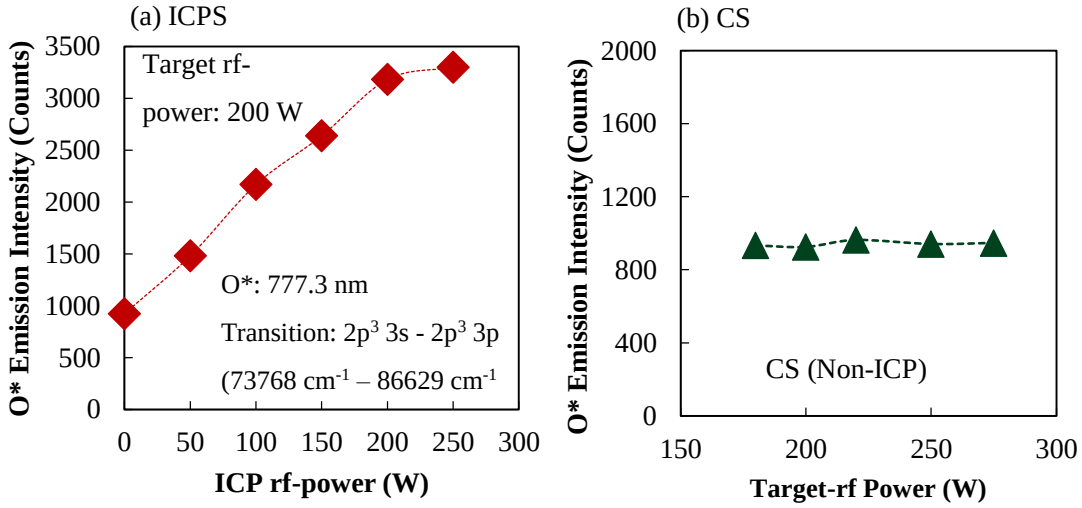

Fig. 2-18 Optical emission intensities for O* (777 nm) atoms for (a) ICPS and (b) CS.

Thus, it can be concluded that ICPS has a great advantage to generate high energy ions ranging from several tens eV to over 100 eV. Such high energy ions strongly assist low-temperature crystalline growth in oxide deposition. The summarization of IED's was listed in Table 2-5.

Table 2-5 Mean energy of IED, E_{mean}, energy at peak, E_{peak}, plasma space potential, V_s, electron temperature, T_e, and electron density, N_e. E_{mean} and E_{peak} were obtained from the measured IED's. V_s, T_e, and N_e were measured by Langmuir probe measurements. [62]"Copyright (2014) The Japan Society of Applied Physics"

Method	Target-rf (W)	ICP-rf (W)	E_{mean} (eV)	E_{peak} (eV)	V_s (V)	T_c (eV)	N_e (cm^{-3})
CS	200	non	17	26	25	4.4	1.7×10^{10}
CS	250	non	19	29	30	5.1	1.7×10^{10}
ICPS	200	150	47	142	150	-	-
ICPS	200	200	54	147	156	10	7.8×10^{10}

2.3.5 Characterization of the Samples Prepared by ICPS at Different Substrate Temperatures (*Ts*)

2.3.5-1 FE-SEM Images for the Samples Prepared at *Ts* from 250 to 400ºC

In this section, crystalline morphology was investigated evolution by FE-SEM images for the samples. Figures 2-19 (a) – (d) present the SEM images of films surface for samples prepared at 250 to 400ºC. In Fig. 2-19 (a), crystalline grains with diameters from 100 to 200 nm were observed for the sample deposited at 250ºC. Furthermore, grain boundaries are noticeably surrounding the crystalline grains. Such grain boundaries affect the out-of-plane IMT. The current path for the out-of-plane direction was restricted by isolated grains and expected to have a potential in achieving out-of-plane IMT with large resistance change. Oxygen vacancies at grain boundaries are responsible for nucleating the phase transition, resulting in early onset of IMT.[27,57]

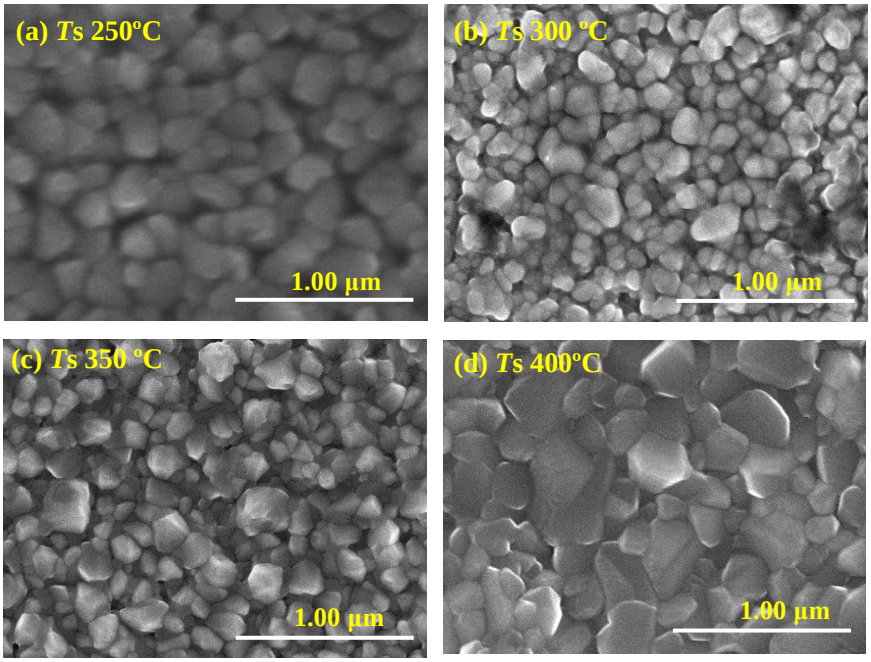

Fig. 2-19 Surface SEM images for the samples prepared at (a) 250ºC, (b) 300ºC, (c) 350ºC, and (d) 400ºC, respectively.

In contrast, densely filled larger crystalline grains with sizes from 100 nm to 300 nm were obtained for the sample prepared at 400ºC as shown in Fig. 2-19 (d), indicating significant effects of substrate temperature on the growth of VO_2 film.

2.3.5-2 Cross-sectional SEM Images for the Samples Prepared at *Ts* from 250 to 400ºC

Observation of the cross-sectional SEM is important for confirming the layered structure aspect, which is also important to characterize the interfacial states of the device. SEM images were taken for all samples prepared from 250 to 400ºC. The cross-sectional SEM images were shown in Fig. 2-20 for films of (a) 250ºC, (b) 300ºC, (c) 350ºC, and (d) 400ºC, respectively. In Fig. 2-20 (a) and (b), two layers L1 (VO_2 film) and L2 (Ti film) on Si substrates are clearly appeared without any interfacial mixing aspect.

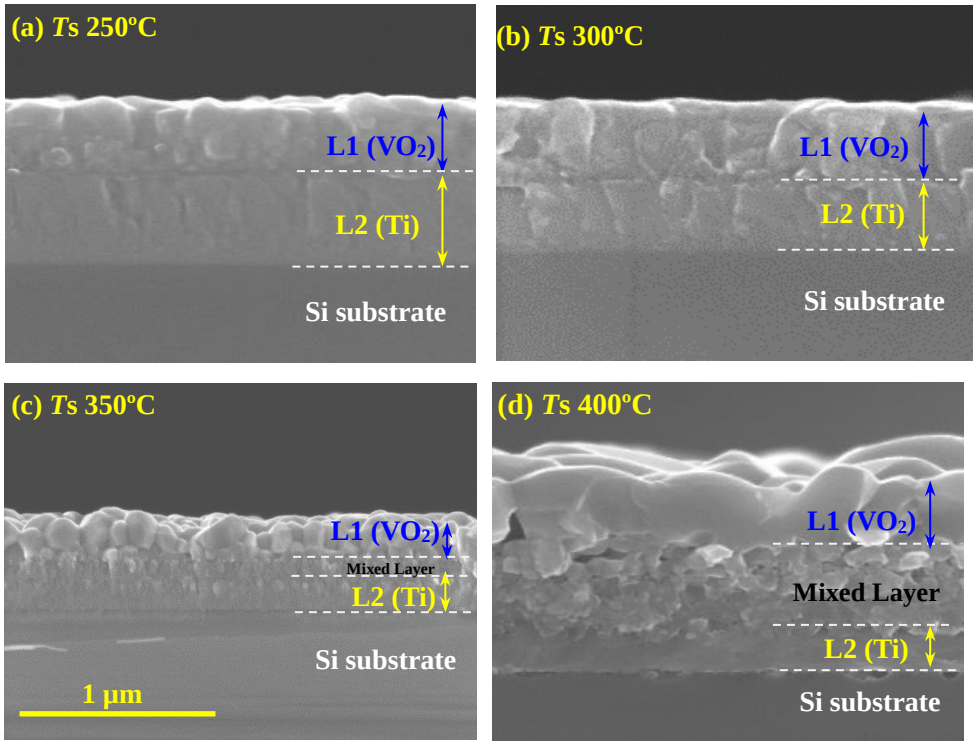

Fig. 2-20 Cross-sectional SEM images for the samples prepared at (a) 250ºC, (b) 300ºC, (c) 350ºC, and (d) 400ºC, respectively.

However, mixed layer started to be observed in Fig. 2-20 (c) for the film deposited at 350°C, while maintaining the three layers structure. Such a mixed layer in the vicinity of the interface is considered due to the diffusion of Ti atoms. This mixed layer became thicker with the increasing of substrate temperature, and a clear mixed layer between the VO_2 film and the Ti layer was observed in the sample of 400°C in Fig.2-20 (d), and the sandwich structures were no longer recognized in contrast to that at 250°C. Diffusion of Ti atoms into the interface might be responsible for the low R_{RT} and disappearance of out-of-plane *R-T* in the 400°C sample as presented in Fig. 2-20 (a). Further discussion will be given in the XPS measurement section.

2.3.5-3 XPS Depth Profiles for the Samples Prepared at *Ts* from 250 to 400°C

XPS depth measurements were performed for the samples prepared from 250 to 400ºC for discussing the chemical composition and interfacial condition for present layered structure device. Figure 2-21 shows the XPS depth profiles for the samples fabricated at (a) 250ºC, (b) 300ºC, (c) 350ºC, and (d) 400ºC, respectively. XPS spectra were taken for C 1*s*, O1*s*, Si 2*p*, V2*p*, and Ti 2*p* after every 2-min sputtering by Ar ion with an acceleration energy of 2 kV. The diameter of X-ray beam is 50 μm and the detector is located at 45º with respect to the surface of the sample.

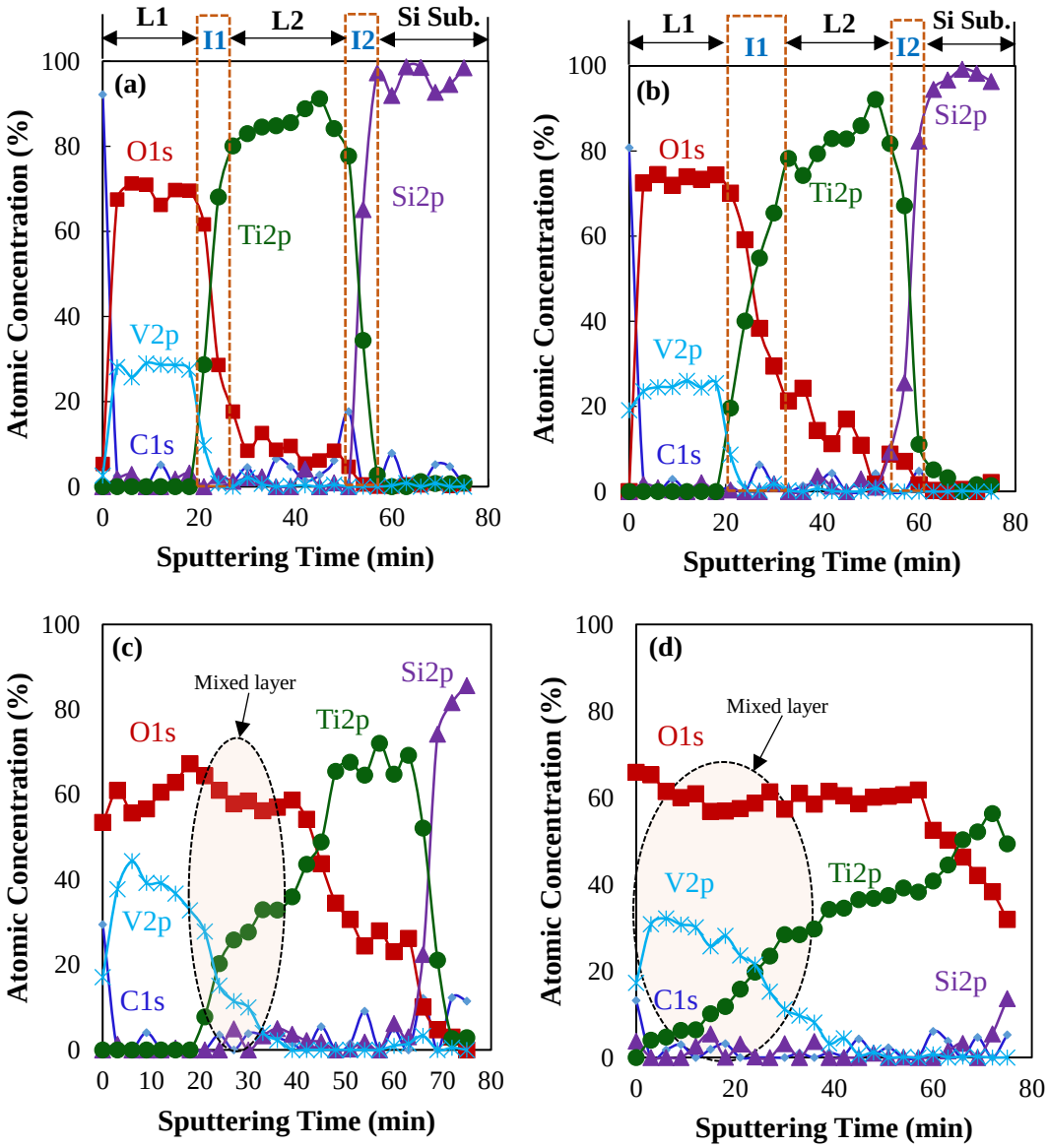

Fig. 2-21 XPS depth profiles for the samples prepared at (a) 250ºC, (b) 300ºC, (c) 350ºC, and (d) 400ºC, respectively.

In Fig. 2-21, the horizontal axis represents the total Ar-ion sputtering time and the vertical axis refers to the atomic concentrations. Atomic concentrations were derived from the area of each atomic spectrum. In Fig. 2-21 (a), two layers labeled as L1 (VO_2), L2 (Ti) with sharp interfaces were observed on the sample of 250ºC, which corresponds to the aspect as was observed in the cross-sectional SEM images (Fig. 2-20 (a)). The VO_2 film was almost stoichiometric in this sample. V and O disappeared in the interface region labeled "I1" as Ti are visible and later vanished near the interface between Ti and Si labeled as "I2". A clear interface without any interface diffusion was obtained between the VO_2 film and the Ti layer in this temperature of 250°C. Consequently, in this VO_2/Ti/Si prepared at 250°C, the Ti layer acts as a metal electrode. As the diffusion did not occur at the interface, sharp IMT was realized in the out-of-plane direction. As the film thickness of VO_2 film was 200 nm, as presented in Fig. 2-21 (a), the etching rate by Ar-ion was estimated as 9.8 nm/min until the interface shown in Fig. 2-21 (a). In Fig. 2-21 (b), wider interface (labeled I1) between the VO_2 film and the Ti film was observed than the sample of 250°C (Fig.2-21 (a)) with a little oxidized Ti layer in the interface. A mixed layer with V, Ti, and O was observed for the sample of 350°C as presented in Fig. 2-21 (c), where oxidation of Ti layer was also observed in this sample, which responsible for the deterioration of IMT at 350°C as shown in Fig. 2-9 (a). Furthermore, in Fig. 2-21 (d) for the sample deposited at 400°C, the top layer mixed with Ti up to the surface. Additionally, oxidation of Ti layer was also seen at this temperature. The disappearance of IMT in Fig. 2-9 (a) of 400°C was responsible for such a mixed layer formation. Therefore, it is recognized that elevated temperature of 400°C invites a crucial problem in the interface.[58]

2.3.5-4 Current-Voltage (*I-V*) Characteristics of the Samples Prepared at *Ts* from 230 to 300ºC

In this section, *I-V* characteristics were measured for the samples prepared at T_s from 230 to 300ºC, in which a good crystallinity was observed. The *I-V* characteristics were measured by KEITHLEY 6487 Picoammeter/Voltage Source. Figure 2-22 (a) shows the *I-V* characteristics of the samples prepared at T_s from 230 to 300ºC. Horizontal axis presents the switching voltage, V_{th} and vertical axis presents the switching current, I_{th}.

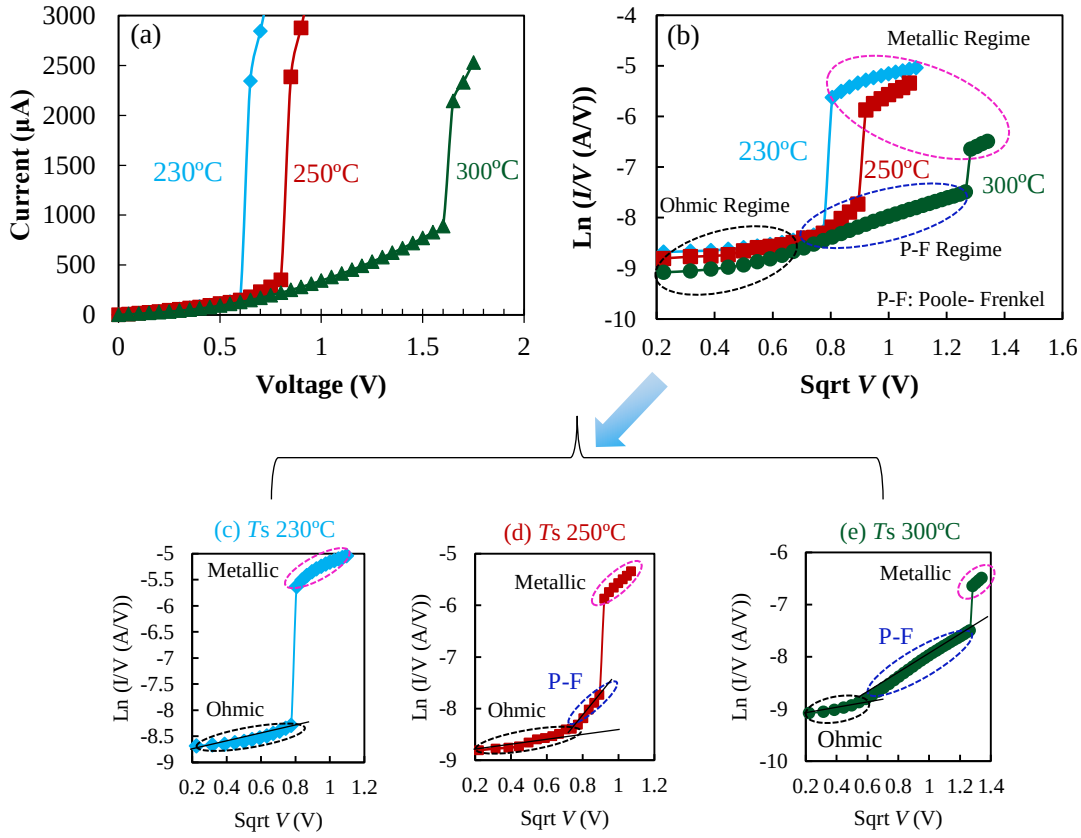

Fig. 2-22 (a) *I-V* characteristics of the samples prepared from 230 to 300ºC, (b) ln (*I/V*) vs. $\sqrt{V}$ measured from (a), and (c) – (e) present the each graph for the all samples taken from (b).

In Fig. 2-22 (a), switching was observed at voltage of 0.6 V with a current value of 150 μA for the sample prepared at *T*s of 230ºC. This V_{th} value is much lower than the reported value for the two-terminal planar type configuration, which was 2 V. These results suggested that the bottom electrode worked as a concrete electrode without interfacial oxidation. In this case, the calculated electric field, E_{th} was 3.0×10^6 V/m. This electric field was in the same order to those previously reported for the

VO_2 nanocontact[59] and nanogap[11], but one order of magnitude larger than the VO_2 planar type configuration.[2] The switching power consumption, *P* was estimated to be about 90 μW, which is lower than previously reported value in the planar type device. On the other hand, as for the samples deposited at *T*s of 250ºC and 300ºC, values of V_{th} were measured to be 0.8 V and 1.6 V, respectively. V_{th} and I_{th} increased with the increase of *T*s. This should be due to the existence of the interfacial oxidation between the VO_2 film and the Ti layer, as was shown in the XPS results. To investigate the *I-V* mechanism, ln (*I/V*) and $\sqrt{V}$ was calculated from the Fig. 2-22 (a) and was shown in Fig. 2-22 (b). Figure 2-22 (c) – (e) present the single graph for films deposited at all *T*s. In Fig. 2-22 (c), in the insulating state (region of before switching), the current was increased with an Ohmic manner. In contrast, two regimes contributing to Ohmic and Poole-Frenkel (P-F) were observed in Fig. 2-22 (d) and (e) in the insulating state, right before the switching occurred. The reason of the co-existence of these two regimes of different conductivities in the insulating state might be due to the contribution of the nonstoichiometric defects of the oxygen vacancy type.[60,61] *I-V* properties were summarized in Table 2-6.

Table 2-6 *I-V* properties of the samples prepared at *T*s from 230 to 300ºC.

***T*s**	V_{th}	I_{th}	***P***	E_{th}
(ºC)	(V)	(μA)	(W)	(V/m)
230	0.6	150	9.0×10^{-5}	3.0×10^{6}
250	0.8	350	2.8×10^{-4}	4.0×10^{6}
300	1.6	880	1.4×10^{-3}	8.0×10^{6}

2.3.6 Growth of VO_2 Films on Ti/Si Substrates with Different Film Thicknesses by the ICPS

In layered type device, film thickness of VO_2 film plays an important role for the control of the out-of-plane characteristics, since VO_2 film thickness corresponds to the electrode gap in the layered type device. Thus in this section, the dependence of VO_2 film thicknesses was investigated. As already described in section 2.3.2-3 and 2.3.2-4, good crystallinity with a sharp out-of-plane IMT was achieved at *T*s of 250ºC. Based on these results, VO_2 films with different film thicknesses were prepared by the ICP-assisted sputtering method at 250ºC. Other deposition conditions are as same as described in section 2.3.2-1. In this case, with the aim to prepare samples with different film thicknesses, deposition times were varied from 20 to 80 min. The film thicknesses were later determined by the cross-section SEM images as shown in Fig. 2-23.

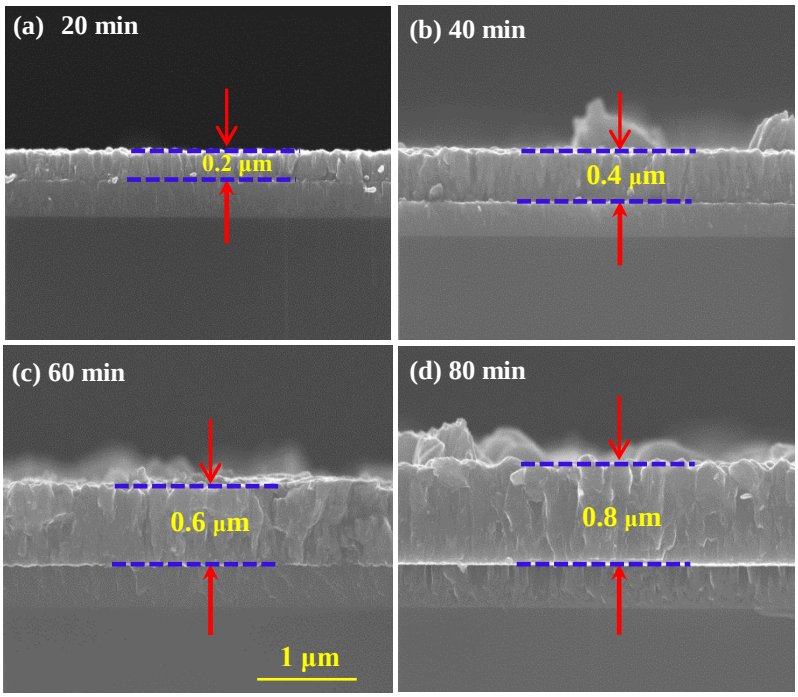

Fig. 2-23 Cross-sectional SEM images of VO_2 films deposited for (a) 20 min, (b) 40 min, (c) 60 min, and (d) 80 min, respectively.

In Fig. 2-23, The film thicknesses were observed to be about 200 nm for the sample prepared at 20 min, 400 nm for 40 min, 600 nm for 60 min, and 800 nm for 80 min.

(a) XRD Patterns of the Samples Prepared with Different Film Thicknesses

Figure 2-24 shows the XRD 2θ scan patterns for the samples with different film thicknesses. Diffractions from hcp-Ti (002), (101), (102), (110), (200), and (112) planes were detected at 2θ = 38.05°, 39.95°, 52.29°, 62.86°, 74.85°, and 77.25°, respectively.

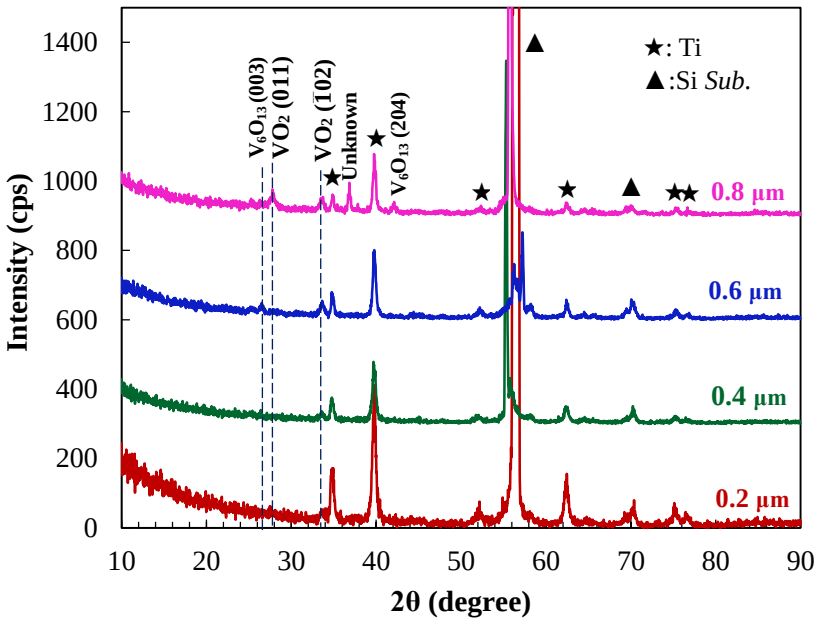

Fig. 2-24 XRD patterns of the samples prepared with different film thicknesses.

Diffractions from VO_2 (011) and ($\bar{1}02$) planes were observed at 2θ = 27.8° and 33.3°,where the peaks intensity increased with the increase of the film thicknesses. These results suggested the polycrystalline growth of VO_2 films (as was previously described in *T*s dependence). A new peak from V_6O_{13} (003) plane was appeared at 2θ = 26.8° for the films from 0.4 to 0.8 μm. Furthermore, another new peak from V_6O_{13} (204) plane was observed at 2θ = 42.2° for the film of 0.8 μm. According to these results, it could be expected that the substrate temperature increased with the increase of deposition time, stabilizing the growth of high oxidation state, V_6O_{13}.

(b) *R-T* Characteristics of the Samples Prepared with Different Film Thicknesses

Figure 2-25 presents the out-of-plane *R-T* characteristics of the samples with different film thicknesses. In Fig. 2-25, 1.3 order of magnitude change in resistance was observed in the sample of 0.2 μm, with $T_{IMT\text{-}H}$ at about 72°C and $T_{IMT\text{-}C}$ at 67°C, and ΔH of 5°C. In the samples of 0.4 and 0.6 μm, IMT with near two orders of magnitude change in resistance were obtained. The $T_{IMT\text{-}H}$ was observed to be at 67°C and $T_{IMT\text{-}C}$ was at 63°C for 0.4 μm. This T_{IMT} of 67°C was rather lower than the sample of 0.2 μm. However, The $T_{IMT\text{-}H}$ was observed at 74°C, which is higher than that of the 0.2 μm. On the other hand, ΔR became smaller in the case of 0.8 μm, and the T_{IMT} shifted to the lower temperature. In this case, $T_{IMT\text{-}H}$ was observed at 60°C, and $T_{IMT\text{-}C}$ at 58°C than the others sample. The shift of the T_{IMT} to lower temperature might be due to the compressive stress in the sample. One can observe, that initial resistance, R_{RT} increased with the increase of the film thickness until 0.6 μm, then decreased at 0.8 μm. The presence of V_6O_{13}, which is reported to be metallic like at room temperature, might be responsible for the decrease of the R_{RT} in 0.8 μm as shown in shown in Fig. 2-25.

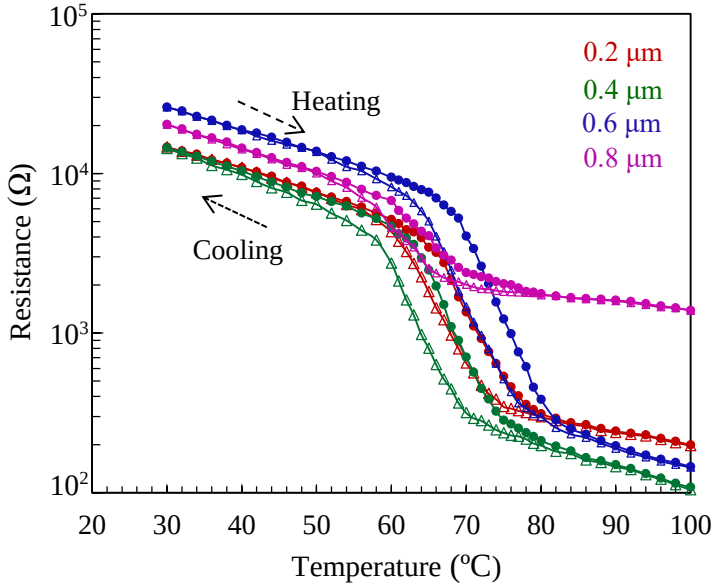

Fig. 2-25 *R-T* characteristics of the samples prepared with different film thicknesses.

(c) *I-V* Characteristics of the Samples Prepared with Different Film Thicknesses

Figure 2-26 (a) shows the *I-V* characteristics of the samples prepared at different film thicknesses. In the sample of 200 nm, switching was observed at the applied voltage of 0.45 V with a switching current of 222 μA. The switching voltage, V_{th}, and current, I_{th}, gradually increased with increasing film thickness. The switching voltage of 0.45 V is the lowest switching voltage in VO_2-based devices, including bulk, two-terminal planar type devices, and layered type device. Figure 2-26 (b) shows the ln (*I/V*) *vs.* $\sqrt{V}$ characteristics for all samples. The data were taken from Fig. 2-26 (a). In Fig. 2-26 (b), two regimes were observed in the insulating state. Ohmic regime was observed in a relatively low voltage area, and P-F regime was observed just before the switching occurred. V_{th} and I_{th} against the film thickness was illustrated in Fig. 2-26 (c).

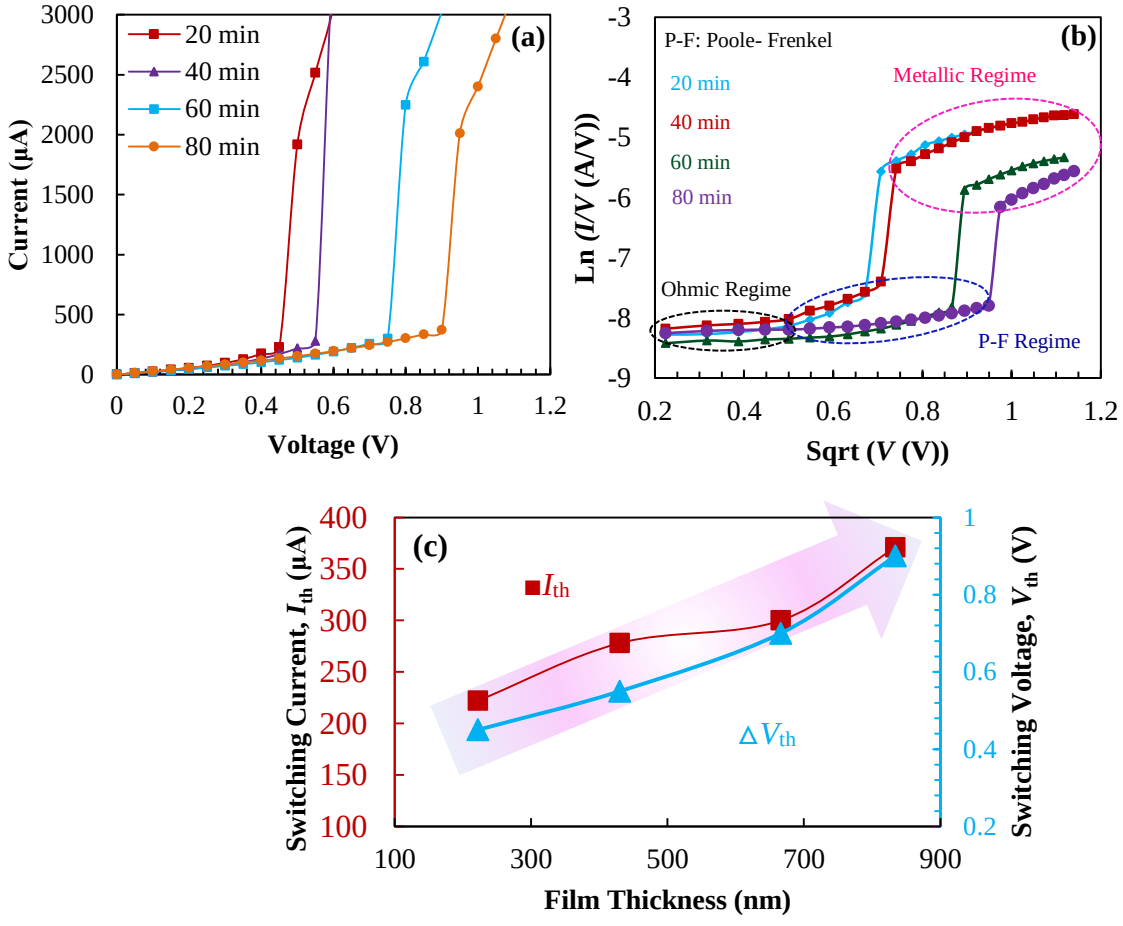

Fig. 2-26 (a) *I-V* characteristics of the samples prepared with different film thicknesses, (b) P-F plots [ln (*I/V*) vs. $\sqrt{V}$] constructed from *I-V* curves shown in (a), and (c) values of V_{th} and I_{th} against film thicknesses.

(d) Switching Electric Field and Power Consumption of the Samples Prepared with Different Film Thicknesses.

Figure 2-27 shows the switching electric field, E_{th} and the power consumption of samples prepared with different film thicknesses. E_{th} increased with decreasing film thicknesses according to the equation of $E_{th} = V_{th}/L$, in which V_{th} is switching voltage, and L is film thickness. The present E_{th} is in the same order as was previously reported in nanogap,[59] nanocontact,[11] and layered type device.[17] However, this value is one order higher than the planar type configuration.[2] Sakai *et al.* surveyed a relationship between transition voltage and film thickness in various type of devices, including VO_2 single crystal, VO_2-based two-terminal planar type devices and VO_2-based layered type device. They reported that E_{th} was disproportional to L, but rather proportional to $L^{1/2}$.[17]

On the other hand, power consumption, P ($P = VI$) decreased with decreasing film thicknesses. The lowest P of 9×10^{-5} W was obtained in the sample with film thickness of 200 nm. The present P is of about two orders lower than previously reported in VO_2-based two-terminal planar type devices and as well as layered type devices.[2–4,6,17] These results suggested that P might be further decreased with the decreasing film thicknesses to several tens nm, indicating the potential of this layered type device.

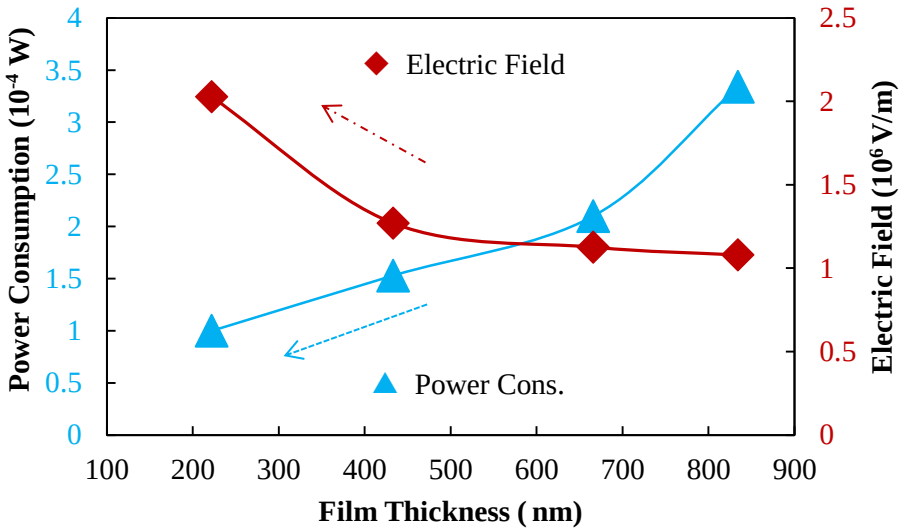

Fig. 2-27 Switching electric field and power consumption of the samples prepared with different film thicknesses.

2.4 Conclusions

In this chapter, VO_2 films were deposited on Ti/Si substrates by using inductively coupled plasma-assisted sputtering (ICPS) method. First, Ti films with a thickness of 300 nm were deposited on p-Si (100) substrates by ICPS method. The resistivities of the Ti films was evaluated to be $1 – 2 \times 10^{-4}$ Ωcm. In the deposition of VO_2 films on the Ti/Si substrates, deposition temperatures were varied from 150 to 450°C for fixed deposition conditions. As the results, diffraction from VO_2 (011) plane was observed on samples prepared at 200 - 400°C, indicating that the VO_2 film grown on Ti/Si has polycrystalline manner. The highest peak intensity was observed at 250°C, while the peak intensity decreased gradually with increasing temperature. In the resistance –temperature (*R-T*) characteristics, the largest out-of-plane IMT with resistance change of 2.6 orders was realized in the sample prepared at 250°C. The disappearance of IMT in the sample prepared at 400°C suggested that low-temperature deposition is required for achievement of large IMT of VO_2 film on the metal template.

In XPS results, a sharp interface between the VO_2 film and the Ti layer was clearly observed in the sample prepared at the substrate temperature of 250°C, while formation of mixing layer with V, O and Ti was found in the samples prepared at temperatures higher than 350°C. Thus, it is vitally important to produce a sharp interface between VO_2 and the bottom electrode in order to achieve a superior IMT properties in the out-of-plane direction. In the sample of 250°C, Ti films acted as an electrode, and a sharp out-of-plane IMT was accomplished. On the other hand, the diffusion of O atoms and the oxidation of Ti films were occurred in the sample fabricated at the higher substrate temperature of 400°C, and were responsible for the degradation of the out-of-plane IMT. Accordingly, it became clear that the 250°C is the suitable substrate temperature for the crystal growth of VO_2 films on the Ti/Si substrates.

The obtained large out-of-plane IMT in VO_2 on Ti/Si substrates is responsible for high resistance value at room temperature. In the present study, presence of grain boundaries in the polycrystalline VO_2 film is considered to be responsible for such high initial resistance between top electrode and bottom electrode. Low-temperature deposition of VO_2 films on metal templates by the ICPS method enabled such large out-of-plane IMT avoiding the diffusion and oxidation of Ti layer .

In order to clarify the advantage of the ICPS method compared to conventional sputtering (CS), comparisons of deposition performances and plasma diagnostics were done between ICPS and CS. As the results, crystalline VO_2 films could not be obtained by the CS at temperature lower than 250°C in contrast to ICPS. Diagnostics results of ion energy distributions (IEDs) for substrate-incident ions showed that the presence of high energy ion components with energies around 80 and 150 eV enhance the low-temperature crystalline growth. In addition, enhancement of oxygen radical (O*) production is also considered to be responsible for the growth of stoichiometric VO_2 films at the low temperature.

In *I-V* characteristics, the threshold switching was observed at the applied voltage of 0.6 V with a current value of 150 μA (power consumption: 90 μW) for the sample of 230°C. This V_{th} value is much

lower than the reported value for the two-terminal planar type configuration, which was several volt. Threshold switching was observed at 0.8 V and 1.6 V for the samples of 250 and 300°C, respectively. The results that the V_{th} and I_{th} increased with Ts should be due to the interfacial mixing layer. The achieved low voltage and power consumption have great potential for the application as a low voltage selective switch for the non-volatile memory.

References

[1] F. J. Morin, Phys. Rev. Lett. **3**, 34 (1959).

[2] J. Sakai and M. Kurisu, Phys. Rev. B - Condens. Matter Mater. Phys. **78**, 2 (2008).

[3] K. Okimura, N. Ezreena, Y. Sasakawa, and J. Sakai, Jpn. J. Appl. Phys. **48**, 065003 (2009).

[4] H.-T. Kim, B.-G. Chae, D.-H. Youn, G. Kim, K.-Y. Kang, S.-J. Lee, K. Kim, and Y.-S. Lim, Appl. Phys. Lett. **86**, 242101 (2005).

[5] C. N. Berglund, IEEE Trans. Electron Devices **16**, 432 (1969).

[6] G. Stefanovich, A. Pergament, and D. Stefanovich, J. Phys. Condens. Matter **12**, 8837 (2000).

[7] H.-T. Kim, B.-G. Chae, D.-H. Youn, S.-L. Maeng, G. Kim, K.-Y. Kang, and Y.-S. Lim, New J. Phys. **6**, 52 (2004).

[8] C.-R. Cho, S. Cho, S. Vadim, R. Jung, and I. Yoo, Thin Solid Films **495**, 375 (2006).

[9] J. S. Lee, M. Ortolani, A. Ginolas, Y. J. Chang, T. W. Noh, and U. Schade, Phys. C **460-462**, 549 (2007).

[10] C. Ko and S. Ramanathan, Appl. Phys. Lett. **93**, 8 (2008).

[11] D. Ruzmetov, G. Gopalakrishnan, J. Deng, V. Narayanamurti, and S. Ramanathan, J. Appl. Phys. **106**, 083702 (2009).

[12] Z. Yang, C. Ko, and S. Ramanathan, J. Appl. Phys. **108**, 073708 (2010).

[13] Z. Yang, S. Hart, C. Ko, A. Yacoby, and S. Ramanathan, J. Appl. Phys. **110**, 033725 (2011).

[14] Y. Cui, X. Wang, Y. Zhou, R. Gordon, and S. Ramanathan, J. Cryst. Growth **338**, 96 (2012).

[15] M. Son, J. Lee, J. Park, J. Shin, G. Choi, S. Jung, W. Lee, S. Kim, S. Park, and H. Hwang, IEEE Electron Device Lett. **32**, 1579 (2011).

[16] Jakub A. Koza, Z. He, A. S. Miller, and J. A. Switzer, Chem. Mater. **23**, 4106 (2011).

[17] J. Sakai, M. Zaghrioui, V. Ta Phuoc, S. Roger, C. Autret-Lambert, and K. Okimura, J. Appl. Phys. **113**, 123503 (2013).

[18] D. H. Kim and H. S. Kwok, Appl. Phys. Lett. **65**, 3188 (1994).

[19] Y. Shigesato, M. Enomoto, and H. Odaka, Jpn. J. Appl. Phys. **39**, 6016 (2000).

[20] P. Jin, K. Yoshimura, and S. Tanemura, J. Vac. Sci. Technol. A Vacuum, Surfaces, Film. **15**, 1113 (1997).

[21] K. Okimura, J. Sakai, and S. Ramanathan, J. Appl. Phys. **107**, 063503 (2010).

[22] K. Okimura and N. Kubo, Thin Solid Films **515**, 4992 (2007).

[23] Y. Nihei, Y. Sasakawa, and K. Okimura, Thin Solid Films **516**, 3572 (2008).

[24] A. L. Pergament, P. P. Boriskov, A. A. Velichko, and N. A. Kuldin, J. Phys. Chem. Solids **71**, 874 (2010).

[25] V. S. Aliev, S. G. Bortnikov, and I. A. Badmaeva, J. Appl. Phys. **115**, 204511 (2014).

[26] S. Shin, S. Suga, M. Taniguchi, M. Fujisawa, H. Kanzaki, A. Fujimori, H. Daimon, Y. Ueda, K. Kosuge, and S. Kachi, Phys. Rev. B **41**, 4993 (1990).

[27] C. Chen, Y. Zhao, X. Pan, V. Kuryatkov, A. Bernussi, M. Holtz, and Z. Fan, J. Appl. Phys. **110**, 023707 (2011).

[28] C. Ko, Z. Yang, and S. Ramanathan, ACS Appl. Mater. Interfaces **3**, 3396 (2011).

[29] D. Wang, H. Murata, and T. Oki, Hyomen Gijutsu **41**, 46 (1990).

[30] O. M. Küttel, P. Groening, R. G.Agostino, and L. Schlapbach, J. Vac. Sci. Technol. A **13**, 2848 (1995).

[31] K. Okimura and A. Shibata, Jpn. J. Appl. Phys., Part 1 **36**, 313 (1997).

[32] G. C. A. M. Janssen and J.-D. Kamminga, Appl. Phys. Lett. **85**, 3086 (2004).

[33] H. B. Profijt, M. C. M. van de Sanden, and W. M. M. Kessels, J. Vac. Sci. Technol. A Vacuum, Surfaces, Film. **31**, 01A106 (2013).

[34] M. B. Sahana, M. S. Dharmaprakash, and S. A. Shivashankar, J. Mater. Chem. **12**, 333 (2001).

[35] Y. Zhou and S. Ramanathan, J. Appl. Phys. **112**, 74114 (2012).

[36] H. Zhou, M. F. Chisholm, T.-H. Yang, S. J. Pennycook, and J. Narayan, J. Appl. Phys. **110**, 073515 (2011).

[37] J. Narayan and V. M. Bhosle, J. Appl. Phys. **100**, 103524 (2006).

[38] Y. Muraoka and Z. Hiroi, Appl. Phys. Lett. **80**, 583 (2002).

[39] T.-H. Yang, R. Aggarwal, A. Gupta, H. Zhou, R. J. Narayan, and J. Narayan, J. Appl. Phys. **107**, 053514 (2010).

[40] D.-H. Youn, J. Lee, B.-G. Chae, H.-T. Kim, S.-L. Maeng, and K.-Y. Kang, J. Appl. Phys. **95**, 1407 (2004).

[41] M. Borek, F. Qian, V. Nagabushnam, and R. K. Singh, Appl. Phys. Lett. **63**, 3288 (1993).

[42] Y. Y. Luo, L. Q. Zhu, Y. X. Zhang, S. S. Pan, S. C. Xu, M. Liu, and G. H. Li, J. Appl. Phys. **113**, 183520 (2013).

[43] M. S. B. de Castro, C. L. Ferreira, and R. R. de Avillez, Infrared Phys. Technol. **60**, 103 (2013).

[44] K. Okimura and Md. Suruz Mian, J. Vac. Sci. Technol. A **30**, 051502 (2012).

[45] Y. Oka, T. Yao, N. Yamamoto, Y. Ueda, and A. Hayashi, J. Solid State Chem. **105**, 271 (1993).

[46] E. Baudrin, G. Sudant, D. Larcher, B. Dunn, and J. M. Tarascon, Chem. Mater. **18**, 4369 (2006).

[47] Z. Chen, S. Gao, L. Jiang, M. Wei, and K. Wei, Mater. Chem. Phys. **121**, 254 (2010).

[48] W. Jiang, J. Ni, K. Yu, and Z. Zhu, Appl. Surf. Sci. **257**, 3253 (2011).

[49] Q. Wang, J. Pan, M. Li, Y. Luo, H. Wu, L. Zhong, and G. Li, J. Mater. Sci. Technol. **2**, 2 (2014).

[50] D. Ruzmetov, D. Heiman, B. B. Claflin, V. Narayanamurti, and S. Ramanathan, Phys. Rev. B - Condens. Matter Mater. Phys. **79**, 153107 (2009).

[51] I. K. Kristensen, Mater. Res. Bull. **9**, 1677 (1974).

[52] J. Li and N. Yuan, Appl. Surf. Sci. **233**, 252 (2004).

[53] C. Böhm and J. Perrin, Rev. Sci. Instrum. **64**, 31 (1993).

[54] K. Ino, S. Toshikuni, U. Takeo, and O. Tadahiro, J. Vac. Sci. Technol. A **15**, 2627 (1997).

[55] T. Nakamura and K. Okimura, Jpn. J. Appl. Phys., **42**, 5776 (2003).

[56] K. Okimura and J. Oyanagi, J. Vac. Sci. Technol. A **22**, 39 (2004).

[57] K. Appavoo, D. Y. Lei, Y. Sonnefraud, B. Wang, S. T. Pantelides, S. A. Maier, and R. F. Haglund, Nano Lett. **12**, 780 (2012).

[58] Md. Suruz Mian and K. Okimura, J. Vac. Sci. Technol. A **32**, 041502 (2014).

[59] J. Leroy, A. Crunteanu, A. Bessaudou, F. Cosset, C. Champeaux, and J. C. Orlianges, Appl. Phys. Lett. **100**, 213507 (2012).

[60] P. P. Boriskov, A. A. Velichko, A. L. Pergament, G. B. Stefanovich, and D. G. Stefanovich, Tech. Phys. Lett. **28**, 406 (2002).

[61] G. Golan and A. Axelevitch, J. Optoelectron. Adv. Mater. **6**, 189 (2004).

[62] Md. Suruz Mian and K. Okimura, Jpn. J. Appl. Phys. **53**, 035802 (2014).

CHAPTER 3

Growth of VO_2 Films on TiN/Ti/Si Substrates by Inductively Coupled Plasma-Assisted Sputtering Method

Chapter 3 Growth of VO_2 Films on TiN/Ti/Si Substrates by Inductively Coupled Plasma-Assisted Sputtering Method

3.1 Introduction

In chapter 2, the low-temperature crystal growth of VO_2 films on Ti/Si substrates was achieved by ICP-assisted sputtering method. A good crystallinity was obtained in a low substrate temperature, while crystallinity degradation was observed in the sample prepared at a high substrate temperature of 400ºC. In *R-T* characteristic, more than two orders of magnitude change in resistance was realized in the out-of-plane direction for this layered-type structure. The diffusion of O atoms and the oxidation of Ti layer were observed in the case of higher substrate temperature deposition, which is responsible for the degradation of out-of-plane IMT.

So, it is highly required to achieve a stoichiometric VO_2 films at higher substrate temperature on conductive layers suppressing the interfacial diffusion and oxidation, since VO_2 is generally known to reveal a good crystallinity at substrate temperatures higher than 400ºC.[1–3]

In this chapter, TiN, a well-known diffusion barrier was introduced as a conductive layer. TiN is widely used in contact metallization for silicon integrated circuits because of its low diffusivity and thermal stability.[4–9] TiN also acts as a concrete electrode because of its low resistivity (bulk: $1–3\times10^{-5}\Omega$ cm). In this study, TiN was used as a bottom electrode with diffusion barrier function for suppressing the diffusion of O atoms and the oxidation of Ti layer. Figure 3.1 shows the schematic out-of-plane device proposed in this chapter.

The deposited films were characterized by XRD and resistivity measurements. The crystallinity of the prepared sample was confirmed by the XRD measurements. The resistivity was measured by the four-point method. The device structure and the atomic composition were evaluated by the cross-sectional SEM images and XPS depth profiles.

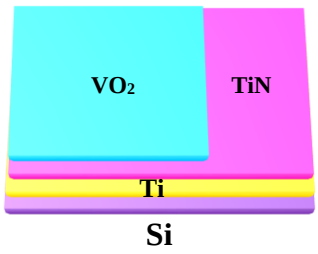

Fig.3-1 Schematic of VO_2/TiN/Ti/Si layered structure devices.

3.2 Experimental Procedure

3.2.1 Deposition Conditions of TiN Films

Before the VO_2 film deposition, Ti and TiN films were deposited by ICP-assisted sputtering and DC magnetron sputtering methods. The Ti films were deposited on the p-Si (100) substrate by the ICP-assisted sputtering method using a Ti metal target, with purity of 99.99%. The deposition condition of Ti films was as same as described in chapter 2. Then, the TiN films were deposited by a DC magnetron sputtering method with a TiN target. The atomic composition of TiN target is Ti: N = 1:1. During the deposition, the substrate temperature and rf power were kept constant respectively at 350°C and 150 W. The Ar gas flow and the base pressure were also constant at 30 sccm and 2×10^{-4} Pa, respectively. The deposition time was maintained at 14 min, producing a film thickness of around 200 nm. Electrical conductivities of Ti and TiN films were measured by using a four-point probe method. The electrical conductivities were estimated to be $1–2 \times 10^{-4}$ Ωcm for both the Ti and TiN films. The deposition conditions for both layers were given in Table 3-1.

Table 3-1 Deposition conditions and electrical resistivity of deposited Ti and TiN films.

Target	Ti (99.99%)	TiN (Ti:N=1:1)
Substrate	p-Si (100)	Ti/Si
Substrate Temperature (°C)	200	350
Ar Pressure (Pa)	1.2	0.6
Ar gas flow (sccm)	70	30
Apparatus	ICP-assisted	DC magnetron
Target-rf Power (W)	200	-
ICP-rf power (W)	150	-
DC power	-	150
Deposition Time (min)	10	14
Film Thickness (nm)	300	200
Resistivity (Ωcm)	$1–2\times10^{-4}$	$1–2\times10^{-4}$

3.2.2 Deposition Conditions of VO_2 Films

After the deposition of the bottom electrode (TiN) on Ti/Si substrates, the deposition of VO_2 films was accomplished by the ICP-assisted sputtering method. Generally, VO_2 reveals a good crystalline above 400°C in conventional magnetron sputtering[10–12], and in comparatively higher deposition temperatures in methods such as PLD[1,2,13,3,14] and CVD.[15,16] In this chapter, the deposition was executed only by the ICP-assisted sputtering method. ICP-assisted sputtering apparatus has a great potential in the low-temperature deposition because of the effect of high energy ion incidence onto the substrate during the deposition as was investigated in the previous chapter.[17–19] The substrate temperatures were varied from 150 to 400°C and were compared to the VO_2/Ti/Si results.

During the deposition of VO_2 films, the target rf-power and the ICP-rf power were both set at 200 W. The total gas pressure was 0.5 Pa with an oxygen flow of 1.0 sccm (sccm: standard cubic centimeter). The deposition time was 20 min, producing the film thickness of around 200 nm. The prepared samples were characterized by the XRD measurements, out-of-plane *R-T* characteristics, FE-SEM, cross-sectional SEM, XPS depth profiles, and out-of-plane *I-V* measurements.
The deposition conditions were given in Table 3-2.

Table 3-2 Deposition conditions of VO_2 films.

Target	V (99.9%)
Substrate	TiN/Ti/Si
Substrate Temperature (°C)	100-400
(Ar+O_2) Pressure (Pa)	0.5
Ar gas flow (sccm)	50
O_2 gas flow (sccm)	1.0
Target-rf Power (W)	200
ICP-rf Power (W)	200
Deposition Time (min)	20

3.3 Results and Discussion

3.3.1 XRD Patterns of TiN Films Deposited on Ti/Si Substrates

Figure 3-2 shows the XRD 2θ scan patterns for the prepared samples. Peaks from the initial Ti layer were found at 35.05°, 38.05°, 39.95°, 52.29º, 62.86º, 74.85º, and 77.25º, corresponding to Ti (100), (002), (101), (102), (110) (200), and (201) planes, respectively. These results suggested that Ti films were grown on Si substrates with a polycrystalline manner. Diffractions from the TiN films were observed at 2θ=36.69°, 42.63°, 61.86°, 74.17°, and 77.96°, which are corresponding to cubic (Fm3m, a: 4.241 Å) TiN (111), (200), (220), (311), and (222) planes, respectively. The results showed the polycrystalline growth of TiN on Ti/Si substrates.

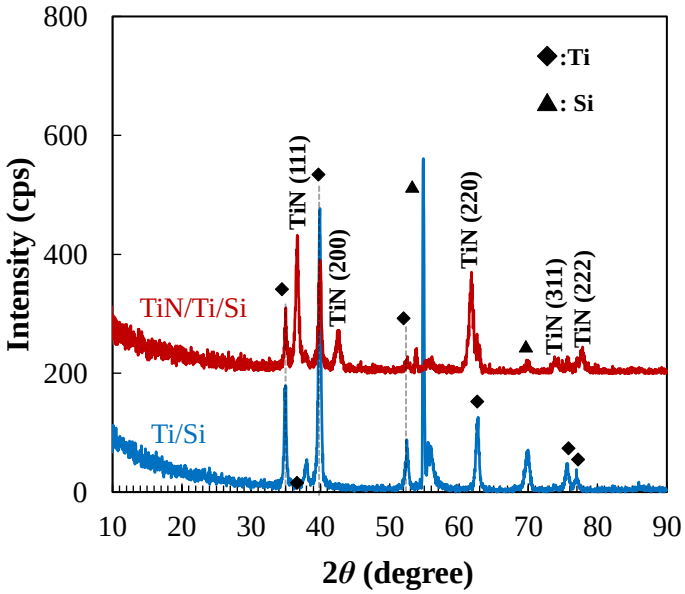

Fig. 3-2 XRD Patterns of TiN films deposited on Ti/Si substrates.

3.3.2 XRD 2θ scan Patterns of VO_2 Films Deposited at Different Substrate Temperatures

The crystallinity of the samples fabricated at different substrate temperatures was discussed by the XRD 2θ scan measurement. 2θ scan, which is suitable for the analysis of polycrystalline thin films, was presented. The incident angle of X-rays was kept at 2º. Figure 3-3 shows the XRD 2θ scan patterns for all samples prepared. *X*-axis represents diffraction angle, and *Y*-axis presents the peak intensity. In Fig. 3-3, diffractions from hcp-Ti (100), (002), (101), (102), (110), (200), and (201) planes were observed at 2θ=25.05°, 38.05°, 39.95°, 52.29°, 62.86°, 74.85° and 77.25°, respectively. As already described in section 2.3.1-2, the growth of Ti films on Si substrates in a polycrystalline manner was confirmed.

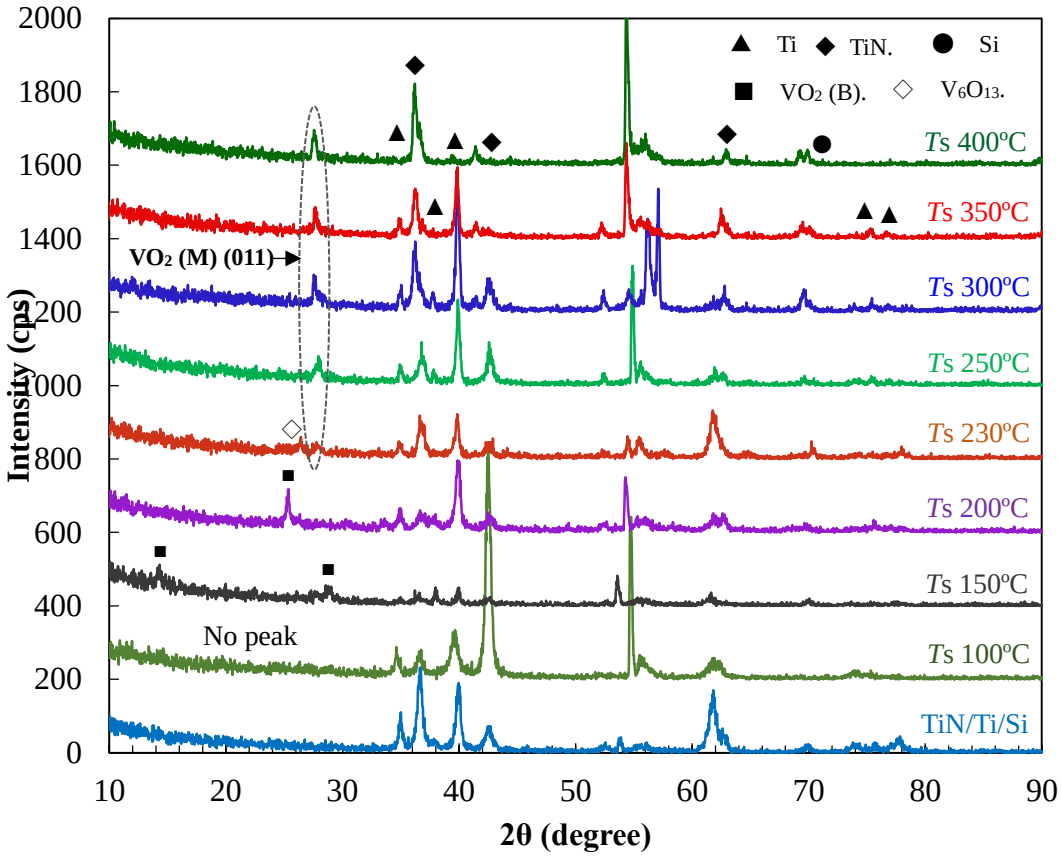

Fig. 3-3 XRD 2θ scan patterns of the samples prepared at different substrate temperatures.

Diffractions at 2θ=36.69°, 42.63°, 61.86°, 74.17°, and 77.96° corresponded to cubic (Fm3m, a: 4.241 Å) TiN (111), (200), (220), (311), and (222) planes, respectively. These results suggest that the TiN film crystallized on Ti/Si substrates with maintaining a polycrystalline manner. Diffraction from

crystalline VO_X was not observed in the sample deposited at 100ºC, while peaks from VO_2 (B) (001) and (002) planes were observed at 2θ=14.39° and 29.07°, respectively. When the substrate temperature increased to 200ºC, a single peak from the VO_2 (B) (110) plane was observed at 25.0°. However, diffraction from monoclinic VO_2 (011) plane was not detected. Later, as the substrate temperature was increased to 250ºC, the peak from VO_2 (B) phase disappeared, and diffraction from the monoclinic VO_2 (M) (011) plane was observed at 27.85º together with a peak from the V_6O_{13} phase. Besides, as the substrate temperature increased from 250 to 400ºC, only single peak of VO_2 (M) (011) plane was detected. The peak intensity increased with increasing of substrate temperature. On the other hand, VO_2 (M) peak intensity decreased when the substrate temperature increased to a value higher than 250ºC in the VO_2/Ti/Si structure, suggesting a significant improvement in the growth of VO_2 (011) at higher substrate temperatures in VO_2/TiN/Ti/Si devices. VO_2 (011) peak intensity evolution with increasing *T*s was illustrated in Fig. 3-4.

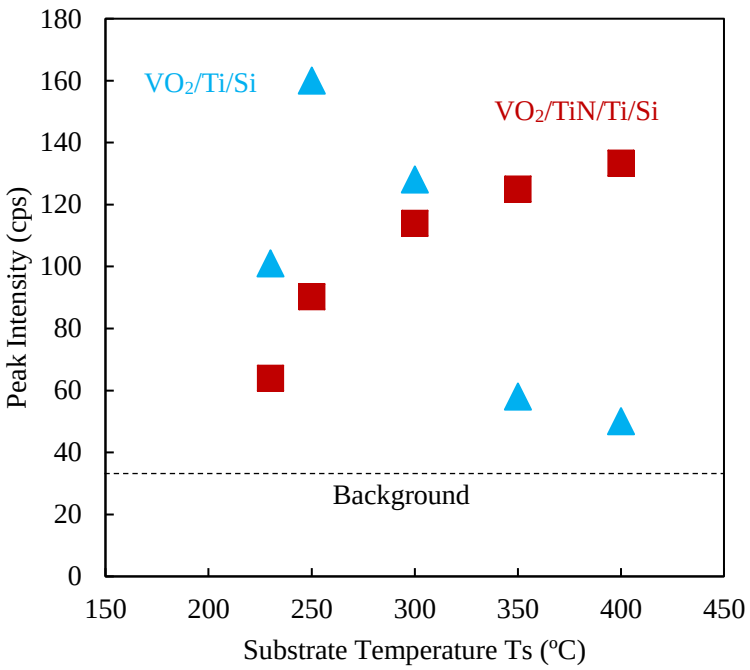

Fig. 3-4 Changes of peak intensity for VO_2 (011) plane observed in XRD patterns for both VO_2/Ti/Si and VO_2/TiN/Ti/Si structures.

3.3.3 *R-T* Characteristics of VO_2 Films Deposited at Different Substrate Temperatures

In chapter 2, out-of-plane *R-T* characteristic with more than two orders of magnitude change in resistance was observed in the sample prepared at 250ºC for the VO_2/Ti/Si structure. However, the IMT was degraded with increasing substrate temperature. Diffusion of Ti atoms and the oxidation of Ti layers were responsible for such deterioration of IMT in the out-of-plane direction as was confirmed by the XPS results. Figure 3-5 shows the out-of-plane IMT characteristics for the samples prepared at different substrate temperatures. The inset shows the schematic of out-of-plane *R-T* measurement method.

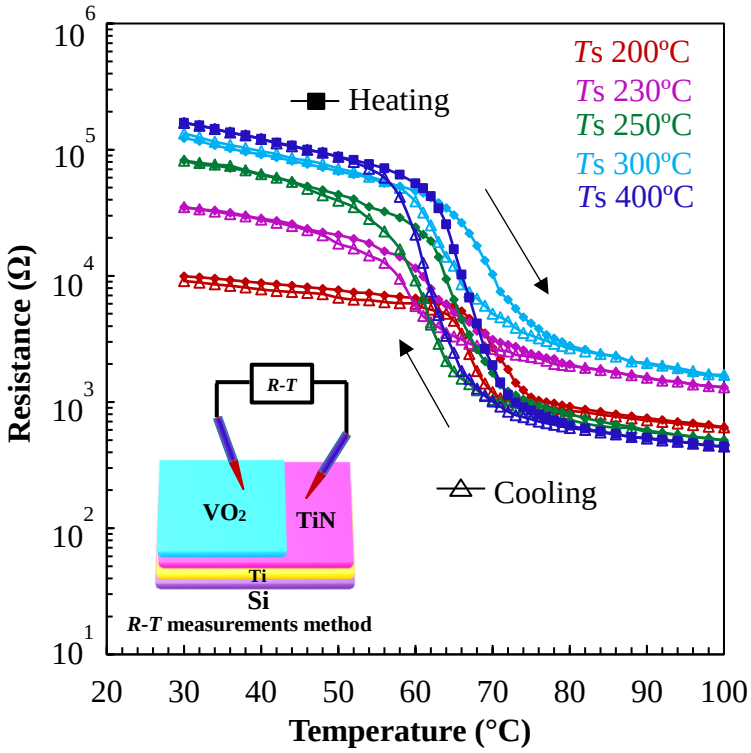

Fig. 3-5 *R-T* characteristics of VO_2 films deposited on TiN/Ti/Si substrates at different substrate temperatures.

In this case, the TiN film was used as a bottom electrode and the probe was tungsten carbide (WC) with a diameter of 50 μm. In Fig. 3-5, all samples prepared at different temperatures from 200 to 400°C revealed the out-of-plane IMT. However, in the case of the VO_2/Ti/Si structure, IMT was realized only for the sample prepared at low substrate temperatures from 200 to 300°C, while IMT was not observed at high substrate temperatures from 350 to 400°C, due to the interfacial diffusion of O atoms and the oxidation of Ti layer. In contrast, a superior and the larger out-of-plane IMT with more than 2.3 orders of magnitude change in resistance with highest initial resistance of 163 kΩ was realized in the

VO_2/TiN/Ti/Si structure prepared at 400°C.

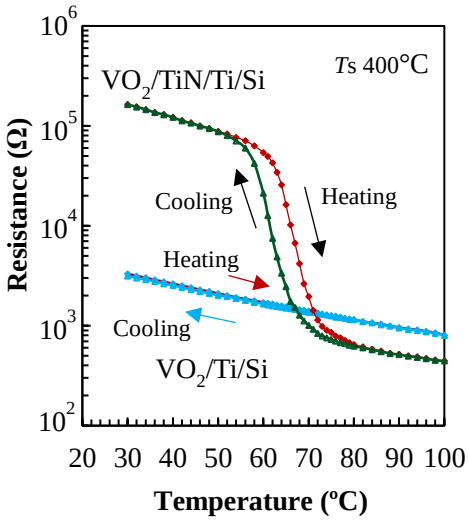

Fig. 3-6 A comparison of the *R-T* characteristics for the samples prepared at *T*s = 400°C for both structures.

Significant improvement was observed in the sample prepared at 400ºC on TiN/Ti/Si substrates compared to Ti/Si substrates. These result suggested that the TiN film worked as an electrode and suppressed the diffusion of O atoms. The details will be described in the XPS section. A weak transition was observed for the sample prepared at 200ºC, in which the VO_2 (B) phase was dominantly grown, as was observed in XRD pattern of Fig. 3-3. The IMT was not obtained at temperatures lower than 200ºC (not shown here). A comparison of the *R-T* characteristics for the layers grown at *T*s = 400°C for both structures is given in Fig. 3-6.

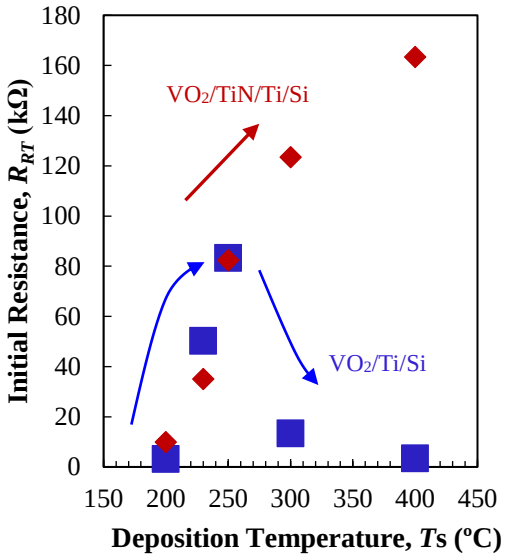

Fig. 3-7 Changes of R_{RT} with substrate temperatures for both structures.

The initial resistance increased with increasing substrate temperature and the highest initial resistance, R_{RT} of 163 kΩ, was obtained in the sample of 400°C, while the R_{RT} decreased with increasing substrate temperature in the case of VO_2/Ti/Si structure. Changes of R_{RT} with substrate temperature for the both structures are given in Fig. 3-7.

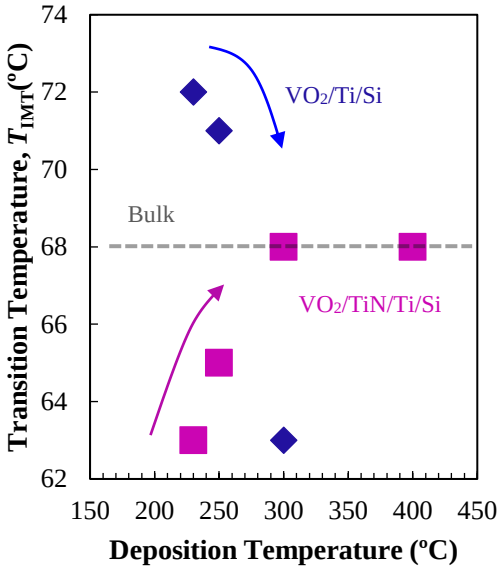

Fig. 3-8 Transition temperatures of VO_2 films fabricated on Ti/Si and TiN/Ti/Si substrates at different substrate temperatures.

The monotonic increase of R_{RT} with increasing temperature in VO_2/TiN/Ti/Si structures proposed a significant improvement of VO_2 crystallinity on the TiN buffer layer. Figure 3-8 displays the changes of T_{IMT} for samples prepared at different T_S for the both device structures of VO_2/Ti/Si and VO_2/TiN/Ti/Si. In the VO_2/Ti/Si structure, T_{IMT} was observed at 72°C for the sample prepared at T_S of 230°C and T_{IMT} decreased below 68°C, with the increase of T_S. In contrast, in the case of the VO_2/TiN/Ti/Si structure, T_{IMT} was at 63°C for the sample fabricated at 230°C and increased with T_S. T_{IMT} was found at 68°C for the samples prepared at 300 - 400°C. The T_{IMT} at 68°C is identical to the IMT temperature for bulk VO_2 crystal.[20]

The IMT properties of VO_2 films deposited on TiN/Ti/Si substrates at the different substrate temperatures from 230 to 400°C are summarized in Table 3-3.

Table 3-3 IMT properties of VO_2 films fabricated on TiN/Ti/Si substrates at different *T*s.

Sub. Temp	R_{RT} (kΩ)	R_{100} (kΩ)	$T_{IMT\text{-}H}$ (°C)	$T_{IMT\text{-}C}$ (°C)	ΔH (°C)	ΔR
200°C	9.9	0.63	71	68	3	0.9
230°C	35.0	1.30	63	60	3	1.2
250°C	82.3	0.49	65	62	3	1.9
300°C	123	1.60	68	63	5	1.5
400°C	163	0.44	68	61	7	2.3

3.3.4 Surface SEM Images of VO_2 Films Deposited at Substrate Temperatures of 250 and 400°C

Figure 3-9 shows surface SEM images for VO_2 films on TiN/Ti/Si substrates prepared at (a) 250°C and (b) 400°C, respectively. Herein, only low (250°C) and high (400°C) substrate temperatures were focused. In Fig. 3-9 (a), larger crystal grains with sizes of 100 - 500 nm were observed for the sample prepared at 250°C. On the other hand, smaller crystal grains with sizes of 100–300 nm were obtained for the sample of 400°C as shown in Fig. 3-9 (b). In this case, the crystal grains are not densely filled and grain boundaries were also observed. Such grain boundaries are responsible for the increase of the initial resistance and are forming an another current path in the out-of-plane direction, and are also responsible for the realization of large IMT.[21,22]

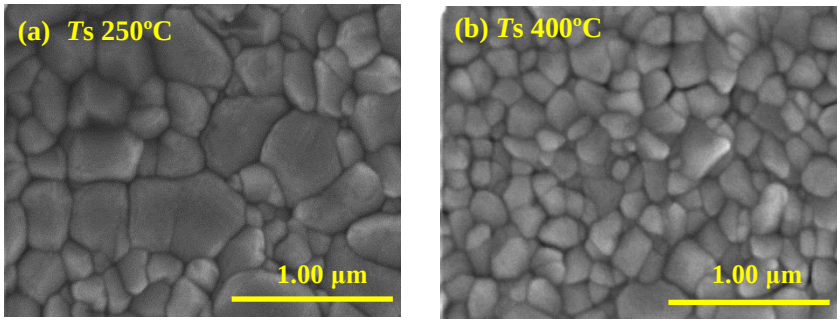

Fig. 3-9 Surface SEM images of VO_2 films fabricated on TiN/Ti/Si substrates at low (250°C) substrate temperature (a) and high (400°C) substrate temperature (b).

3.3.5 Cross-sectional SEM Images of VO_2 Films Deposited at Substrate Temperatures of 250 and 400°C

Figure 3-10 (a) and (c) shows cross-sectional SEM images of the samples fabricated at 250°C and 400°C on TiN/Ti/Si substrates. Fig 3-10 (b) and (d) represent the cross-sectional SEM images for the samples prepared at 250°C and 400°C on the Ti/Si layer as already shown in Fig. 2-20 in chapter 2. In Fig. 3-10 (a), three layers consisting of VO_2, TiN and Ti were clearly observed on Si substrates with sharp interfaces at the lower temperature of 250°C. In the case of VO_2/Ti/Si structure, VO_2, Ti and Si were clearly observed at a lower temperature of 250ºC as shown in Fig. 3-10 (b).

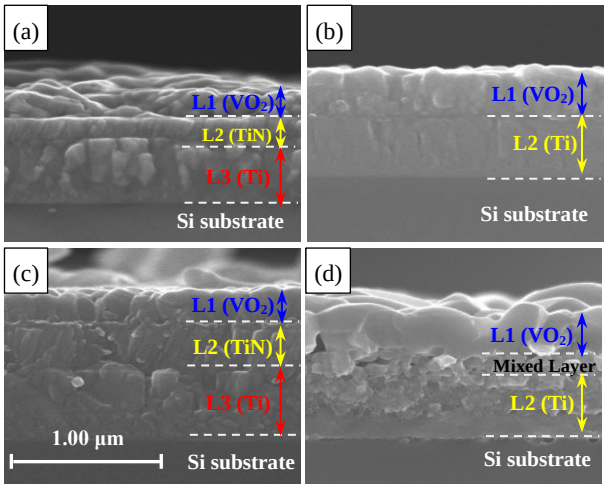

Fig. 3-10 Cross-sectional SEM images of VO_2 films fabricated on TiN/Ti/Si substrates at low (250°C) substrate temperature (a) and high (400ºC) substrate temperature (c). (b) and (d) present for the VO_2/Ti/Si structure deposited at the same temperatures. Fig. 3-10 is "Reproduced with permission from [Md. Suruz Mian and K. Okimura, J. Vac. Sci. Technol. A **32**, 041502 (2014)]. Copyright [2014], American Vacuum Society."

Three layers with consisting of VO_2, TiN, and Ti were also clearly apparent on Si substrates in the sample prepared at a higher temperature of 400°C in the VO_2/TiN/Ti/Si structure without any mixing layer between the VO_2 film and the TiN layer. Sharp interfaces between the VO_2 film and theTiN layers and between the TiN and the Ti layers were also observed. These results suggested that the TiN film acted as a diffusion barrier and suppressed the diffusion of O atoms into the Ti layer, which led to realize a sharp interface in sample deposited at a higher substrate temperature. Such sharp interface is essential to achieve a superior out-of-plane IMT.[21,23] However, in VO_2/Ti/Si structures, mixing layer between the VO_2 film and the Ti layer was observed in the sample prepared at 400°C shown in Fig. 3-10 (d).

3.3.6 XPS Depth Profiles of VO_2 Films Deposited at Substrate Temperatures of 250 and 400°C

In this section, XPS depth profiles were examined in order to investigate the atomic composition and interface condition between the VO_2 film and the bottom electrode. Figure 3-11 (a) shows the XPS depth profiles for the sample prepared at 250°C on the TiN/Ti/Si substrates and Fig. 3-11 (b) shows the XPS depth profiles of VO_2/Ti/Si structure deposited at the same temperature .

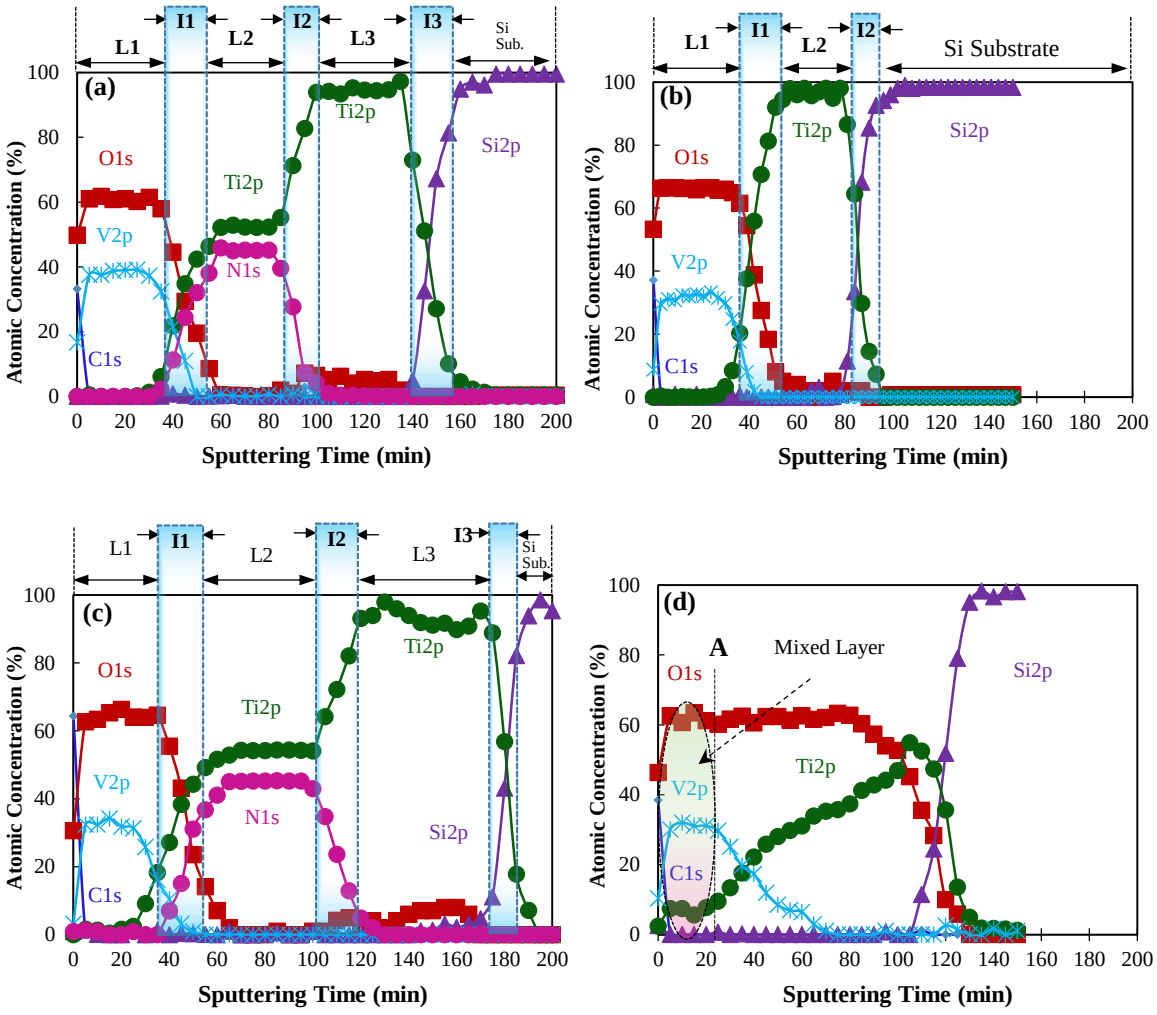

Fig. 3-11 XPS depth profiles of VO_2 films fabricated on TiN/Ti/Si substrates at (a) 250°C and (c) 400°C. Images of (b) and (d) present the XPS depth profiles of VO_2/Ti/Si structures, where (b) for 250°C and (d) for 400°C, respectively. This Figure is "Reproduced with permission from [Md. Suruz Mian and K. Okimura, J. Vac. Sci. Technol. A **32**, 041502 (2014)]. Copyright [2014], American Vacuum Society."

XPS spectra were taken for C 1*s*, N 1*s*, O1*s*, Si 2*p*, V2*p*, and Ti 2*p* after every 2 min sputtering by

Ar ions with an acceleration energy of 2 kV. In Fig. 3-11, the horizontal axis shows the total Ar-ion sputtering time. The vertical axis represents the atomic concentration. The atomic concentrations were derived from the area of each atomic spectrum. In Fig. 3-11 (a), three layers (L1, L2, and L3) were designated on Si substrates as the same as observed in the cross-sectional SEM image in Fig. 3-10 (a). In this case, the VO_2 film was almost stoichiometry. In the TiN buffer layer, the N atom concentration was slightly smaller than stoichiometry. This fact probably indicated the initial TiN film quality. A sharp interface was observed between the VO_2 film and the TiN layer, suggesting that the TiN layer acts as an electrode for the sample prepared at 250ºC. Consequently, superior IMT was realized for the low substrate temperature of 250ºC as illustrated in Fig. 3-5. These results were the same as the case of the VO_2/Ti/Si structure are shown in Fig. 3-11 (b).

Figure 3-11 (c) shows the XPS depth profiles of the VO_2/TiN/Ti/Si structure with the VO_2 film deposited at 400ºC. As shown in Fig. 3-11 (c), a significant improvement was observed despite the high deposition temperature of 400°C. A sharp interface between the VO_2 film and the TiN layer was obtained at this high temperature similar to that of the sample of 250°C. Although a very small amount of Ti atoms in the VO_2 region and the O atoms in the TiN region were also observed at this temperature. On the other hand, significant diffusion of O atoms and oxidation of Ti layer were observed in the sample fabricated at T_S of 400ºC in the VO_2/Ti/Si structure. A metallic Ti layer (L3) was also maintained in this case. These results clarified that the diffusion of O atoms and the oxidation of Ti layer were suppressed by the TiN buffer layer in the VO_2/TiN/Ti/Si structure, even at the VO_2 deposition temperature of 400°C. The realization for both stoichiometric crystalline VO_2 films and the sharp interface enabled to fabricate a layered device with the intrinsic IMT of the VO_2 film. Figure 3-11 (d) shows the XPS depth profile of the VO_2/Ti/Si structure with the VO_2 film deposited at 400ºC (This figure is reused for the comparison with the VO_2/TiN/Ti/Si structure). In this case, the top layer was observed to mix with the Ti atoms. Additionally, oxidation of the Ti layer also caused the formation of a TiOx layer on Si substrates. Such the diffusion of O atoms and the oxidation of the bottom Ti layer resulted in the disappearance of IMT in the sample prepared at 400°C for the VO_2/Ti/Si structure.

3.3.7 *I-V* Characteristics of VO_2 Films Deposited at Substrate Temperatures of 250 and 400°C

Current–voltage characteristics (*I-V*) in the out-of-plane direction of the VO_2/TiN/Ti/Si structure using the TiN layer as a bottom electrode were investigated for the low (250°C) and high (400°C) substrate temperatures by using a curve tracer. A 50 Hz sinusoidal voltage was applied through 100 Ω series resistance by contacting probe. Figure 3-12 presents the *I–V* curves for the samples deposited at 250 and 400°C.

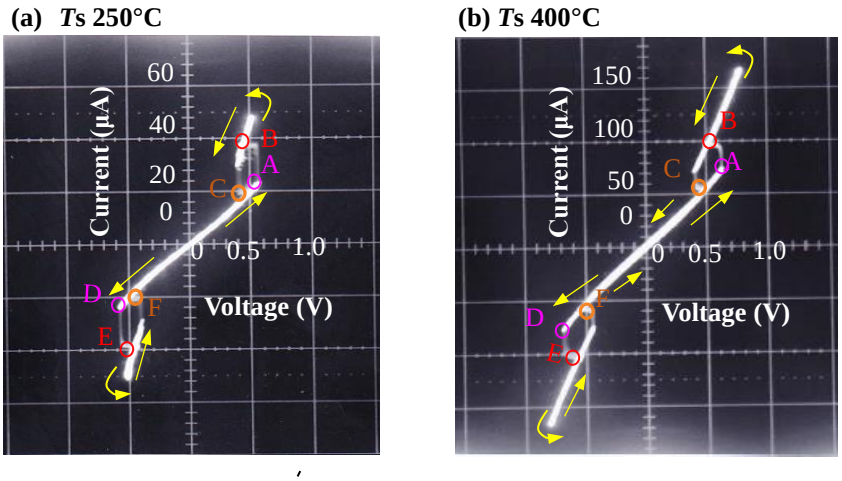

Fig. 3-12 *I-V* characteristics of VO_2 films fabricated on TiN/Ti/Si substrates at (a) 250ºC and (b) 400ºC. Figure 3-12 is "Reproduced with permission from [Md. Suruz Mian and K. Okimura, J. Vac. Sci. Technol. A **32**, 041502 (2014)]. Copyright [2014], American Vacuum Society."

In Fig. 3-12 (a), threshold switching was observed at the applied voltage of 0.55 V. The threshold switching current was estimated to be about 22 μA, labeled as "A". This switching current obtained in this sample is the lowest value ever reported for the VO_2-based devices. Then the *I–V* curve followed A → B → C cycle, and reached to the initial trace at point of "C". In the negative bias, similar threshold switching was appeared at point of "D", with -0.55 V, -22 μA, and *I–V* repeated the loop labeled D → E → F. This symmetric *I–V* characteristic against applied sinusoidal voltage was the same as that of typical VTRS inVO_2-based two-terminal planar type devices. The symmetry characteristic represented that metal electrode behave as an Ohmic contact, not as a Schottky barrier. The threshold electric field E_{th} that triggered the VTRS was estimated to be 2.8×10^6 V/m from the 0.55 V onset voltage and 200 nm film thickness. The power consumption of 12.1 μW achieved in this device has a great potential for the application of VO_2-based devices.

In the case of 400ºC, the threshold switching was realized at the applied voltage of 0.60 V and the I_{th}

was observed to be about 55 μA, which were rather higher compared to the case of 250ºC. The *I-V* curve followed the A → B → C cycle, and it reached to the initial trace as labeled as C. The same loop was obtained for the negative voltages. The diffusion of O atoms and the oxidation of TiN layer in the vicinity of the interface, which were recognized at the I1 in Fig. 3-11 (c), may be responsible for the increasing of V_{th} and I_{th} at 400ºC .The power consumption was estimated to be about 33.0 μW. The calculated E_{th} was about 3.0×10^6 V/m. These values of E_{th} are the same order as that reported for nanogap and nanocontact VO_2 junctions. [24,25] For this discrepancy, we speculate that the presence of lower oxidized states in the interface shown in the XPS depth profile, which affect the onset field to shift towards a lower value. Yang *et al.* suggested that the power consumption is suppressed by introducing a layered structure for future advancement.[26] The present layered type device with low power consumption has a great potential for realizing VO_2-based switching device.

3.4 Conclusions

In the previous chapter, the out-of-plane IMT with more than 2.6 orders of magnitude change in resistance was achieved for the sample deposited on Ti/Si substrates at low substrate temperature. However, such IMT was observed to disappear in the sample prepared at a high substrate temperature of 400ºC due to the diffusion of O atoms and the oxidation of Ti layer. In this chapter, TiN was introduced as a diffusion barrier with the aim of accomplishing a good crystallinity of VO_2 films even at a high substrate temperature of 400ºC. TiN was deposited on Ti/Si substrate by DC magnetron sputtering method. The deposited TiN films showed polycrystalline feature and low resistivity on the order of 10^{-4} Ω cm, as confirmed by the XRD and resistivity measurements. Then, VO_2 films was fabricated on TiN/Ti/Si substrates by the ICP-assisted sputtering method. The substrate temperature was varied from 100 to 400ºC. The crystallinity was evaluated by the XRD 2θ scan measurements.

In XRD results, diffraction from the (011) plane was observed on all samples prepared at 250 - 400ºC. A significant improvement was found in the VO_2/TiN/Ti/Si structure; the peak intensity was increased with increasing substrate temperature, and the highest peak intensity was achieved in the sample of 400ºC. These results implied that a good crystallinity of VO_2 films was achieved at a high substrate temperature of 400ºC, while the degradation of crystallinity was obtained in the VO_2/Ti/Si structure fabricated at 400ºC. Peaks from VO_2 (B) metastable phase were observed on the samples deposited at 150 and 200ºC, while any peak from VOx was not observed at 100ºC.

In *R-T* characteristics, the R_{RT} was increased with increasing substrate temperature, and two orders of magnitude changes in resistance were realized at the lower substrate temperature of 250-350ºC. Rather larger resistance drop with more than 2.3 orders of magnitude was observed at 400ºC. These results correspond to the XRD results in which highest peak intensity was obtained at 400ºC. The T_{IMT} was found to be 68ºC in the sample of 400ºC, which is identical to the generally recognized IMT temperature for bulk VO_2 crystal.

In XPS, a sharp interface was observed in the sample prepared at a lower substrate temperature of 250ºC, which is same as VO_2/Ti/Si structure. Furthermore, an abrupt interface was also obtained for the sample prepared at 400ºC in VO_2/TiN/Ti/Si structures, though a very small amount of Ti atoms in the VO_2 region and the O atoms in the TiN region were also observed. On the other hand, significant diffusion of O atoms and the oxidation of Ti layer were observed in the sample fabricated at T_S of 400ºC in the VO_2/Ti/Si structure. These results indicate a drastic improvement in VO_2/TiN/Ti/Si structures, in which TiN layer suppressed the oxidation of Ti layer. Furthermore, three layers with clear interface were also confirmed in the cross-sectional SEM images, which is vitally important to realize a sharp interface between the VO_2 film and the metal laye6r, and led to the abrupt IMT in the out-of-plane direction.

In out-of-plane *I-V* characteristics, switching was observed at the applied voltage of 0.55 V, and the switching current was 22 μA for the sample prepared at a substrate temperature of 250ºC. On the other

hand, V_{th} and I_{th} were designated at 0.60 V and 55 μA for the sample prepared at 400ºC, respectively. Rather higher values of V_{th} and I_{th} at 400ºC were considered to be responsible for observed small diffusion of O atoms at the interface between the VO_2 film and TiN layer.The switching electric field was estimated to be 2.8×10^6 V/m and 3.0×10^6 V/m for both substrate temperatures of 250 and 400ºC. The estimated electric field was in the same order as previously reported value for VO_2 nanocontact and nanogap junction. The calculated power consumption at 250 ºC was 12.1 μW, which is the lowest value ever reported in VO_2-based two-terminal planar type devices and as well as layered type device. The present layered type device with low switching voltage and low power consumption offers a great potential for the application as a low voltage and low power consumption selective switch which is highly required for the next generation high-speed non-volatile memory device.

References

[1] K. Okimura, J. Sakai, and S. Ramanathan, J. Appl. Phys. **107**, 063503 (2010).

[2] D. H. Kim and H. S. Kwok, Appl. Phys. Lett. **65**, 3188 (1994).

[3] T.-H. Yang, R. Aggarwal, A. Gupta, H. Zhou, R. J. Narayan, and J. Narayan, J. Appl. Phys. **107**, 053514 (2010).

[4] M. Wittmer, B. Studer, and H. Melchior, J. Appl. Phys. **52**, 5722 (1981).

[5] M. Wittmer, J. R. Noser, and H. Melchior, J. Appl. Phys. **54**, 1423 (1983).

[6] J. Y. Park, J. Y. Kim, Y. D. Kim, H. Jeon, and Y. Kim, J. Korean Phys. Soc. **42**, 817 (2003).

[7] S.-K. Rha, W.-J. Lee, S.-Y. Lee, Y.-S. Hwang, Y.-J. Lee, D.-I. Kim, D.-W. Kim, S.-S. Chun, and C.-O. Park, Thin Solid Films **320**, 134 (1998).

[8] S. Q. Wang, I. Raaijmakers, B. J. Burrow, S. Suthar, S. Redkar, and K. B. Kim, J. Appl. Phys. **68**, 5176 (1990).

[9] T. Q. Li, S. Noda, Y. Tsuji, T. Ohsawa, and H. Komiyama, J. Vac. Sci. Technol. A **20**, 583 (2002).

[10] M. B. Sahana, G. N. Subbanna, and S. A. Shivashankar, J. Appl. Phys. **92**, 6495 (2002).

[11] M. Tangirala, K. Zhang, D. Nminibapiel, V. Pallem, C. Dussarrat, W. Cao, T. N. Adam, C. S. Johnson, H. E. Elsayed-Ali, and H. Baumgart, ECS J. Solid State Sci. Technol. **3**, N89 (2014).

[12] M. S. B. de Castro, C. L. Ferreira, and R. R. de Avillez, Infrared Phys. Technol. **60**, 103 (2013).

[13] Y. Muraoka and Z. Hiroi, Appl. Phys. Lett. **80**, 583 (2002).

[14] M. Borek, F. Qian, V. Nagabushnam, and R. K. Singh, Appl. Phys. Lett. **63**, 3288 (1993).

[15] M. B. Sahana, M. S. Dharmaprakash, and S. A. Shivashankar, J. Mater. Chem. **12**, 333 (2001).

[16] D. Vernardou, D. Louloudakis, E. Spanakis, N. Katsarakis, and E. Koudoumas, Sol. Energy Mater. Sol. Cells **128**, 36 (2014).

[17] K. Okimura and N. Kubo, Thin Solid Films **515**, 4992 (2007).

[18] Y. Nihei, Y. Sasakawa, and K. Okimura, Thin Solid Films **516**, 3572 (2008).

[19] Md. Suruz Mian and K. Okimura, Jpn. J. Appl. Phys. **53**, 035802 (2014).

[20] F. J. Morin, Phys. Rev. Lett. **3**, 34 (1959).

[21] Md. Suruz Mian and K. Okimura, J. Vac. Sci. Technol. A **32**, 041502 (2014).

[22] D. Brassard, S. Fourmaux, M. Jean-Jacques, J. C. Kieffer, and M. A. El Khakani, Appl. Phys. Lett. **87**, 1 (2005).

[23] K. Okimura and Md. Suruz Mian, J. Vac. Sci. Technol. A **30**, 051502 (2012).

[24] D. Ruzmetov, G. Gopalakrishnan, J. Deng, V. Narayanamurti, and S. Ramanathan, J. Appl. Phys. **106**, 083702 (2009).

[25] J. Leroy, A. Crunteanu, A. Bessaudou, F. Cosset, C. Champeaux, and J. C. Orlianges, Appl. Phys. Lett. **100**, 213507 (2012).

[26] Z. Yang, C. Ko, and S. Ramanathan, Annu. Rev. Mater. Res. **41**, 337 (2011).

CHAPTER 4

Self-sustaining Oscillation of VO_2-Based Layered Type Device

Chapter 4 Self-sustaining Oscillation of VO_2-Based Layered Type Device

4.1 Introduction

As described before, VO_2 has attracted much attention due to its sharp first-order insulator-metal transition (IMT) near to room temperature of 68°C.[1–4] It was reported that this IMT of VO_2 can be triggered by the different external parameters, such as thermal, electrical and optical excitation, and as well as strain, making VO_2 to be as a most promising material. However, physics of the transition in VO_2 are still under debate. While some studies suggest that the transition is a Peierls transition,[5–7] some other studies favor that it is a Mott transition.[8–11] Voltage triggered resistance switching (VTRS) of VO_2 was first reported in the1960s.[12,13] Since then, the VTRS of VO_2 has actively been studied by others.[9,10,14–16] VTRS that occurred due to the occurrence of IMT in VO_2 thin films has been a central subject in attempt to realize an electrical switching devices,[2,9,10,14,17,18] though there are remaining discussions regarding the contribution of local temperature rise by current induced Joule heating effect.[17,19,20]

Generally, It is known that self-sustaining oscillation phenomenon can be triggered in such a device which shows a negative differential resistance (NDR) region in its *I-V* characteristics. VO_2 also exhibits a NDR region in *I-V* characteristics. Self-sustaining oscillation in VO_2 has been investigated from the 1970s. Oscillation in VO_2 bulk crystal was firstly reported by Taketa *et al*. with frequency of 0.9 kHz at room temperature in 1975.[21] Then, in 1978, rather high oscillation frequency of 5 kHz for VO_2 needles was reported by Fisher.[22] After that, there was no report on oscillation in VO_2 until Sakai reported it in 2008, in which the oscillation was observed in VO_2-based two-terminal planar type devices with the frequency of 556 kHz.[23] Sakai suggested that the oscillation occurred only under a certain combination of the source voltage and load resistance. Then, the electrical oscillation of VO_2-based two-terminal planar type devices was reported by Kim's group in late 2008.[24,25] Therefore, at present self-sustaining oscillations of VO_2 films were actively studied and were frequently reported.[25–31] This oscillation in VO_2 is triggered by the threshold switching characteristics, which is accompanied by the negative differential resistance (NDR). Sakai and Kim's groups suggested that the restoring force in the series resistance occurred in the metallic state of VO_2, then getting back to the insulating state, and resulting in self-sustaining oscillation of the voltage across VO_2.[23,25,32] Time constant (τ), which is determined by series resistance and capacitance in the circuit, is considered to be a decisive factor in deciding the oscillation frequency (f_{osc}).[27] To date, the values of f_{osc} were reported to range in order of several hundred kHz for VO_2-based two-terminal planar type devices, with the τ in the order of several μs. In the VO_2-based two-terminal planar type devices, electrode areas and spacing are designed to be in μm-order scale, resulted in a low oscillation frequencies. Recently, Beaumont *et al.* reported oscillation in VO_2-based out-of-plane configuration, in which VO_2 film was sandwiched by

crossbar electrodes, realizing a narrower electrodes spacing.[29] They reported rather lower threshold current (~ 0.6 mA) and voltage (~ 0.8 V) in *I-V* characteristics and f_{osc} up to 300 kHz by the current injection. Out-of-plane configuration has a great potential for lowering both threshold voltage and current in switching, and also controlling the f_{osc}. This is due to the defined electrode spacing, which is corresponding to the films thickness in the out-of-plane configuration. Furthermore, high-frequency self-sustaining oscillation with a frequency of MHz order and parametric dependence of the oscillation frequency in both configurations have not yet been reported. This parametric study is important in order to clarify the mechanism of self-sustaining oscillation in VO_2-based devices. In addition, self-sustaining oscillation measurement is effective to investigate the stability and the speed of resistance switching.

In this chapter, the performance of self-sustaining oscillation in the VO_2-based layered type devices was investigated. As layered type devices, VO_2/Ti/Si and VO_2/TiN/Si structures were used. In the VO_2/Ti/Si structure, the sample fabricated at a low temperature of 250°C described in chapter 2 was introduced. While, the VO_2/TiN/Si structure is newly prepared in this chapter. The dependence of the oscillation frequency on source voltage, *V*s, and series resistance, R_E, was studied in the VO_2/TiN/Si structure. Parametric dependence of the oscillation frequency was investigated in the VO_2/Ti/Si structure. Before the oscillation measurements were performed, VO_2 films were deposited on TiN conductive layers at a low substrate temperature of 230°C by using the ICP-assisted sputtering method. In chapters 2 and 3, it was found that low deposition temperature of around 230°C was effective for suppressing interfacial diffusion and oxidation.[33,34] Then, the deposited films were characterized by XRD, out-of-plane *R-T*, SEM, and XPS measurements. The oscillation measurements of VO_2-based layered type device were performed. During the measurements, the dependence of oscillation frequency on geometric parameters, including the film thickness and probe diameter was examined together with the dependence on circuit parameters of source voltage and series resistance. Higher self-oscillation frequency up to 9 MHz by adjusting those parameters offers new vistas for the application of this phenomenon in the engineering fields, such as radio frequency generators and dc-rf micro inverters. Figure 4-1shows the schematic of VO_2/TiN/Si layered structure devices for this chapter.

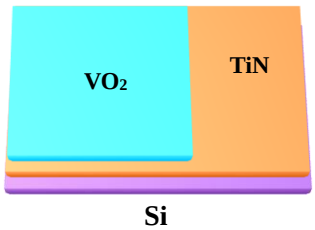

Fig. 4-1 Schematic of VO_2/TiN/Si layered structure devices.

4.2 Experimental Procedure

In chapters 2 and 3, good crystallinity with more than two orders of magnitude change in resistance in both VO_2/Ti/Si and VO_2/TiN/Ti/Si structures at *T*s of 250°C was obtained. However, the diffusion of the O atoms and the oxidation of Ti layer were observed in VO_2/Ti/Si structures at *T*s of 400°C. In chapter 3, TiN was introduced as a bottom electrode with diffusion barrier function, resulting successful suppression of the oxidation of Ti layers and realized 2.3 orders of magnitude change in resistance at *T*s of 400°C in VO_2/TiN/Ti/Si structures in which sharp interfaces were formed without diffusion of Ti.[34] Significant improvement of abruptness in the interface between VO_2 film and the conductive layer was realized in the VO_2/TiN/Ti/Si structure at 400°C, while a small amount of diffusion of the O atoms into TiN layer was recognized at this temperature. As the result, it can be concluded that low-temperature deposition is suitable for the fabrication of VO_2 films on the conductive layer. Based on this background, in this chapter, a single TiN layer (without Ti) was used as a bottom electrode to form an out-of-plane configuration. Crystallinity, *R-T* characteristics, and the interface between the VO_2 film and the TiN layer were investigated. Based on out-of-plane *I-V* characteristics, the performance of self-sustaining oscillation in layered type device was also investigated.

Before the VO_2 deposition, conductive TiN layer was deposited on Si substrates (TiN/Si structures) by the DC magnetron sputtering method. In the TiN deposition, TiN with composition ratio of Ti: N = 1:1 was used as a target material. A minute description of deposition processes of TiN films is the same as given in chapter 3.[34] The conductivity of fabricated TiN films was about 2×10^{-4} Ωcm, suitable to be used as bottom electrodes for the switching and oscillation experiments. In the deposition of VO_2 films, V metal with a purity of 99.9% was used as a target material. The total pressure of Ar and O_2 gasses was 0.5 Pa, and flow rates of Ar and O_2 were 55 sccm and 1.0 sccm, respectively. Target-rf power and ICP-rf powers were 200 W, and the deposition rate of under these conditions was 10 nm/min. The deposition time was 20 min; VO_2 film with thickness of 200 nm was produced. All measurements were performed at room temperature. The deposition conditions of VO_2/Ti/Si structures were given in chapter 2.

The crystallinity of VO_2 films was measured by the X-ray diffraction (XRD) using CuKα radiation. Layered device structure was confirmed by the cross-sectional FE-SEM. X-ray photoelectron spectroscopy (XPS) depth profiles was performed to investigate the chemical composition along the film thickness. All electrical characterizations were performed in an out-of-plane direction by two-probe method, in which tungsten carbide (WC) tips with a diameter of 50 μm were used as the probes. *I-V* analysis and oscillation observation were performed by instantly switching from one measurement circuit to another, in order to study the relationship between *I-V* and oscillation properties in the same junction.

4.3 Results and Discussion

4.3.1 XRD Pattern of VO_2 Film Deposited on TiN/Si Substrates

Figure 4-2 shows the XRD 2θ scan pattern of the VO_2 film deposited on TiN/Si substrates. Diffractions at 2θ = 36.69°, 42.63°, 61.86°, corresponding to cubic (Fm3m, a: 4.241 Å) of TiN (111), (200), and (220) planes were observed, respectively. These results suggest that the TiN film on Si substrates was crystallized while maintaining the polycrystalline manner. The preferential peak of VO_2 (M) (011) plane was detected at 2θ = 27.85°, suggesting the crystalline growth of VO_2 films on TiN/Si layer. A weak peak from the metastable VO_2 (B) (110) plane was observed at 2θ = 25.25°. VO_2 (B) is a polymorph of VO_2, which usually grows at a relatively low substrate temperature, and is metallic at room temperature.[35,36]

Cross-sectional SEM image shown in Fig. 4-2 (b) confirmed the layered structure of the fabricated VO_2/TiN/Si device. In Fig. 4-2 (b), two layers (L1 and L2) with a sharp interface between the VO_2 film and the TiN layer were clearly observed, while the oxidation and diffusion were not observed in the vicinity of the interface.

Figure 4-2 (c) shows the surface SEM image of the produced sample. The observed grain sizes were around 50 to 200 nm.

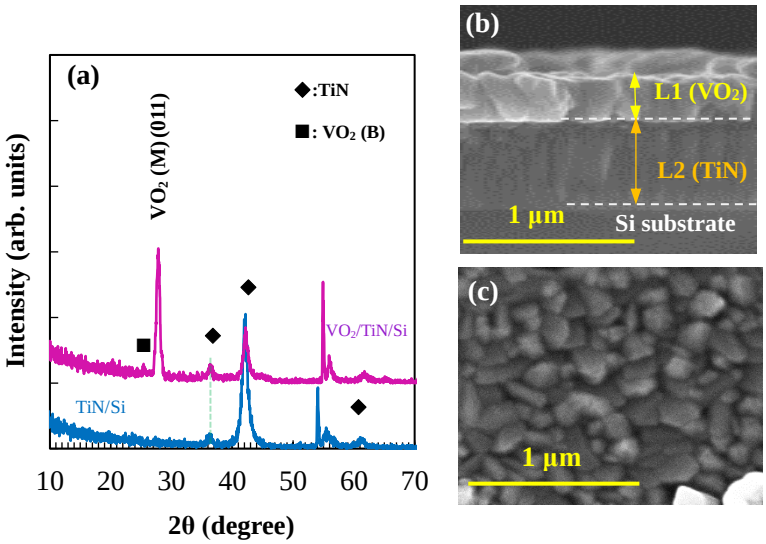

Fig. 4-2 (a) XRD 2θ scan pattern of VO_2 film deposited on TiN/Si substrates, and (b) cross-sectional SEM image and (c) surface SEM image of the produced VO_2/TiN/Si structures.

4.3.2 *R-T* Characteristics of VO_2 Film Deposited on TiN/Si Substrates

Figure 4-3 presents the out-of-plane *R-T* characteristics of VO_2 film fabricated on TiN/Si substrates. Inset shows the out-of-plane *R-T* measurement method. The deposited film revealed an out-of-plane IMT with resistance change of more than two orders of magnitude. This result suggested that the bottom layer acts as an electrode properly. Further discussion will be provided in the next section. The T_{IMT} was observed at 62ºC for the heating and 58ºC for the cooling, with hysteresis width of 4ºC. The R_{RT} was 167 kΩ and R_{100} was 318 Ω. Obtained transition temperature was rather lower than the reported value of 68ºC for VO_2 bulk crystal, which should be due to the presence of another vanadium oxide such as VO_2 (B) phase. However, the magnitude of resistance change, ΔR is the almost same as was observed for the VO_2/Ti/Si and VO_2/TiN/Ti/Si structures, which were deposited at 250ºC.

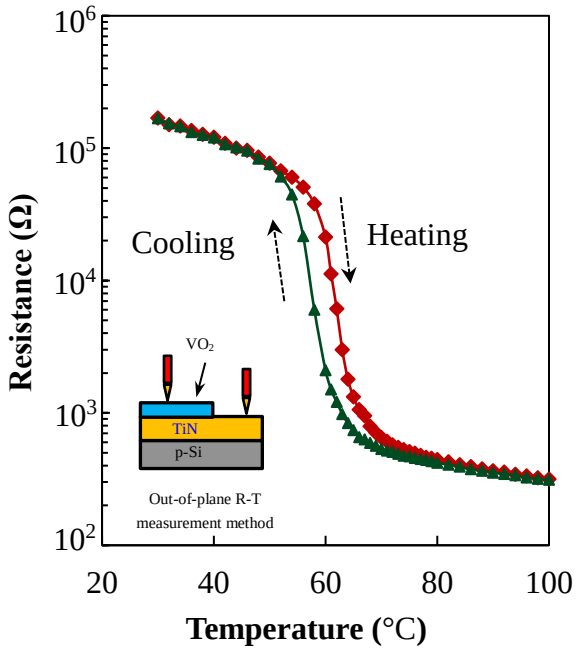

Fig. 4-3 *R-T* characteristics of the VO_2 film deposited on TiN/Si substrates. Fig. 4-3 is "Reproduced with permission from [Md. Suruz Mian, K. Okimura, and J. Sakai, J. Appl. Phys. **117**, 215305 (2015)]. Copyright [2015], AIP Publishing LLC."

4.3.3 XPS Depth Profiles of VO_2 Film Deposited on TiN/Si Substrates

In this section, XPS analysis was carried out to investigate the atomic composition and the interface condition between the VO_2 film and the TiN layer. Fig. 4-4 shows the XPS depth profiles of VO_2 film deposited on TiN/Si substrates.

XPS spectra were taken for C 1*s*, N 1*s*, O1*s*, Si 2*p*, V2*p*, and Ti 2*p* after every 2 min sputtering by Ar ion with an acceleration energy of 2 kV; same as described in XPS section of chapter 2 and 3. In Fig. 4-4, the horizontal axis shows the total Ar-ion sputtering time, while the vertical axis represents the atomic concentration.

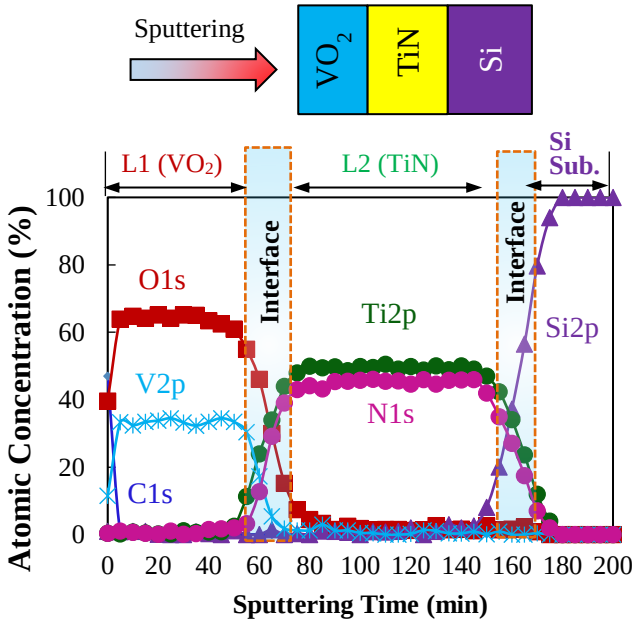

Fig. 4-4 XPS depth profiles of VO_2 film deposited on TiN/Si substrates.

In Fig. 4-4, two layers (L1 (VO_2) and L2 (TiN) were designated on Si substrates, same as observed in the cross-sectional SEM image in Fig. 4-2 (b). In the TiN buffer layer, the concentration of N atom was slightly smaller than stoichiometry. This fact probably reflected the initial TiN film quality. A sharp interface was observed between the VO_2 film and the TiN layer, confirming that the TiN layer acts as an electrode for the sample prepared at 230ºC. Consequently, an abrupt out-of-plane IMT was realized for the lower substrate temperature of 230ºC as illustrated in Fig. 4-3.

4.3.4 *I-V* Characteristics of VO_2 Film Deposited on TiN/Si Substrates

Before performing the oscillation measurement, it is essential to achieve a threshold switching. Figure 4-5 (a) shows the out-plane *I-V* measurement method, in which one probe contacted onto the VO_2 film and another one onto the TiN layer. The *I-V* characteristics were measured by using a curve tracer (Kokuyo Electric, SCT-2FR), where 50 Hz sinusoidal wave voltage was applied to VO_2.

Typical *I-V* curve as shown in Fig. 4-5 (b) was observed, in which the threshold switching phenomenon occurred at applied voltage of 1.8 V and threshold current of 80 μA (labeled as "A"). Calculated electric field in this device was 9×10^6 V/m, which is rather higher than those observed in VO_2/Ti/Si and VO_2/TiN/Ti/Si structures. Estimated consumption power was 144 μW. Before the threshold switching occurred, (at point "A") the resistance was 22.5 kΩ (insulating state or high resistance state (HRS)). After the switching occurred, the resistance decreased to about 2.1 kΩ (metallic state or low resistance state (LRS)); marked as "B".

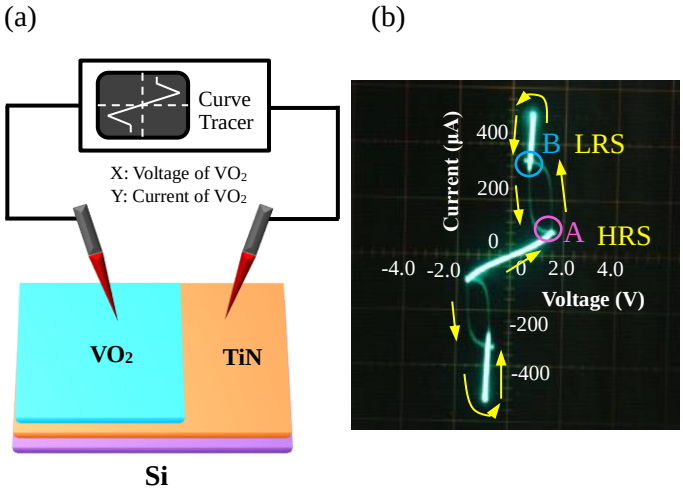

Fig. 4-5 (a) Out-of-plane *I-V* measurement method and (b) *I-V* characteristics of VO_2 film deposited on TiN/Si substrates. Fig. 4-5 (b) is "Reproduced with permission from [Md. Suruz Mian, K. Okimura, and J. Sakai, J. Appl. Phys. **117**, 215305 (2015)]. Copyright [2015], AIP Publishing LLC."

4.3.5 Oscillation Measurement of VO_2 Film Deposited on TiN/Si Substrates

4.3.5-1 Fundamental of Oscillation Measurement Method

In previous section, resistance switching at an applied voltage of 1.8 V, with switching current of 80 μA in out-of-plane *I-V* characteristic was observed. By using this device, oscillation phenomenon based on out-of-plane switching characteristic at room temperature was measured. A simple series circuit was used for the oscillation measurement, which consists of a DC voltage source *V*s, a series resistance R_E and the VO_2 sample.[23,25,27,30] Figure 4-6 shows a schematic of experimental circuit for the self-oscillation measurement. As shown in Fig. 4-6, the contact probe on the VO_2 layer was positively biased, and voltage drop in the VO_2 device (V_D) was monitored by a digital oscilloscope (Tektronix, TDS2022B). Advantest R6144 was used for dc power supply of constant voltage source. Previous reports on self-oscillation suggested that the self-oscillation phenomenon was triggered when V_S reached a certain threshold value that depends on the value of R_E.

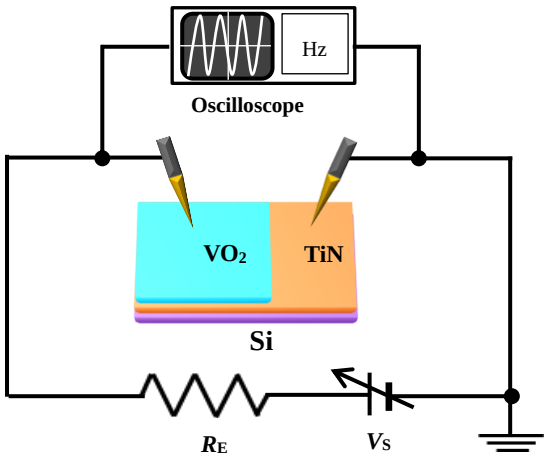

Fig. 4-6 A schematic of oscillation measurement circuit.[37]

4.3.5-2 Dependence of Oscillation Frequency on *Vs* and R_E

As described in section 4.1, it has been reported that the oscillation can only appear at a certain value of *Vs* and R_E. Self-oscillation phenomenon in present layered type device was also successfully observed by adjusting V_S and R_E. Figure 4-7 (a) shows the oscillation waveform with various V_S, with a fixed R_E of 36 kΩ. The oscillation was started at V_S = 5.3 V with the period of the waveforms of 0.9 μs, and still continued until V_S = 9.0 V with the period of the waveform of about 0.4 μs. When *Vs* increased to 10 V, the oscillation vanished, suggesting that the irreversible transition to metallic state occurred. The estimated oscillation frequency, f_{osc}, was 1.1 MHz for the *Vs* = 5.3 V and the highest f_{osc} of about 2.5 MHz was recorded at *Vs* = 9.0 V. The oscillation was stable for more than 10 minutes after being triggered. It can be observed that the period of each oscillation waveform strongly depends on the rising time (τ_1) of V_D, which corresponds to the recovery time of the metal-insulator transition (MIT). On the other hand, time needed for insulator-metal transition, τ_2 which is a jump from "A" to "B" in Fig. 4-5 (b), was almost same for all the waveforms. The IMT (threshold switching) took ~ 120 ns, which is higher than the electrical response time reported for a VO_2-based two-terminal planar-type VO_2 devices.[14]

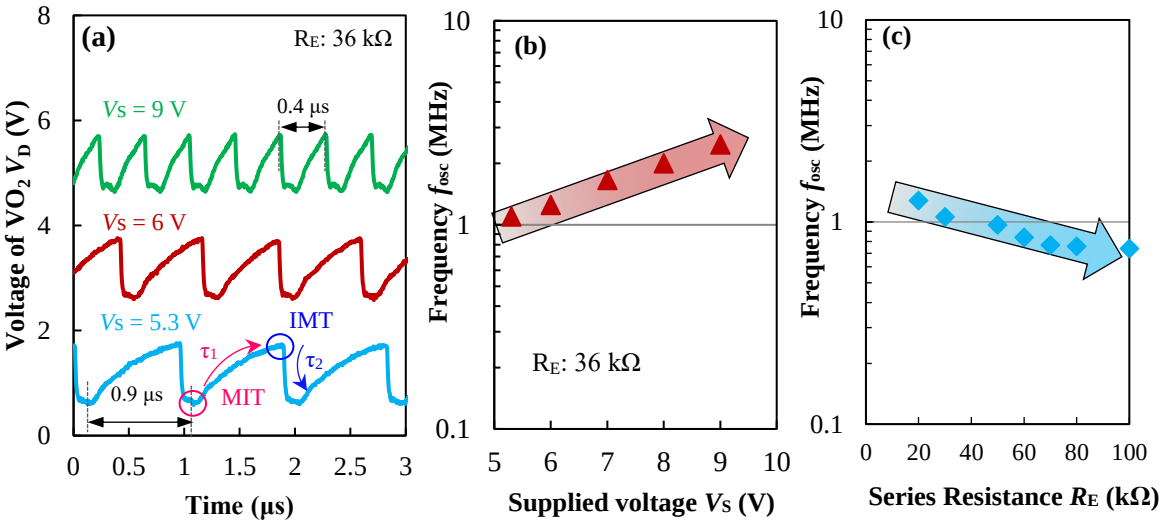

Fig. 4-7 (a) Oscillation waveforms for different *Vs*, (b) dependence of f_{osc} on *Vs*, and (c) dependence of f_{osc} on R_E. Minimum value of f_{osc}, observed firstly with increasing V_S, is plotted for each R_E.

Figure 4-7 (b) shows the dependence f_{osc} on *Vs*, as was calculated from Fig. 4-7 (a) in which f_{osc} was increased with the increasing of *Vs*, because the MIT time (τ_1) was decreased with the rising of *Vs* as shown in Fig. 4-7 (a). On the other hand, f_{osc} gradually decreased with the increasing of R_E as shown in Fig. 4-7 (c), similar to the other reported f_{osc} in the planar-type devices.[23]

4.3.5-3 Analytical Study of Oscillation Phenomena

In the previous section, dependency of f_{osc} on V_S and R_E was described. In this section, self-oscillation phenomenon was described by an equivalent circuit. Previously, it was reported that the recovering curve of the voltage across VO_2 device is well fitted by a charging curve based on a simple RC circuit, in which the resistance depends on the resistance of VO_2 device, R_D, and the series resistance, R_E, and the capacitance depends on the dielectric component of VO_2 device, C_D, and the floating capacitive component in the circuit.[25,27,30] As for the self-oscillation mechanism, restoring force of R_E is considered to make charging of capacitance in the VO_2 device. In other words, just after the IMT occurs in VO_2, restoring force of R_E makes charging up the capacitance in the VO_2 device up to the point "A" in Fig. 4-5 (b). Figure 4-8 (a) shows the equivalent circuit for the self-oscillation phenomenon of VO_2 device.[25,27,37]

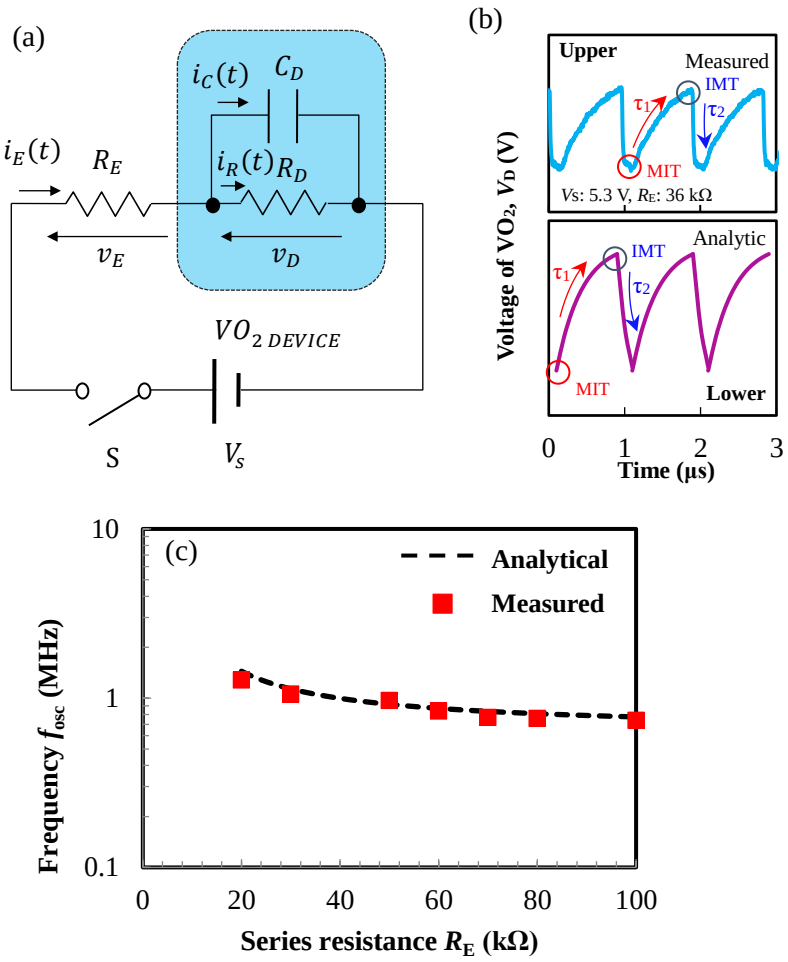

Fig. 4-8 (a) Equivalent circuit for the self-oscillation. (b) Comparison between an analytic and experimental waveforms. (c) Dependence of oscillation frequency, f_{osc}, on series resistance, R_E. Dotted line shows analysis based on equation (10). Minimum value of f_{osc}, observed firstly with increasing V_S, is plotted for each R_E.[37]

From Fig. 4-8 (a) the initial equations are given as below.

The current flowing through the device is given by Eq. (1).

$$i_C = \frac{dq_D}{dt} = C_D \frac{dV_D}{dt} \quad \text{..... (1)}$$

Here, q_D is the electric charge of VO_2 and $q_D = C_D V_D$; C_D is the capacitance of VO_2 device and parallel to the R_D, V_D is the voltage of VO_2 device.

Total current of the circuit, i_E is given by Eq. (2), which is flowing through the R_E.

$$i_E = i_C + i_R \quad \text{..... (2)}$$

Here, i_C is the current flowing through the C_D and i_R is the current flowing through the R_D.

Now, $i_R = \frac{V_D}{R_D}$ ..... (3)

Source voltage, $V_S = V_E + V_D$ ..... (4)

Here, V_E is the voltage of R_E.

From Eqs. (1) - (4), the governing differential equation is given by Eq. (5).

$$C_D R_E \frac{dV_D}{dt} + \left(1 + \frac{R_E}{R_D}\right) V_D = V_S \quad \text{..... (5)}$$

Solution of Eq. (5) is given by the sum of steady state and transient solutions.

Steady state solution is given by eq. (6).

$$V_{D-st} = \frac{R_D}{R_D + R_E} V_S \quad \text{..... (6)}$$

And transient solution is given by Eq. (7).

$$V_{D-trans} = Ae^{-\frac{R_D + R_E}{C_D R_D R_E} t} \quad \text{..... (7)}$$

Thus, general solution is given by

$$V_{D-general} = V_{D-st} + V_{D-trans} = \frac{R_D}{R_D + R_E} V_S + Ae^{-\frac{R_D + R_E}{C_D R_D R_E} t} \quad \text{..... (8)}$$

Constant A is decided by initial condition of capacitor C_D.

If $q_{C_D}|_{t=0}$=0, analytical solution of time-dependent voltage across the VO_2 device, V_D (t), is given as follows:

$$V_D(t) = \frac{R_D}{R_D + R_E} V_S \left(1 - e^{-\frac{R_D + R_E}{C_D R_D R_E} t}\right) \quad \text{..... (9)}$$

From Eq. (9), time constant τ for V_D (t) is given by

$$\tau = \frac{C_D R_D R_E}{R_D + R_E} \quad \text{..... (10)}$$

where R_D is the resistance of VO_2 and C_D is the capacitance parallel to the R_D. Using eq. (9), the experimental curve (Fig. 4-8 (b) *upper*) was simulated as shown in Fig. 4-8 (b) (*lower*). It can be seen that the experimental curve is well reconstructed. In this analysis (*lower*), time constant τ_1 for rising case (MIT) was calculated based on Eq. (10). On the other hand, τ_2 for IMT was shorter than MIT, corresponding to a discharge process in which much smaller resistance of metallic VO_2 determines the time constant together with C_D.

Figure 4-8 (c) shows the minimum oscillation f_{osc} observed for each R_E. Due to the fact that f_{osc} increases with V_S under a fixed R_E, as illustrated in Fig. 4-7 (b), minimum f_{osc} corresponds to the frequency at the threshold V_S. An analytical dependence of f_{osc} on R_E as a dotted line, together with the experimental results were shown in Fig. 4-8 (c). In the analysis, the value of R_D was constant at 20 kΩ, based on the experimentally measured resistance value of the VO_2 point contact. On the other hand, the value of CD was set constant at 7.8×10^{-11} F based on the measured f_{osc} corresponding to the observed time constant. The analytical curve reproduced the dependence of f_{osc} on R_E, supporting the validity of the equivalent circuit model. However, as previously reported, there exists a lower limit of R_E for the occurrence of oscillation.[23,30] In the present case, the lower limit of R_E was 20 kΩ.

4.3.5-4 Parametric Dependence of the Self-Oscillation Phenomenon in VO_2/Ti/Si Structures

(a) Film thickness and probe diameter

In planar type devices, the dependence of f_{osc} was reported only on circuit parameters of *V*s and R_E. However, the dependence of f_{osc} on geometrical parameters such as film thicknesses of VO_2 film and contact probe diameter has not yet been investigated. In this section, the dependence of f_{osc} was parametrically investigated. The VO_2/Ti/Si layered device structure fabricated at 250ºC was used in the parametric investigation of f_{osc}. In this parametric study, the dependence of f_{osc} on VO_2 film thicknesses and contact probe diameter was investigated. Those are important parameters in the layered type point contact device. In addition, the dependence of f_{osc} on hysteresis width of *I*-*V* characteristics was also explored.

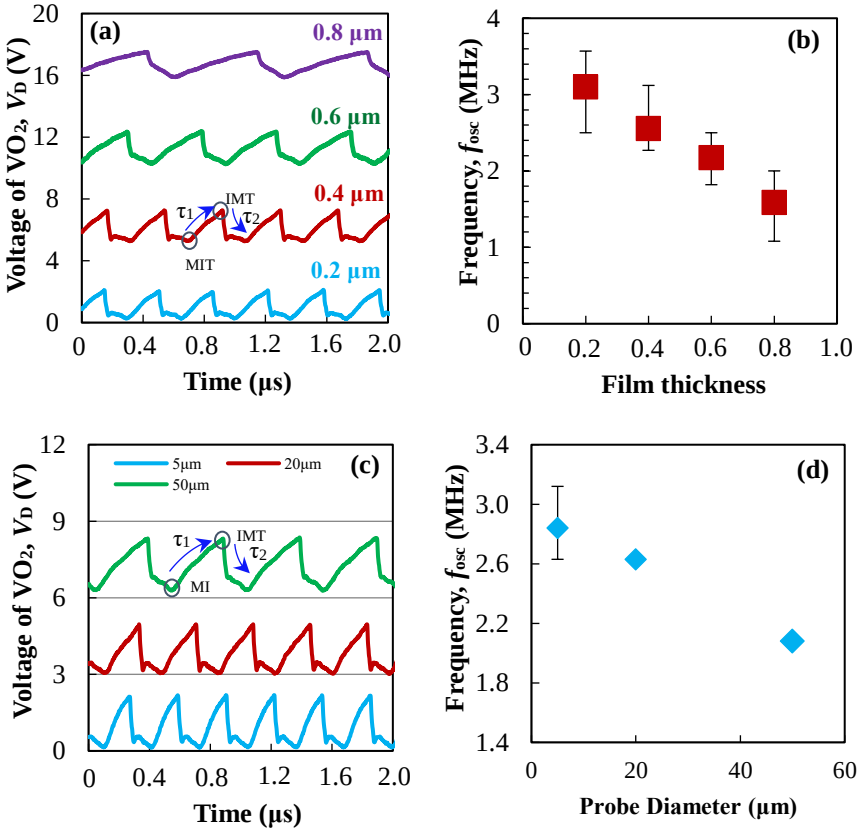

Fig. 4-9 (a) Oscillation waveforms and (b) f_{osc} for different film thicknesses.[37] (c) Oscillation waveforms and (d) f_{osc} for different probe diameters.

Figure 4-9 (a) shows the waveforms for different film thicknesses. As can be seen, charging time (τ_1) in rising period increases with increasing film thickness, while discharge time (τ_2) in falling period is

almost constant. Consequently, f_{osc} tends to decrease with the increase of film thickness as shown in Fig. 4-9 (b). In Fig. 4-9 (b), the average value of five measurements for each thickness were shown in a square symbol. Error bars show the variation of all measurements. Based on the geometrical considerations, out-of-plane resistance of VO_2 should increase with film thickness. As shown in Fig. 2-14 (Chapter 2), the values of resistance between two probes gradually increase with the thickness (until 0.6 μm). The increase of R_D is responsible for longer rising time as reflected in the measured waveforms. The results evidenced that the higher frequency over MHz range in the present out-of-plane device is due to the film thickness of the VO_2 layer which corresponds to the electrode distance in the planar-type device. Accordingly, in VO_2-based two-terminal planar type devices, oscillation frequency was restricted by the rather wide spacing between electrodes.[23,25,27,30,32] The present results proposed that the achievement of an out-of-plane configuration develops such fast oscillating devices based on out-of-plane threshold switching.

Fig. 4-9 (c) presents the oscillation waveforms of different contact probe diameters. The probe diameters were varied from 5 μm–50 μm. In Fig. 4-9 (c), it was found that the oscillation frequency decreased with increase of the probe diameter and the highest f_{osc} of 2.8 MHz was achieved for the smallest probe diameter of 5 μm. However, in this case the oscillation was a little unstable.

(b) Hysteresis width

Next, the dependence of f_{osc} on hysteresis width of the *I-V* characteristics was investigated. In the *I-V* characteristics, the different hysteresis width was found by adjusting the pressure of the contact probe. Basically, the small hysteresis was obtained when the contact probe pressure was relatively small. However, the contact probe pressure could not be measured in quantitatively for the experimental set-up limitation.

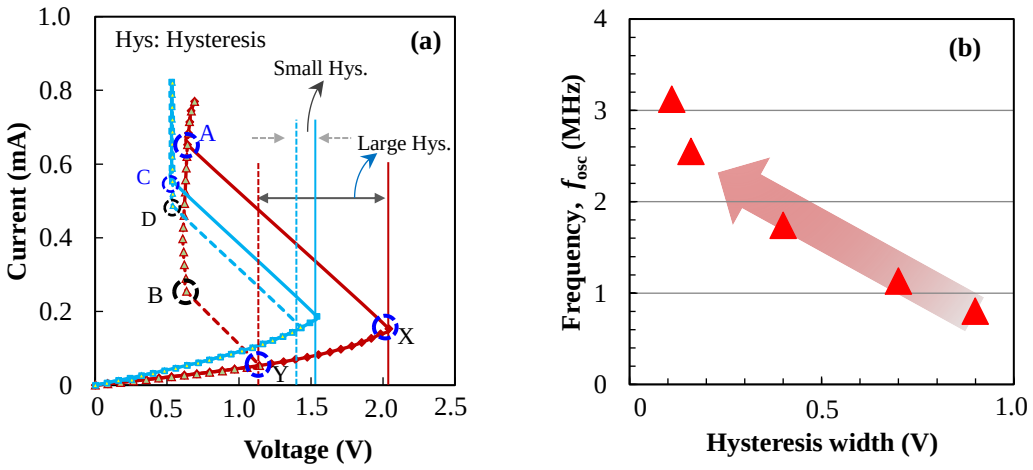

Fig. 4-10 (a) *I-V* characteristics with different hysteresis width and (b) f_{osc} for different hysteresis width.

In this case the top contact probe with a diameter of 50 μm was used for all measurements. Figure 4-10 (a) shows the *I-V* characteristics with different hysteresis width, measured by the Keithley 6487 Picoammeter/Voltage Source. In Fig. 4-10 (a), representative *I-V* characteristics which have wide and small hysteresis width were illustrated. Red cycles corresponds to the wide hysteresis, and light blue cycles corresponds to the small hysteresis. The solid lines represents the increasing case of current across the applied voltage and the broken lines indicates the decreasing case of the current. The hysteresis width was determined by the difference between the switching voltage, pointed at "X", and the voltage where the current looped back to the initial trace, pointed at "Y" for the wide hysteresis. The other hysteresis width was also calculated by the same method. Causes of large hysteresis width in switching characteristics consideration as follows; high contact probe pressure results in the increasing of the contact area and the decreasing of the resistance. Due to this matter, during the occurrence of the IMT, rather large amount of current flows, thus stabilizes the metallic state. This is expected to cause a delay in MIT, which is responsible for the large hysteresis width in the switching characteristics. In contrast, as the contact probe pressure decreases, small current flow results in small hysteresis width in the switching characteristics.

Figure 4-10 (b) shows the dependence of f_{osc} on the different hysteresis width. In Fig. 4- 10 (b), it can be seen that f_{osc} increased with the decrease of hysteresis width. In wider hysteresis width, it takes longer time to back the initial trace (A→ B) after the switching, resulting MIT time constant τ_1 (as shown in Fig. 4-9 (a) or (c)) becomes larger and f_{osc} turn to lower value. On the other hand, in smaller hysteresis width, after the switching occur, it does not take so much time (C→ D) to back to the initial trace, resulting the MIT time constant τ_1 (as shown in Fig. 4-9 (a) or (c)) becomes smaller-and f_{osc} turn to higher value. Highest f_{osc} with more than 3.12 MHz was obtained for the lowest hysteresis width.

4.3.5-5 Multi-step Resistance Switching and the Self-Oscillation Phenomenon

In the *I-V* measurements, a different *I-V* curve was observed when the contact probe pressure was relatively lower than the Fig. 4-10 (a). In this case, a multi-step *I-V* characteristics with a very small hysteresis was observed. The multi-step switching was observed at three times as labeled as "A", "B", and "C". Such multi-step *I-V* characteristics with a little wider hysteresis were previously reported for VO_2-based two-terminal planar type devices. [14] However, multi-step *I-V* characteristics without hysteresis has not yet been reported. After achieving this kind of switching, the oscillation was measured.

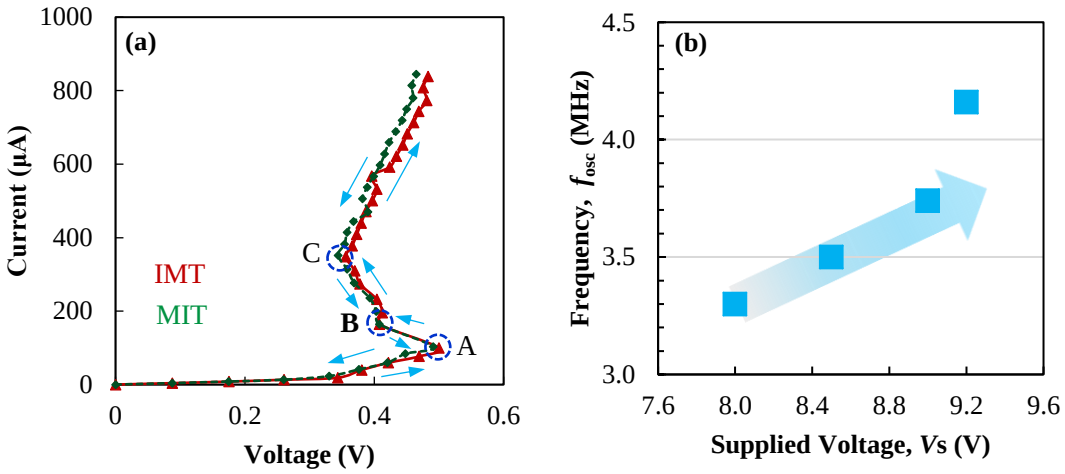

Fig. 4-11 (a) *I-V* characteristics with multi-step switching and (b) dependence of f_{osc} on *V*s for this *I-V* characteristics.

Fig. 4-11 (b) shows f_{osc} for different *V*s. The f_{osc} increased with *V*s and higher f_{osc} was recorded to be about 4.12 MHz. This value is the highest f_{osc} than the ever reported for VO_2-based two-terminal planar type devices and layered type device. In the previous section, it was observed that f_{osc} increased with the decrease of hysteresis width. Thus, based on the results shown in this and previous sections, it can be understood that the *I-V* with small hysteresis and multi-step is rather advantageous to achieve a high-frequency self-oscillation.

4.3.5-6 High-frequency Self-Oscillation in VO_2/TiN/Si Structures

In the previous section, high-frequency self-oscillation with f_{osc} of 4.12 MHz was achieved in the case of multi-step switching with smaller hysteresis width in VO_2/TiN/Si structures. In this section, the same type of *I-V* characteristics was realized when the contact pressure of the probe on the VO_2 film in VO_2/TiN/Si structures was weakened. Figure 4-12 (a) shows an *I-V* characteristic curve obtained when the probe contacting pressure was lower than in the case of Fig. 4-7 (a), where smaller hysteresis (between IMT and MIT) was appeared on the same device. In this case, the switching voltage and current were almost same as in Fig. 4-5 (b), while rather high oscillation frequency was observed in this case.

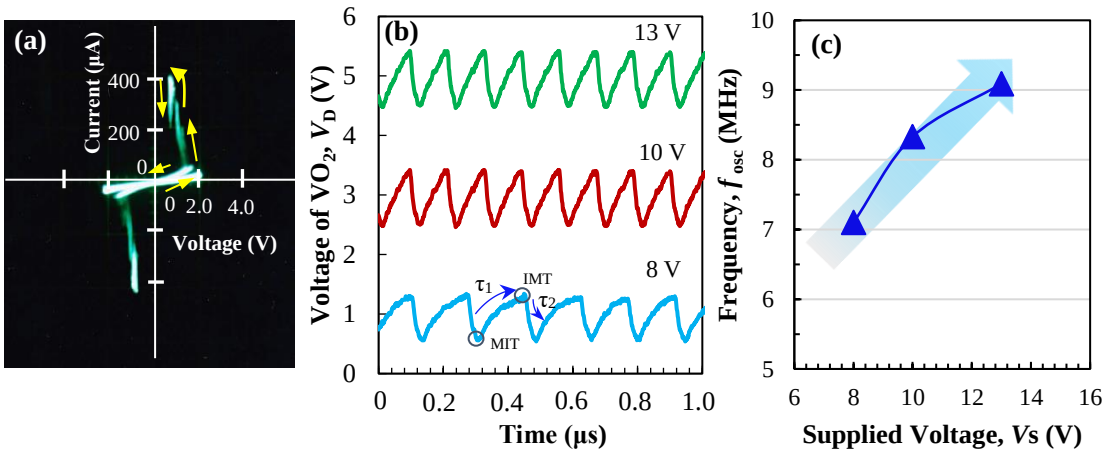

Fig. 4-12 (a) *I-V* characteristics with multi-step switching for high frequency oscillation mode, (b) oscillation waveforms for different *V*s, and (c) dependence of f_{osc} on *V*s. Series resistance, R_E, was kept constant at 30 kΩ.[37] Fig. 4-12 (a) is "Reproduced with permission from [Md. Suruz Mian, K. Okimura, and J. Sakai, J. Appl. Phys. **117**, 215305 (2015)]. Copyright [2015], AIP Publishing LLC."

Figure 4-12 (b) presents the oscillation waveforms for different *V*s. The MIT time constant τ_1 decreased with increase of *V*s. At *V*s = 8 V, τ_1 was found to be about 139 μs, which is further decreased to about 85 μs at *V*s= 13 V, while τ_2 was constant at around 48 μs. Figure 4-12 (c) shows the f_{osc} for different *V*s, calculated from Fig. 4-12 (b). The highest f_{osc} = 9.09 MHz was obtained for the *V*s= 13 V. This value is the highest value for VO_2 based all type devices. These results suggest the impact and potential of the present proposed layered type device. Such a high-frequency self-oscillation in VO_2 based layered type device makes it more promising for applications such as oscillators and micro-converters.

4.3.5-7 Mechanism of High-frequency Self-Oscillation

In the previous section, high-frequency self-oscillation with 9.09 MHz was observed in VO_2/TiN/Si device. In this section, the mechanism of the occurrence of self-oscillation with different frequency was discussed. In Fig. 4-13, three types of voltage triggered resistance switching, VTRS with negative differential resistance, NDR ($dV_D/dI_D < 0$) regions after the onset of IMT were illustrated. Fig. 4-13 (i) presents a non-hysteretic behavior between paths of IMT and MIT. In this case, faster transition occurs due to spontaneous recovering from metallic state ("b_1") to insulating state ("a_1"). Fig. 4-13 (ii) shows that the hysteretic ($b_2 \leftrightarrow c_2$) behavior between IMT and MIT. In this case, recovering time (τ_2) becomes longer than the case of 4-13 (i) because of the presence of the metallic state from "b_2" to "c_2", resulting the oscillation frequency to be lower than the case of Fig. 4-13 (i). In the present study, such kind of VTRS with the certain metallic period was observed, as shown in Fig. 4-5 (b) and 4-10 (a).

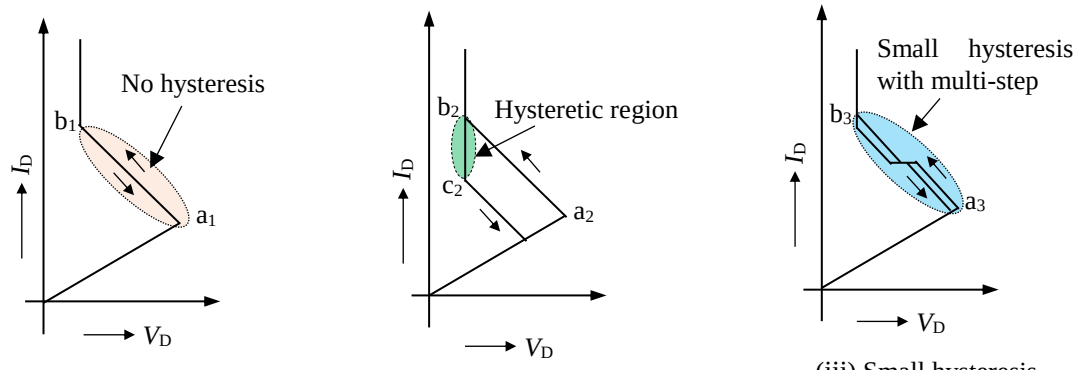

(i) Without hysteresis (ii) With hysteresis (iii) Small hysteresis with multi-step

Fig. 4-13 Illustrations for voltage triggered switching with NDR ($dV_D/dI_D < 0$) region after the onset of IMT for cases without hysteretic behavior between paths of IMT and MIT (i), with hysteretic behavior (ii), and multiple NDR regions with smaller hysteresis (iii).[37]

Figure 4-13 (iii) presents the multiple NDR regions with smaller hysteresis. In the previous section, high-frequency oscillation was obtained while low hysteresis width with multi-step *I*-*V* characteristics as shown in Fig. 4-11 and 4-12 was observed. Such multistep behavior in the NDR region of VO_2 based switching device was frequently reported.[14,38–40] In the present study, the inhomogeneous polycrystalline film with a granular surface was observed in the cross-sectional SEM image in Fig. 4-2 (b), which has possibly caused multiple contacting routes with the probe surface when the probe contacting pressure was rather low. Then, multiple current paths were formed between the probe and the film due to localized VTRS. In this case, the smaller hysteresis width, which might be due to the single crystalline VO_2 in each grain, causes recovering time shorter than the case in Fig. 4-13 (ii), resulting high-frequency oscillations. Present results with MHz band open new vistas for realizing simple layered structure devices for radio frequency generators and micro-inverters.

4.4 Conclusions

In this chapter, the performance of self-sustaining oscillation in the VO_2 layered type device was investigated. Self-sustaining oscillation phenomenon in the VO_2 is responsible for self-sustaining repetition of voltage triggered resistance switching.

For this experiment, the VO_2/Ti/Si structure deposited at 250ºC (as shown in chapter 2) and the VO_2/TiN/Si structure were introduced in this chapter. In the VO_2/TiN/Si structure, VO_2 films were deposited at a low substrate temperature of 230ºC by using the ICP-assisted sputtering method. The fabricated VO_2/TiN/Si showed clear interface between VO_2 and TiN layers and out-of-plane IMT with more than two orders of magnitude change in resistance. In *I-V* characteristics, the threshold switching was observed at the applied voltage of 1.8 V with switching current of 80 μA. By using this device, oscillation phenomena based on voltage triggered switching characteristic was measured at room temperature.

By adjusting *V*s and R_E, self-oscillation in out-of-plane configuration was successfully achieved. The oscillation was observed at *V*s= 5.3 V with a constant R_E of 36 kΩ. The duration of oscillation waveforms was 0.9 μs, and resulted in the f_{osc} of 1.1 MHz. The oscillation was stable for more than 10 minutes after being triggered. An equivalent circuit for the analytical study was proposed, and the experimental curve was observed to be well-reconstructed. In the analysis, the value of R_D was constant at 20 kΩ, based on the experimentally measured resistance value. The value of C_D was set constant at 7.8×10^{-11} F based on the measured f_{osc}.

In addition, the dependence of f_{osc} on VO_2 film thickness and probe diameter was investigated. Dependence of f_{osc} on hysteresis width was also studied. The frequency was decreased with the increasing of VO_2 film thickness, indicated that the resistance of VO_2 film determined the time constant for the recovery path. The f_{osc} was increased as the probe diameter decreased. Also, as the hysteresis width decreased, the f_{osc} observed to be gradually increased, because if the hysteresis width is large the recovering time of MIT (τ_1) become large, and resulting the large f_{osc}. A multi-step switching with a small hysteresis width was observed, when the contacting probe pressure was relatively smaller than the initial *I-V* measurement. In this case, high frequency of 4.12 MHz was realized, which was the highest f_{osc} ever observed for the VO_2-based all types device. These results suggested that smaller hysteresis width in *I-V* characteristics is an important key to achieve a high-frequency oscillation. Based on this result, further *I-V* characteristics were measured for the VO_2/TiN/Si device, by lowering the contacting probe pressure. A multi-step *I-V* characteristics was observed, with a very small hysteresis width. In this case, a very high f_{osc} of 9.09 MHz was recorded.

Finally, the mechanism of high-frequency oscillation was discussed. Based on these results, faster transition occurs was clarified due to the spontaneous recovering from metallic state to insulating state in a non-hysteretic behavior between paths of IMT and MIT in *I-V* characteristics. If the hysteretic behavior between IMT and MIT is appeared in *I-V*, longer recovering time was observed due to the

presence of the metallic state, resulting in the rather lower oscillation frequency compared to the non-hysteretic *I-V* is expected. Multi-step *I-V* in NDR with small hysteresis is the main issue to achieve a high-frequency oscillation. In the present study, the inhomogeneous polycrystalline film with a granular surface, as was shown in the cross-sectional SEM image, has a possibility to make multiple contacting routes when the probe contacting pressure was low. Then, multiple current paths were formed in between the probe and the film due to the localized voltage triggered switching. In this case, smaller hysteresis, which might be due to the single crystalline VO_2 in each grain, makes recovering time shorter.

The achieved low voltage switching with high speed in layered type device, open new vistas for the applications of VO_2 films in low voltage switching devices. Furthermore, High-frequency self - sustaining oscillation was obtained in the present proposed layered type device based on the fast resistance switching, which is expected to the application in micro-inverters.

References

[1] F. J. Morin, Phys. Rev. Lett. **3**, 34 (1959).

[2] C. N. Berglund and H. J. Guggenheim, Phys. Rev. **185**, 1022 (1969).

[3] J. B. Goodenough, J. Solid State Chem. **3**, 490 (1971).

[4] A. Zylbersztejn and N. F. Mott, Phys. Rev. B **11**, 4383 (1975).

[5] Renata M. Wentzcovitch, W. W. Schulz, and P. B. Allen, Phys. Rev. Lett. **72**, 3389 (1994).

[6] S. Biermann, A. Poteryaev, A. I. Lichtenstein, and A. Georges, Phys. Rev. Lett. **94**, 26404 (2005).

[7] A. Cavalleri, M. Rini, H. H. W. Chong, S. Fourmaux, T. E. Glover, P. A. Heimann, J. C. Kieffer, and R. W. Schoenlein, Phys. Rev. Lett. **95**, (2005).

[8] T. M. Rice, H. Launois, and J. Pouget, Phys. Rev. Lett. **73**, 3042 (1994).

[9] G. Stefanovich, A. Pergament, and D. Stefanovich, J. Phys. Condens. Matter **12**, 8837 (2000).

[10] H.-T. Kim, B.-G. Chae, D.-H. Youn, S.-L. Maeng, G. Kim, K.-Y. Kang, and Y.-S. Lim, New J. Phys. **6**, 52 (2004).

[11] M. M. Qazilbash, K. S. Burch, D. Whisler, D. Shrekenhamer, B. G. Chae, H.-T. Kim, and D. N. Basov, Phys. Rev. B - Condens. Matter Mater. Phys. **74**, 1 (2006).

[12] P. F. Bongers and U. Enz, Philips Res. Repts **21**, 387 (1966).

[13] K. van Steensel, F. van de Burg, and C. Kooy, Philips Res. Repts **22**, 170 (1967).

[14] K. Okimura, N. Ezreena, Y. Sasakawa, and J. Sakai, Jpn. J. Appl. Phys. **48**, 065003 (2009).

[15] Z. Yang, Y. Zhou, and S. Ramanathan, J. Appl. Phys. **111**, 1 (2012).

[16] J. Sakai and M. Kurisu, Phys. Rev. B - Condens. Matter Mater. Phys. **78**, 2 (2008).

[17] C. Ko and S. Ramanathan, Appl. Phys. Lett. **93**, 8 (2008).

[18] J. Leroy, A. Crunteanu, A. Bessaudou, F. Cosset, C. Champeaux, and J. C. Orlianges, Appl. Phys. Lett. **100**, 213507 (2012).

[19] L. A. Ladd and W. Paul, Solid State Commun. **7**, 425 (1969).

[20] H. S. Choi, J. S. Ahn, J. H. Jung, and T. W. Noh, Phys. Rev. B **54**, 4621 (1996).

[21] Y. Taketa, F. Kato, M. Nitta, and M. Haradome, Appl. Phys. Lett. **27**, 212 (1975).

[22] B. Fisher, J. Appl. Phys. **49**, 5339 (1978).

[23] J. Sakai, J. Appl. Phys. **103**, 103708 (2008).

[24] Y.W. Lee, B.J. Kim, J.W. Lim, S.J. Yun, S. Choi, B.G. Chae, G. Kim, and H.T. Kim, Appl. Phys. Lett. **92**, 8 (2008).

[25] H.-T. Kim, B.-J. Kim, S. Choi, B.-G. Chae, Y.-W. Lee, T. Driscoll, M. M. Qazilbash, and D. N. Basov, J. Appl. Phys. **107**, (2010).

[26] A. Crunteanu, J. Givernaud, J. Leroy, D. Mardivirin, C. Champeaux, J.-C. Orlianges, A. Catherinot, and P. Blondy, Sci. Technol. Adv. Mater. **11**, 065002 (2010).

[27] T. Driscoll, J. Quinn, M. Di Ventra, D.N. Basov, G. Seo, Y.-W. Lee, H.-T. Kim, and D. R. Smith, Phys. Rev. B - Condens. Matter Mater. Phys. **86**, 1 (2012).

[28] G. Seo, B.-J. Kim, H.-T. Kim, and Y.-W. Lee, J. Light. Technol. **30**, 2718 (2012).

[29] A. Beaumont, J. Leroy, J.-C. Orlianges, and A. Crunteanu, J. Appl. Phys. **115**, 154502 (2014).

[30] N. Shukla, A. Parihar, E. Freeman, H. Paik, G. Stone, V. Narayanan, H. Wen, Z. Cai, V. Gopalan, R. Engel-Herbert, D. G. Schlom, A. Raychowdhury, and S. Datta, Sci. Rep. **4**, 4964 (2014).

[31] Y. Wang, J. Chai, S. Wang, L. Qi, Y. Yang, Y. Xu, H. Tanaka, and Y. Wu, J. Appl. Phys. **117**, 1 (2015).

[32] B.J. Kim, G. Seo, Y.W. Lee, S. Choi, and H.T. Kim, IEEE Electron Device Lett. **31**, 1314 (2010).

[33] Md. Suruz Mian and K. Okimura, Jpn. J. Appl. Phys. **53**, 035802 (2014).

[34] Md. Suruz Mian and K. Okimura, J. Vac. Sci. Technol. A **32**, 041502 (2014).

[35] Y. Oka, T. Yao, N. Yamamoto, Y. Ueda, and A. Hayashi, J. Solid State Chem. **105**, 271 (1993).

[36] S. Ni, H. Zeng, and X. Yang, J. Nanomater. **2011**, 1 (2011).

[37] Md. Suruz Mian, K. Okimura, and J. Sakai, J. Appl. Phys. **117**, 215305 (2015).

[38] D. Ruzmetov, G. Gopalakrishnan, J. Deng, V. Narayanamurti, and S. Ramanathan, J. Appl. Phys. **106**, 083702 (2009).

[39] Y. Zhou, Z. Yang, and S. Ramanathan, Ieee Electron Device Lett. **33**, 101 (2012).

[40] Y. Zhou, X. Chen, C. Ko, Z. Yang, C. Mouli, and S. Ramanathan, IEEE Electron Device Lett. **34**, 220 (2013).

CHAPTER 5

Summary and Future Works

Chapter 5 Summary and Future Works

5.1 Summary

Transition metal oxide offers great opportunities for the next generation device applications due to its variety in structures and properties. Vanadium dioxide (VO_2) is also one of the material that has been continuously collecting attentions since the first discovery of its large insulator-to-metal transition (IMT) phenomenon in 1959. The IMT of VO_2 can be triggered by external parameters such as temperature, optical excitation, strain, and as well as the voltage addition. Voltage triggered resistance switching (VTRS) of VO_2 was first investigated in the VO_2-based two-terminal planar type devices. However, there has been a restriction in switching voltage and current, because the threshold switching voltage and current depend on the gap between both electrodes in this type configuration. Therefore, in order to investigate the intrinsic properties of VTRS, it is highly required to achieve a layered type device, in which VO_2 films is deposited on the conductive layer. Some research groups reported the layered type devices, including VO_2 films deposited on metallic plates such as Ti or Al, heavily doped Si wafers, Nb-doped SrTiO3 substrates, and metallic films such as Pt or Au. However, the out-of-plane IMT, the crystalline morphology, and the interface between the VO_2 film and the bottom electrode were not minutely investigated.

This dissertation mainly focuses on the crystalline growth of VO_2 films on the conductive layer with the aim of achieving a VO_2-based layered type device. In this work, out-of-plane IMT, crystalline morphology, the interface between the VO_2 film and the bottom electrode, and the out-of-plane switching characteristics were investigated. The self-sustaining oscillation performance of the layered devices was also investigated.

In chapter 1, the background of this study was introduced. Crystalline structure, band structure, and the synthesis method of VO_2 films were described. A review of VTRS in VO_2 and VO_2-based two-terminal planar type devices with problem statement was delivered in this chapter. Finally, the importance of VO_2-based layered type device with the motivation of this work was presented.

In chapter 2, the crystalline growth of VO_2 films on Ti/Si substrates was investigated by an inductively coupled plasma-assisted sputtering (ICPS) and conventional RF sputtering method.

Diffraction from VO_2 (011) plane was observed on samples prepared at 200 - 400°C, indicating that the VO_2 film grown on Ti/Si substrates has polycrystalline manner. The highest peak intensity was observed at 250°C, while the peak intensity decreased gradually with increasing temperature. In the resistance –temperature (R-T) characteristics, the largest out-of-plane IMT with resistance change of 2.6 orders of magnitude was realized in the sample prepared at 250°C. The disappearance of IMT in

the sample prepared at 400°C suggested that low-temperature deposition is required for achievement of large IMT of VO_2 film on the metal template.

In XPS results, a sharp interface between the VO_2 film and the Ti layer was clearly observed in the sample prepared at the substrate temperature of 250°C, while the formation of mixing layer with V, O and Ti was found in the samples prepared at temperatures higher than 350°C. Thus, it is vitally important to produce a sharp interface between the VO_2 film and the bottom electrode in order to achieve a superior IMT properties in the out-of-plane direction. In the sample of 250°C, Ti films acted as an electrode, and a sharp out-of-plane IMT was accomplished. On the other hand, the diffusion of O atoms and the oxidation of Ti layers were observed in the sample fabricated at the higher substrate temperature of 400°C, and responsible for the degradation of the out-of-plane IMT. Accordingly, it became clear that the 250°C is the suitable substrate temperature for the crystalline growth of VO_2 films on the Ti/Si substrates.

The obtained large out-of-plane IMT in VO_2 film on Ti/Si substrates is responsible for high resistance value at room temperature. In the present study, the presence of grain boundaries in the polycrystalline VO_2 film is considered to be responsible for such high initial resistance between the top electrode and the bottom electrode. Low-temperature deposition of VO_2 films on metal template by ICPS method enabled such large out-of-plane IMT.

In order to clarify the advantage of ICPS method compared to conventional sputtering (CS), comparisons of deposition performances and plasma diagnostics were done between ICPS and CS. As the results, crystalline VO_2 films could not obtained by CS at a temperature lower than 250°C in contrast to ICPS. Diagnostics results of ion energy distributions (IEDs) for substrate-incident ions showed that the presence of high energy ion components with energies around 80 and 150 eV enhance the low-temperature crystalline growth. In addition, enhancement of oxygen radical (O*) production is also considered to be responsible for the growth of stoichiometric VO_2 films.

In *I-V* characteristics, the threshold switching was observed at an applied voltage of 0.6 V with a current value of 150 μA (consumption power: 90 μW) for the sample of 230°C. This V_{th} value is much lower than the reported value for the VO_2-based two-terminal planar type devices, which was 2 V. Threshold switching was observed at 0.8 V and 1.6 V for the samples of 250°C and 300°C, respectively. The V_{th} and I_{th} were increased with *T*s. This should be due to the interfacial mixing layer. The achieved low voltage and power consumption have great potential for the application as a low voltage selective switch for the nonvolatile memory.

In chapter 2, the out-of-plane IMT with more than 2.6 orders of magnitude change in resistance was achieved for the sample deposited on Ti/Si substrates at low substrate temperature. However, such IMT was observed to disappear in the sample prepared at a high substrate temperature of 400ºC due to the diffusion of O atoms and the oxidation of Ti layer.

In chapter 3, TiN was introduced as a diffusion barrier with the aim of accomplishing a good crystalline VO_2 films even at a high substrate temperature of 400ºC. TiN films was deposited on Ti/Si substrates by DC magnetron sputtering method. The deposited TiN films showed polycrystalline feature and low resistivity on the order of 10^{-4} Ω cm, confirmed by the XRD and resistivity measurements. Then, VO_2 films were fabricated on TiN/Ti/Si substrates by the ICP-assisted sputtering method. The substrate temperature was varied from 100 to 400ºC. The crystallinity was evaluated by the XRD 2θ scan measurements.

In XRD results, diffraction from the VO_2 (011) plane was observed on all samples prepared at 250–400ºC. A significant improvement was found in the VO_2/TiN/Ti/Si structure; the peak intensity was increased with increasing substrate temperature, and the highest peak intensity was achieved in the sample of 400ºC. These results implied that a good crystallinity of VO_2 films was achieved at a high substrate temperature of 400ºC, while the degradation of crystallinity was obtained in the VO_2/Ti/Si structure fabricated at 400ºC. Peaks from VO_2 (B) metastable phase were observed on the samples deposited at 150 and 200ºC, while any peak from VOx was not observed at 100ºC.

In *R-T* characteristics, the R_{RT} increased with increasing substrate temperature, and two orders of magnitude changes in resistance were realized at the lower substrate temperature of 250-350ºC. Rather larger resistance drop with more than 2.3 orders of magnitude was observed at 400ºC. These results correspond to the XRD results in which highest peak intensity was obtained at 400ºC. The T_{IMT} was found to be 68ºC in the sample of 400ºC, which is identical to the generally recognized IMT temperature for bulk VO_2 crystal.

In XPS results, a sharp interface between the VO_2 film and the TiN layer was observed in the sample prepared at a low substrate temperature of 250ºC in the VO_2/TiN/Ti/Si structure. Significant improvement of abruptness in the interface between the VO_2 film and the TiN layer was realized in the VO_2/TiN/Ti/Si structure at 400°C, though a small amount of Ti atoms in the VO_2 region and O atoms in the TiN region were observed at this temperature. On the other hand, significant diffusion of O atoms and oxidation of Ti layer were observed in the sample fabricated at T_S of 400ºC in the VO_2/Ti/Si structure. Furthermore, three layers with including the VO_2 film, TiN layers, and Ti layers on Si substrates with clear interfaces were also confirmed in the cross-sectional SEM images, which are vitally important to realize a sharp interface between the VO_2 film and the metal layer, and led to the abrupt IMT in the out-of-plane direction.

In out-of-plane *I-V* characteristics, switching was observed at the applied voltage of 0.55 V and the switching current of 22 μA for the sample prepared at a substrate temperature of 250ºC. On the other hand, V_{th} and I_{th} were designated at 0.60 V and 55 μA for the sample prepared at 400 ºC, respectively. Rather higher values of V_{th} and I_{th} at 400ºC were considered to be responsible for observed small diffusion of O atoms at the interface between the VO_2 film and the TiN layer. The switching electric field was estimated to be 2.8×10^6 V/m and 3.0×10^6 V/m for both substrate temperatures of 250 and

400ºC. The estimated electric field was in the same order as previously reported value for VO_2 nanocontact and nanogap junction. The calculated power consumption at 250ºC was 12.1 μW, which is the lowest value ever reported in VO_2-based two-terminal planar type devices and as well as layered type device. The present layered type device with low switching voltage and low power consumption offers a great potential for the application as a low voltage and low power consumption switching elements.

In chapter 4, the performance of self-sustaining oscillation in VO_2-based layered type device was investigated. Self-sustaining oscillation phenomenon in the VO_2 film is responsible for self-sustaining repetition of voltage triggered resistance switching.

For this experiment, the VO_2/Ti/Si structure deposited at 250ºC (as shown in chapter 2) and the VO_2/TiN/Si structure were introduced in this chapter. In the VO_2/TiN/Si structure, the VO_2 film was deposited at a low substrate temperature of 230ºC by using the ICP-assisted sputtering method. The fabricated VO_2/TiN/Si showed clear interface between the VO_2 film and the TiN layers and out-of-plane IMT with more than two orders of magnitude change in resistance. In *I-V* characteristics, the threshold switching was observed at the applied voltage of 1.8 V with switching current of 80 μA. By using this device, oscillation phenomena based on voltage triggered switching characteristic was measured at room temperature.

By adjusting Vs and R_E, self-oscillation in out-of-plane configuration was successfully achieved. The oscillation was observed at Vs= 5.3 V with a constant R_E of 36 kΩ. The duration of oscillation waveforms was 0.9 μs, and resulted in the f_{osc} of 1.1 MHz. An equivalent circuit for the analytical study was proposed, and the experimental curve was observed to be well-reconstructed. In the analysis, the value of R_D was constant at 20 kΩ, based on the experimentally measured resistance value of VO_2 point contact device. The value of C_D was set constant at 7.8×10^{-11} F based on the measured f_{osc}.

In addition, the dependence of f_{osc} on VO_2 film thicknesses and contact probe diameter was investigated. Dependence of f_{osc} on hysteresis width was also studied. The frequency was decreased with increasing of VO_2 film thicknesses, indicated that the resistance of VO_2 film determined the time constant for the recovery path. The f_{osc} was increased as the probe diameter decreased. Also, as the hysteresis width decreased, the f_{osc} observed to be gradually increased, because if the hysteresis width is large the recovering time of MIT (τ_1) become large, and resulting the large f_{osc}. A multi-step switching with a small hysteresis width was observed, when the contacting probe pressure was relatively smaller than the initial *I-V* measurement. In this case, high frequency of 4.12 MHz was realized, which was the highest f_{osc} ever observed for the VO_2-based all types device. These results suggested that smaller hysteresis width in *I-V* characteristics is an important key to achieve a high-frequency oscillation. Based on this result, further *I-V* characteristics were measured for the VO_2/TiN/Si device, by lowering the contacting probe pressure. A multi-step *I-V* characteristics were

observed with a very small hysteresis width. In this case, a very high f_{osc} of 9.09 MHz was recorded.

Finally, the mechanism of high-frequency oscillation was discussed. Based on these results, faster transition occurs was clarified due to the spontaneous recovering from metallic state to insulating state in a non-hysteretic behavior between paths of IMT and MIT in *I-V* characteristics. If the hysteretic behavior between IMT and MIT is appeared in *I-V*, longer recovering time was observed due to the presence of the metallic state, resulting in the rather lower oscillation frequency compared to the non-hysteretic *I-V* is expected. Multi-step *I-V* in NDR with small hysteresis is the main issue to achieve a high-frequency oscillation. In the present study, the inhomogeneous polycrystalline film with a granular surface, as was shown in the cross-sectional SEM image, has a possibility to make multiple contacting routes when the probe contacting pressure was low. Then, multiple current paths were formed in between the probe and the film due to the localized voltage triggered switching. In this case, smaller hysteresis, which might be due to the single crystalline VO_2 in each grain, makes recovering time shorter.

From the above findings, VO_2-based layered device structure expected to open new vistas for realizing simple layered structure devices for radio frequency generators and micro-inverters.

In summary for this dissertation, the growth of VO_2 film on the conductive layers were realized at a low substrate temperature of 250ºC by using inductively coupled plasma-assisted sputtering (ICPS) method. High energy ion components of ICPS enhance the low-temperature crystalline growth. The VO_2 films grown on the Ti layer at 250ºC achieved large out-of-plane IMT with more than 2.6 orders of magnitude change in resistance, while that deposited at 400ºC IMT was disappeared due to the diffusion of O atoms and the oxidation of Ti layer. The diffusion of O atoms at high (400ºC) substrate temperature were successfully resolved by introducing TiN layers. Low voltage (0.55 V) and power consumption (12 μW) VTRS were realized at the low temperature (250ºC) deposited VO_2 films on TiN/Ti/Si substrates, indicating great potential for the application of VO_2 films in low voltage switching devices. High-frequency self-sustaining oscillation was obtained in the present proposed layered type device based on the fast resistance switching, which is expected to the application in micro-inverters.

5.2 Future Works

In this dissertation, the growth of VO_2 films on conductive layers deposited by the ICP-assisted sputtering method was investigated. IMT with more than 2 orders of magnitude was achieved in the out-of-plane direction. From the *I-V* characteristics measured for VO_2 with different film thicknesses, it was understood that the switching voltage decreases with decreasing of films thicknesses. In order to realize further lowering of switching voltage in layered type device structure, further decrease of the film thickness to several tens nm is required. For this purpose, reconsiderations on the target rf-power and ICP-rf power are needed to avoid the intrinsic interface problems in sputtering processes.

In order to allow deposition at a higher substrate temperature (300-350ºC), further improvement in the interface condition is required, where rather high-quality TiN layer is needed, further investigation regarding the deposition conditions of TiN layer is necessary.

ACHIEVEMENTS

Achievements

A. Peer Reviewed Journal Papers

1. **Md. Suruz Mian,** Kunio Okimura and Joe Sakai
   "Self-oscillation up to 9 MHz based on voltage triggered switching in VO_2/TiN point contact junctions"
   Journal of Applied Physics, 2015, Vol. 117, No 21, pp. 215305-1 ～ 215305-5.

2. **Md. Suruz Mian** and Kunio Okimura
   "Effect of conductive TiN buffer layer on the growth of stoichiometric VO_2 films and the out-of-plane insulator–metal transition properties"
   Journal of Vacuum Science and Technology **A,** 2014, Vol. 32, No. 4, pp. 041502-1 ～ 041502-6.

3. **Md. Suruz Mian** and Kunio Okimura
   "Effects of energetic substrate-incident ions on the growth of crystalline vanadium dioxide films in inductively coupled plasma-assisted sputtering"
   Japanese Journal of Applied Physics, 2014, Vol.53, No 3, pp. 035802-1 ～ 035802-6.

4. Kunio Okimura and **Md. Suruz Mian**
   "Low-temperature oriented growth of vanadium dioxide films on CoCrTa metal template on Si and vertical metal–insulator transition"
   Journal of Vacuum Science and Technology **A,** 2012, Vol. 30, No 5, pp. 051502-1 ～ 051502-7.

B. International Conference Papers

1. **Md. Suruz Mian** and Kunio Okimura
   "High frequency self-oscillations in VO_2 based out-of-plane device structure"
   Proceedings of The 13th International Symposium on Sputtering & Plasma Processes (ISSP 2015) pp. 436-439 (2015).

2. **Md. Suruz Mian** and Kunio Okimura
   "Layered growth of vanadium dioxide films on Ti/Si by inductively coupled plasma assisted sputtering method and out-of-plane electrical switching characteristics"
   Proceedings of The 12th International Symposium on Sputtering & Plasma Processes (ISSP 2013) pp. 345-348 (2013).

3. **Md. Suruz Mian** and Kunio Okimura
   "Vanadium Dioxide Film Growth on Titanium Metal Layer on Si (100) by Inductively Coupled"
   Plasma Assisted Sputtering Method"
   Proceedings of MJIIT-JUC Joint Symposium 2012 (MJJS 2012), ESE-8-1 pp. 1-4 (2012).

4. Nurul Hanis Azhan, **Md. Suruz Mian** and Kunio Okimura
   "Electrical properties of vanadium dioxide thin films on silicon substrate with metal-insulator transition"
   Proceedings of MJIIT-JUC Joint Symposium 2012 (MJJS 2012), ESE-8-2 pp. 1-4 (2012).

C. International Presentations

1. **Md. Suruz Mian,** Kunio Okimura, and Joe Sakai
   "Voltage induced electrical oscillation in VO_2-based layered structure device"
   14th International Union of Materials Research Societies-International Conference on Advanced Materials (IUMRS-ICAM 2015), II-4ThP-76, October 25-29, 2015, Jeju, Korea.

2. **Md. Suruz Mian** and Kunio Okimura
   "High frequency self-oscillations in VO_2 based out-of-plane device structure"
   The 13th International Symposium on Sputtering and Plasma Processes (ISSP 2015), MN3-8p, July 8-10, 2015, Kyoto Research Park, Kyoto, Japan.

3. **Md. Suruz Mian** and Kunio Okimura
   "Dependence of out-of-plane insulator-metal transition characteristics of VO_2 films on bottom electrode in layered structure device"
   7th International Symposium on Advanced Plasma Science and its Applications for Nitrides and Nanomaterials/8th International Conference on Plasma –Nano Technology & Science (IS Plasma-IC Plants 2015), D3-p-14, March 26-31, 2015, Nagoya University, Nagoya, Japan.

4. **Md. Suruz Mian** and Kunio Okimura
   "Growth of VO_2 films on TiN conductive layer with out-of-plane insulator-metal transition by ICP-assisted sputtering method"
   International Union of Materials Research Societies - International Conference on Electronic Materials 2014 (IUMRS-ICEM 2014), F1-P-0359, June 10-14, 2014, TWTC Nangang Exhibition Hall, Taipei, Taiwan.

5. **Md. Suruz Mian** and Kunio Okimura
   "Characterization of Insulator-Metal Transition of Vanadium Dioxide Films Grown on Titanium and Titanium Nitride layers"
   6th International Symposium on Advanced Plasma Science and its Applications for Nitrides and Nanomaterials/7th International Conference on Plasma –Nano Technology & Science (IS Plasma-IC Plants 2014), 06aP36, March 2-6, 2014, Meijo University, Nagoya, Japan.

6. **Md. Suruz Mian** and Kunio Okimura
   "Layered growth of vanadium dioxide films on Ti/Si by inductively Coupled plasma assisted sputtering method and out-of-plane electrical Switching characteristics"

The 12th International Symposium on Sputtering and Plasma Processes (ISSP 2013), TF-P2-16, July 10-12, 2013, Kyoto Research Park, Kyoto, Japan.

7. **Md. Suruz Mian** and Kunio Okimura
   "Vanadium Dioxide Film Growth on Titanium Metal Layer on Si (100) by Inductively Coupled" Plasma Assisted Sputtering Method"
   MJIIT-JUC Joint Symposium 2012 (MJJS2012), November 21-23, 2012, MJIIT, UTM, Kuala Lumpur, Malaysia.

8. Nurul Hanis Azhan, **Md. Suruz Mian** and Kunio Okimura
   "Electrical properties of vanadium dioxide thin films on silicon substrate with metal-insulator transition"
   MJIIT-JUC Joint Symposium 2012 (MJJS2012), November 21-23, 2012, MJIIT, UTM, Kuala Lumpur, Malaysia.

9. **Md. Suruz Mian** and Kunio Okimura
   "Growth of vanadium dioxide thin films with metal-insulator transition on CoCrTa at low temperature".
   15th International Conference on Thin Films, P-S2-33, November 8-11, 2011, Kyoto TERRSA, Kyoto, Japan.

10. Tomo Watanabe, **Md. Suruz Mian**, Kunio Okimura and Joe Sakai
    "Growth of phase transition VO_2 films with M2 phase in inductively coupled plasma assisted reactive sputtering".
    15th International Conference on Thin Films, P-S2-44, November 8-11, 2011, Kyoto TERRSA, Kyoto, Japan.

D. Awards

1. ***Best Poster Award***

   "Voltage induced electrical oscillation in VO_2-based layered structure device."

   (IUMRS-ICAM 2015)

2. ***Best Poster Award***

   "High frequency self-oscillations in VO_2 based out-of-plane device structure."

   (ISSP 2015)

3. ***Best poster presentation award***

   "Dependence of out-of-plane insulator-metal transition characteristics of VO_2 films on bottom electrode in layered structure device."

   (IS Plasma-IC Plants 2015)

4. ***Best Poster award***

   "Growth of VO_2 films on TiN conductive layer with out-of-plane insulator-metal transition by ICP-assisted sputtering method."

   (IUMRS-ICEM 2014)